LICENTIATE THESIS

Clustering and caustics in one-dimensional models of turbulent aerosols

JAN MEIBOHM

Department of Physics
University of Gothenburg
Göteborg, Sweden 2018

Clustering and caustics in one-dimensional models of turbulent aerosols
Jan Meibohm

ISBN 978-91-7833-165-9 (PRINT)
ISBN 978-91-7833-166-6 (PDF)

Department of Physics
University of Gothenburg
SE-412 96 Göteborg
Sweden
Telephone: +46 (0)31-786 00 00

Front cover: A picture drawn by the author in the introductory course for PhD students at Gothenburg University. Using this drawing, the author was supposed to explain to his fellow students what his research was going to be about.

Printed by BrandFactory AB
Göteborg, Sweden 2018

ABSTRACT

Heavy particles suspended in turbulent fluid flows, so-called turbulent aerosols, are common in nature and in technological applications. A prominent example is rain droplets in turbulent clouds. Due to their inertia, ensembles of aerosol particles distribute inhomogeneously over space and can develop large relative velocities at small separations.

We use statistical models that mimic turbulent flow by means of Gaussian random velocity fields to describe these systems. Compared to models that involve actual turbulence, our statistical models are simpler to study and allow for an analytical treatment in certain limits. Despite their simplicity, statistical models qualitatively explain the results of direct numerical simulations and experiments.

In this Licentiate thesis, we focus primarily on studying one-dimensional versions of the statistical model. The results of these systems create intuition for, and give important insights into the behaviour of higher dimensional models of particles in turbulence.

List of papers

This thesis consists of an introductory text and the following three appended papers:

Paper A

Meibohm, J., Candelier, F., Rosen, T., Einarsson, J., Lundell, F. & Mehlig, B. 2016 Angular velocity of a spheroid log rolling in a simple shear at small Reynolds number. *Physical Review Fluids* **1** (8), 084203.

Paper B

Meibohm, J., Pistone, L., Gustavsson, K., & Mehlig, B. 2017 Relative velocities in bidisperse turbulent suspensions. *Physical Review E* **96** (6), 061102(R).

Paper C

Dubey, A., Meibohm, J., Gustavsson, K., & Mehlig, B. 2018 Fractal dimensions and trajectory crossings in correlated random walks. *arXiv e-print 1806.08207*

ACKNOWLEDGEMENTS

First and foremost, I would like to thank my supervisors Bernhard Mehlig and Kristian Gustavsson for taking me as a student and for creating a vibrant research environment.

Furthermore, I would like to thank our collaborators who I had the pleasure of working with: I thank Tomas Rosén, Fredrik Lundell and Lorenzo Pistone for interesting discussions and great numerical work. I am grateful to Fabien Candelier for introducing me to fluid dynamics and matched asymptotic expansions. Further, I would like to thank my office mates Johan and Anshuman for helping me with many different things and for making the office the fun place it is. Thanks also to Marina, Erik and Anshuman for proofreading the thesis, and to Sophia for always being there.

CONTENTS

PART I
INTRODUCTION

Systems of heavy particles immersed in turbulent fluids, called turbulent aerosols, are abundant in nature and technology [1, 2]. A prominent example is water droplets in warm stratocumulus clouds [3]. Cloud turbulence is believed to play an important role in the growth of droplets [4, 5]. When the droplets are small, they grow primarily through collisions, which are facilitated by the turbulence [6]. In order to understand the impact of turbulence on droplet growth, a detailed knowledge of the dynamics of turbulent aerosols is required. In particular, it is vital to understand how often the aerosol particles come close together and, when they do, how fast they move relative to each other [7, 8, 9, 10]. Due to particle inertia, heavy particles may cross the stream lines of the underlying fluid and engage in spatial clustering [1, 2, 11, 12, 13, 14]. Clustering describes the phenomenon that ensembles of heavy particles, instead of distributing homogeneously over space, form regions of high (and low) concentration even though the underlying turbulent fluid may be incompressible. At the same time, particles with different acceleration histories may approach each other at high relative velocities due to caustic singularities in the inertial particle dynamics [6, 7, 8, 9, 10, 15], which affects the rate and outcomes of collisions [2].

Models based on a probabilistic approach to turbulence, called statistical models in the literature [1], have helped considerably in the understanding of the dynamics of turbulent aerosols. These models abandon the ambitious endeavour of describing the underlying turbulence and instead model the fluid by a random velocity field [11, 16]. The particle dynamics is subject to forces induced by the random fluid field fluctuations. Using statistical models, we can study the mechanisms of spatial clustering and the relative velocity statistics in a simplified environment. Yet these models are realistic enough to qualitatively explain the results of turbulence simulations and experiments [1].

In this Licentiate thesis, we review known results and discuss recent progress in the study of statistical models for turbulent aerosols. We focus

primarily on one-dimensional versions of the model, for which analytical results can be obtained. Known models of this type are the white-noise model [1] and the telegraph model [17]. We introduce a new system with this property, the persistent-flow model, which is valid for weakly inertial particles in a highly persistent flow. Despite the apparent simplicity of these one-dimensional models, they are surprisingly rich in their dynamics and provide valuable insights for higher dimensional systems [1, 6, 18]. This aspect is shown and discussed in the research papers appended to the text.

The thesis is organised as follows: After moving step-by-step from the complex problem of inertial particles in turbulence to statistical models in Chapter 1, we discuss the phenomenon of spatial clustering in Chapter 2. In Chapters 3 we review and extend the knowledge of spatial clustering in one-dimensional statistical models. The research papers produced in the course of three year's work are reviewed and put into the context of the preceding text in Chapter 4. Conclusions are drawn and possible future projects are discussed in Chapter 5.

This Licentiate thesis is intended to give the interested reader an intelligible and concise introduction to the world of one-dimensional statistical models of turbulent aerosols. In the author's personal view, the papers B and C showcase the value of these models. Paper A discusses the angular velocity of a *single* particle in a shear flow and is slightly detached from the rest of the work.

1 Particles in fluids

The motion of an ensemble of non-interacting spherical particles in fluid turbulence is a complex problem to study [1, 2, 6]. This becomes clear already when considering the motion of a single particle. On the one hand, the fluid motion, possibly a very complicated motion in itself, applies a force on the particle which makes it move. The moving particle, on the other hand, pushes aside the fluid, generating a complicated disturbance of the flow. Disturbances of that kind may, depending on the viscosity of the fluid, persist for some time and affect the particle motion later. If more particles are involved, other effects such as hydrodynamic interactions between the particles come into play [19, 20]. Due to the complexity of the system, the main challenge is to find a way of simplifying the problem without losing the essential physics. Before discussing the approximations and simplifications we are going to make in this work, we describe the system on a more formal level.

1.1 Problem formulation

The dynamics of particles in an incompressible fluid is described by the Navier-Stokes equations [21, 22, 23]

$$\frac{\partial \boldsymbol{w}}{\partial t} + (\boldsymbol{w}\cdot\nabla)\boldsymbol{w} = -\nabla p - \nu\nabla^2\boldsymbol{w}\,, \tag{1.1a}$$

$$\nabla\cdot\boldsymbol{w} = 0\,. \tag{1.1b}$$

Here, $\boldsymbol{w}(\boldsymbol{x},t)$ and $p(\boldsymbol{x},t)$ are the velocity of the fluid and the pressure at position $\boldsymbol{x}$ and time t, respectively. The quantity ν denotes the kinematic viscosity of the fluid. The first equation (1.1a) can be identified as Newton's second law for an infinitesimal fluid parcel. Eq. (1.1b) ensures incompressibility of the flow. First, we note that the Navier-Stokes equations are non-linear, because of the so-called convective term $(\boldsymbol{w}\cdot\nabla)\boldsymbol{w}$ on the left hand side of Eq. (1.1a). This non-linearity has drastic and important consequences that we describe later in this Section. The term $-\nu\nabla^2\boldsymbol{w}$ on the right-hand side of the equation is called the viscous term. It is responsible for the dissipation of energy in the fluid. Because of the viscous term, perturbations of the flow smoothen out with time. For our purposes, the Navier-Stokes equations need

to be supplemented by suitable boundary conditions that account for the presence of the particles. The no-slip boundary condition is used in viscous flows. It requires that the fluid velocity relative to the surface of the particles must vanish [19, 20]. The no-slip boundary condition leads to fluid stresses on the particle surfaces which in turn result in forces that make the particles move [19, 20].

There are two fundamental difficulties in describing the above system. The first one arises, because the problem requires the simultaneous solution of the field equations (1.1), while satisfying the boundary conditions which change as a function of time as the particles move through the fluid. Problems like this require so-called self-consistent solutions that are challenging to obtain even for a small number of particles [19, 20]. Second, if the fluid moves quickly, the non-linear term in Eq. (1.1a) renders the solutions of the Navier-Stokes equations unstable, leading to chaotic fluid motion. In fluid dynamics, this is known as turbulence [22, 23]. These difficulties make the complete problem intractable and call for approximations. We explain these approximations in the Sections that follow.

1.2 One-way coupling approximation

First, we assume that the particle system is so dilute that there are no hydrodynamic interactions between the particles. This is typically the case in, for instance, turbulent air clouds [1]. Note, however, that when there is strong spatial clustering of the particles, this assumption may break down [1, 24]. Second, we assume that the particles are much smaller than the smallest structures of the flow. Because of the viscous term, such a smallest spatial scale exists, a fact we discuss in the next Section.

These assumptions motivate the 'one-way coupling' approximation [25]. It assumes that the presence of the particles changes the flow only marginally so that the boundary condition can be disregarded in Eqs. (1.1). That is to say, the motion of the particles is influenced by the fluid flow, but the flow-field, on the other hand, is not affected by the particles. The one-way coupling approximation is useful because it decouples the flow-field motion from the motion of the particles, making the problem more tractable. Once the equations are decoupled, we can discuss turbulence and the particle motion separately.

1.3 Turbulence

Turbulence is the most common state of fluids in nature. It describes the chaotic and strongly mixing behaviour of rapidly moving fluids and is caused by the non-linearity of the problem (1.1) [22]. Despite its long history, turbulence is still an active field of research and the non-linear field equations (1.1) remain a major challenge. Since the times of Navier and Stokes the understanding of turbulence has improved considerably [26], while several fundamental problems remain unsolved. In this Section, we describe important aspects of turbulence on a phenomenological level. A better understanding of the existence of a smallest scale in turbulence and the origin of the highly irregular motion in turbulent flows motivates the main ingredient to our model for turbulent aerosols, the random flow field. For a detailed account of turbulence see Refs. [22] and [23].

1.3.1 Reynolds number

Given a length scale L and a velocity scale V, we can construct the dimensionless Reynolds number

$$\mathrm{Re} = \frac{LV}{\nu}\,, \tag{1.2}$$

which characterises the flow behaviour [19, 22]. In simple systems such as the flow of water through a pipe, there is a *single* Reynolds number that characterises the motion of the fluid, regardless of the magnitudes of the individual quantities in Eq. (1.2). The significance of Re becomes clear when transforming the variables in the Navier-Stokes equations (1.1a) according to $\boldsymbol{w} \to V\boldsymbol{w}$, $\boldsymbol{x} \to L\boldsymbol{x}$, $t \to (L/V)t$ and $p \to (V\nu/L^2)p$. One obtains the dimensionless equation

$$\mathrm{Re}(\partial_t \boldsymbol{w} + (\boldsymbol{w}\cdot\nabla)\boldsymbol{w}) = -\nabla p - \nabla^2 \boldsymbol{w}\,, \tag{1.3}$$

that depends only on the Reynolds number, and possibly on the boundary conditions. Because Re appears on the left-hand side of Eq. (1.3), it controls the importance of the terms $\partial_t \boldsymbol{w}$ and $(\boldsymbol{w}\cdot\nabla)\boldsymbol{w}$. As mentioned earlier, the non-linear convective term $(\boldsymbol{w}\cdot\nabla)\boldsymbol{w}$ is responsible for the onset of turbulence. At small Re, the non-linearity is negligible and Eq. (1.3) can be treated as effectively linear. Solutions of the linearised equations are stable and possibly

steady. In particular, these flows do not mix and individual fluid parcels move along stream lines. Flows with these properties are called laminar [19].

If we want to describe more complex systems than a simple pipe flow, the construction of the Reynolds number according to Eq. (1.2) is no longer unique. Consequently, fluid dynamical problems that contain several length and/or velocity scales, are characterised by several different Reynolds numbers. Thus for a finite-size particle moving in a pipe flow, we have a flow Reynolds number associated to the motion of the fluid in the pipe and a particle Reynolds number associated to the relative motion of the particle and the fluid.

We now discuss a fluid at large Reynolds number, $\mathrm{Re} \gg 1$. In this case, the non-linear term renders the flow unstable and we expect the fluid motion to be highly irregular and complicated. Observations fluid flows at high Reynolds numbers indicate, however, that statistical averages of turbulent flows have a lot of symmetry. Loosely speaking, the flow looks irregular and complicated in the same way everywhere and for all times. This simple argument describes the important concept of statistical homogeneity and isotropy of turbulent flow [22, 23]. If the Reynolds number is large enough, suitably defined statistical observables of the flow, such as correlation functions, are invariant under translations and rotations.

1.3.2 Turbulent cascade

It is instructive to think that turbulent fluid motion is characterised by eddies of different sizes. Think of a cup of coffee and add a little milk to it. Not much happens so far, but as soon as we start to stir the mixture with a spoon, eddies of approximately the size of the spoon form. These eddies are unstable and break up into smaller eddies, which again decompose into even smaller ones [22]. In the coffee cup we now suddenly see a lot of structure. A whole ensemble of eddies of different sizes interact with each other, engaging in the formation of complex patterns. If we were to zoom in into these patterns very closely, we would realise that there is a finite end to the structure in the fluid. At small scales, depending how thick, or viscous, the coffee and the milk are, the eddy-structure so predominant at larger scales, is gone. The internal friction of the fluid efficiently smoothens out all small structures below a certain length scale, called the Kolmogorov length η_{K} [22, 23, 27, 28].

In the turbulence literature, the ensemble of eddies of different sizes is

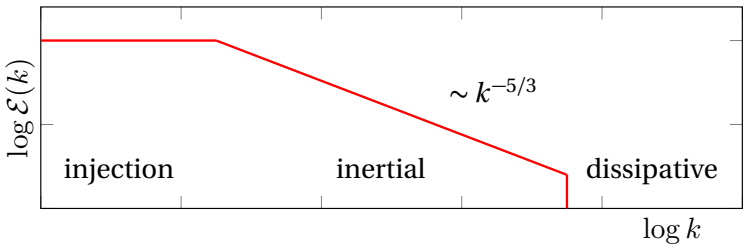

Figure 1.1: Schematic of the energy spectrum $\mathcal{E}(k)$ as a function of k.

called the 'Richardson' or 'energy' cascade [22, 29], because it transports the injected energy at large length scales (stirring with the spoon) to ever smaller scales until it is eventually dissipated into heat at scales of the order of η_K.

Eddies of size l have an associated wave number $k \sim 1/l$. Hence, small spatial scales correspond to large k-values whilst large spatial scales correspond to small k. We define the scale-dependent quantity $\mathcal{E}(k)$ to be the energy content of eddies with wave number k [23]. In a famous series of papers, Kolmogorov [27, 28] used symmetry and universality arguments to describe $\mathcal{E}(k)$ for isotropic and homogeneous turbulence. His result is shown schematically as the red line in Fig. 1.1. The flat regime at small k is the scale associated to energy injection, called the 'injection scale'. The energy that is brought into the system at these large length scales (small k) is transported to smaller scales (larger k) by means of the Richardson cascade described above. Kolmogorov was able to show that on the basis of his assumptions, $\mathcal{E}(k)$ has a power-law form with exponent approximately $-5/3$ at wave numbers sufficiently larger than the injection scale [27, 28]. This regime is called the 'inertial range'. At large k and small length scales of the order of η_K, this power law is cut off by dissipation and, hence, by the viscosity of the fluid, in a regime called the 'dissipative range'.

As noted in Section 1.2 we want to describe systems in which the particles are smaller than the Kolmogorov length. It has been shown that the length scales where the fluid-velocity field is smooth can extend up to several η_K, depending on the Reynolds number [1, 30]. We may therefore assume that the fluid flow which the particles experience is smooth.

1.3.3 Gaussian random-flow model

We now condense the insights gained in the previous Section into a simple fluid model. Because the detailed turbulent motion at high Reynolds numbers is highly irregular, it is practically unpredictable. For systems like this, it makes sense to consider its long-time statistical properties instead of trying to predict individual realisations [22, 23, 31]. Here, we go one step further and adopt a drastic simplification that lies at the heart of the statistical description of turbulence. We construct models that put emphasis only on modelling the *statistics* of the flow field $\boldsymbol{w}(\boldsymbol{x},t)$, not its individual realisations [1]. At first sight, this may not appear to be a great simplification. However, it allows us to abandon the idea of solving the Navier-Stokes equations (1.1) and, thus turbulence, all together. Instead, we introduce a field $\boldsymbol{u}(\boldsymbol{x},t)$ with statistical properties that are similar to those of $\boldsymbol{w}(\boldsymbol{x},t)$ in the dissipative range. To this end, we define a d-dimensional random field $\boldsymbol{\phi}(\boldsymbol{x},t)$ in a periodic box of size L by [1, 11]

$$\boldsymbol{\phi}(\boldsymbol{x},t) = N_d \sum_{\boldsymbol{k}} \boldsymbol{a}_{\boldsymbol{k}}(t) f(\boldsymbol{k}) \mathrm{e}^{i\boldsymbol{k}\cdot\boldsymbol{x}}, \tag{1.4}$$

where $\boldsymbol{k} \in (2\pi/L)\mathbb{Z}^d$ and N_d is a normalisation constant that depends on d. Furthermore, for a given $\boldsymbol{k}$, $\boldsymbol{a}_{\boldsymbol{k}}(t)$ is a stationary, complex d-dimensional random process and f is a function of $\boldsymbol{k}$ that we specify below. Since $\boldsymbol{\phi}$ is real, we need to add the condition that $\boldsymbol{a}^*_{\boldsymbol{k}}(t) = \boldsymbol{a}_{-\boldsymbol{k}}(t)$.

In this work, we use two and three dimensional incompressible random velocity fields defined by

$$\boldsymbol{u}(\boldsymbol{x},t) = \boldsymbol{\nabla} \wedge \boldsymbol{\phi}(\boldsymbol{x},t). \tag{1.5}$$

One-dimensional fields, however, can always be expressed in terms of the derivative of a potential and are hence compressible. Therefore, we define one-dimensional *compressible* velocity fields as

$$u(x,t) = \partial_x \phi(x,t). \tag{1.6}$$

Note that we have defined the random field (1.4) so that spatial and time correlation factorise if the processes $a_{i,\boldsymbol{k}}(t)$ are independent. To see this consider the correlation function

$$\langle \phi_i(\boldsymbol{x},t)\phi_j(\boldsymbol{y},s)\rangle = N_d^2 \sum_{\boldsymbol{k},\boldsymbol{l}} \langle a_{i,\boldsymbol{k}}(t) a_{j,\boldsymbol{l}}(s)\rangle f(\boldsymbol{k}) f(\boldsymbol{l}) \mathrm{e}^{i(\boldsymbol{k}\cdot\boldsymbol{x}+\boldsymbol{l}\cdot\boldsymbol{y})}. \tag{1.7}$$

Clearly, if $a_{i,\boldsymbol{k}}$ are independent so that $\langle a_{i,\boldsymbol{k}}(t)a^*_{j,\boldsymbol{l}}(s)\rangle = C(|t-s|)\delta_{ij}\delta_{\boldsymbol{kl}}$, Eq. (1.7) factorises and we find

$$\langle \phi_i(\boldsymbol{x},t)\phi_j(\boldsymbol{y},s)\rangle = \delta_{ij}C(|t-s|)G(\boldsymbol{x}-\boldsymbol{y}), \tag{1.8}$$

where $G(\boldsymbol{x}) = N_d^2 \sum_{\boldsymbol{k}} f(\boldsymbol{k})^2 \mathrm{e}^{i\boldsymbol{k}\cdot\boldsymbol{x}}$ is proportional to the Fourier transform of $f(\boldsymbol{k})^2$. Note further that using this construction, the statistics of $\boldsymbol{\phi}(\boldsymbol{x},t)$ at each point $\boldsymbol{x}$ in space is determined by the statistics of the underlying random process $\boldsymbol{a}_{\boldsymbol{k}}(t)$, while its time correlation is fixed by the time correlation of $\boldsymbol{a}_{\boldsymbol{k}}(t)$. The spatial correlation $G(\boldsymbol{x})$, on the other hand, depends only on the choice of the function $f(\boldsymbol{k})$. These conclusions apply in a similar way to the higher moments of $\boldsymbol{\phi}(\boldsymbol{x},t)$.

The above construction allows to generate random fields with a large variety of different statistics. Generalisations of the procedure using $\boldsymbol{k}$-dependent processes $\boldsymbol{a}_{\boldsymbol{k}}(t)$ are straightforward in principle. In the rest of this work, we choose $\boldsymbol{a}_{\boldsymbol{k}}(t)$ to be independent Ornstein-Uhlenbeck processes. Their components have Gaussian statistics and individual realisations are solutions of the stochastic differential equations

$$\dot{a}_{i,\boldsymbol{k}}(t) = -\frac{a_{i,\boldsymbol{k}}(t)}{\tau} + \sqrt{2D}\,\xi_{i,\boldsymbol{k}}(t), \tag{1.9}$$

where $\xi_{i,\boldsymbol{k}}(t)$ are complex Gaussian white noises with correlation

$$\langle \xi_{i,\boldsymbol{k}}(t)\xi^*_{j,\boldsymbol{l}}(s)\rangle = \delta_{ij}\delta_{\boldsymbol{kl}}\delta(t-s). \tag{1.10}$$

Choosing Ornstein-Uhlenbeck processes for $\boldsymbol{a}_{\boldsymbol{k}}(t)$ renders $\boldsymbol{\phi}(\boldsymbol{x},t)$ Gaussian with time correlation

$$C(|t-s|) = 2\tau^{-1}\mathrm{e}^{-|t-s|/\tau}, \tag{1.11}$$

which implies that τ is the correlation time of $\boldsymbol{\phi}(\boldsymbol{x},t)$. A convenient choice for $f(\boldsymbol{k})$ is $f(\boldsymbol{k}) = \mathrm{e}^{-\eta^2 k^2/4}$, for which we obtain the spatial correlation

$$G(\boldsymbol{x}) \sim \eta^{-d}\mathrm{e}^{-x^2/(2\eta^2)} \tag{1.12}$$

in the limit $L \to \infty$.

Using Gaussian statistics has the advantage of being computationally convenient. However, turbulence fluid velocities can be shown to be highly

non-Gaussian in the dissipative range, due to 'intermittency' [23] which describes sudden strong outbursts of turbulent fluctuations. Furthermore, real turbulence exhibits long-lived regions of high vorticity, so-called vortex tubes [32] that are absent in the statistical model. Finally, the dissipation in Eq. (1.1) and, hence, the Richardson cascade break time-reversal symmetry in turbulence [23], while the statistical model is time-reversal symmetric [1]. These shortcomings of the statistical model have measurable consequences when compared *quantitatively* to direct numerical simulations [1]. The simplicity of the model and its ability of *qualitatively* explaining more complicated systems makes it, however, attractive for further studies.

A more detailed account on the construction of the random flow, including also higher-order correlations $\boldsymbol{\phi}$ is found in Refs. [1, 33].

1.4 Particle motion in a fluid

As the second part of our problem, we need to understand how particles move in a generic flow. That is, we require the forces that act on the particles for a given flow field. Depending on how large the impact of the presence of the particle on the flow field is, the non-linear term $(\boldsymbol{w}\cdot\nabla)\boldsymbol{w}$ can become relevant. Reliable analytical expressions for the force on the particle can be formulated only for laminar flows when the particle moves slowly relative to the fluid [19, 20, 34]. For these flows, the Reynolds number associated to the particle motion, is small.

1.4.1 Low-Reynolds-number flows

In order to know when the force on a particle generated by a laminar flow is a good approximation in turbulence, we need to compare the size of the non-linear term in Eq. (1.1a) to that of the other terms. This is done by considering the particle Reynolds number Re_p, which is obtained from using Eq. (1.2) with the size a of the particle as the length scale and its velocity v_0 relative to the flow as the velocity scale. We obtain

$$\mathrm{Re}_\mathrm{p} = v_0 a/\nu. \tag{1.13}$$

Naively, when $\mathrm{Re}_\mathrm{p} \ll 1$ the left hand of Eq. (1.3) is negligible and we can consider the so-called Stokes equation [19, 20]

$$\nabla p + \nabla^2 \boldsymbol{w} = 0. \tag{1.14}$$

A more detailed analysis, however, reveals that the left-hand side of Eq. (1.3) is a singular perturbation to Eq. (1.14) [35]. One way of solving such boundary-layer problems is by using matched asymptotic expansions [36, 37]. Applying this method one solves two or sometimes even more different perturbation problems in- and outside the boundary layer(s) and matches them together. This method allows to obtain the force on a spherical particle given the unperturbed ambient flow without the particle [35]. For a very small particle, that moves slowly relative to the flow and is much denser than fluid, it is a good approximation to use a constant ambient flow to calculate the force [1]. The corresponding equation for the force is known as Stokes law [19, 20]

$$\boldsymbol{F} = 6\pi\nu\rho_{\mathrm{f}}a(\boldsymbol{w}(\boldsymbol{x},t)-\boldsymbol{v}(t)), \tag{1.15}$$

where ρ_{f} denotes the fluid density. Note that we have neglected gravity [38, 39, 40, 41] because we solely focus on inertial effects here. The linearity of Eq. (1.15) in $\boldsymbol{w}(\boldsymbol{x},t)$ makes the problem tractable both numerically and, in some cases, even analytically.

1.5 The statistical model

We are now in the position to formulate the system of equations that makes up the statistical model for turbulent aerosols [1]. Using Stokes law (1.15) with the fluid velocity field $\boldsymbol{w}(\boldsymbol{x},t)$ replaced by the random velocity field $\boldsymbol{u}(\boldsymbol{x},t)$, we obtain the equations of motion for a single particle

$$\tfrac{\mathrm{d}}{\mathrm{d}t}\boldsymbol{x}(t) = \boldsymbol{v}(t), \tag{1.16a}$$

$$\tfrac{\mathrm{d}}{\mathrm{d}t}\boldsymbol{v}(t) = \gamma(\boldsymbol{u}(\boldsymbol{x}(t),t)-\boldsymbol{v}(t)), \tag{1.16b}$$

where $\gamma = 9/2(\rho_{\mathrm{f}}/\rho_{\mathrm{p}})(\nu/a^2)$ is called the viscous damping and ρ_{p} is the density of the particle. The random velocity field $\boldsymbol{u}(\boldsymbol{x},t)$ has the first and second moments (see Section 1.3.3)

$$\langle \boldsymbol{u}(\boldsymbol{x},t)\rangle = 0 \tag{1.17a}$$

$$\langle u_i(\boldsymbol{x},t)u_j(\boldsymbol{y},t)\rangle = u_0^2\left[1-\frac{(\boldsymbol{x}-\boldsymbol{y})^2}{\eta^2}\right]\delta_{ij}\mathrm{e}^{-(\boldsymbol{x}-\boldsymbol{y})^2/(2\eta^2)}\mathrm{e}^{-|t-s|/\tau}. \tag{1.17b}$$

Because $\boldsymbol{u}(\boldsymbol{x},t)$ is taken to be Gaussian, its statistics is completely described by Eqs. (1.17). Recall from Section 1.2 that we treat the interaction of the

particle with the fluid within the one-way coupling approximation, so that adding additional non-interacting particles to the fluid does not alter the equations. In particular, we can define a whole ensemble of particles and treat them as the field $\boldsymbol{x}(t) = \boldsymbol{x}(\boldsymbol{x}_0, t)$ which maps an initial particle position $\boldsymbol{x}_0$ at some initial time t_0 to a final position $\boldsymbol{x}(t)$ at time t. This particle field has an associated velocity field that we call $\boldsymbol{v}(\boldsymbol{x}(t), t) = \partial_t \boldsymbol{x}(\boldsymbol{x}_0, t)$. These two fields satisfy the same equations of motion as the single particle in Eq. (1.16). We have

$$\frac{\mathrm{d}}{\mathrm{d}t}\boldsymbol{x}(\boldsymbol{x}_0, t) = \boldsymbol{v}(\boldsymbol{x}(t), t), \tag{1.18a}$$

$$\frac{\mathrm{d}}{\mathrm{d}t}\boldsymbol{v}(\boldsymbol{x}(t), t) = \gamma(\boldsymbol{u}(\boldsymbol{x}(t), t) - \boldsymbol{v}(\boldsymbol{x}(t), t)). \tag{1.18b}$$

From now on, we use the short-hand notation $\boldsymbol{x}(t) = \boldsymbol{x}(\boldsymbol{x}_0, t)$ and $\boldsymbol{v}(t) = \boldsymbol{v}(\boldsymbol{x}(t), t)$. It is worth mentioning that the fields $\boldsymbol{x}(t)$ and $\boldsymbol{v}(t)$ are in general multivalued [6, 7, 8], due to caustics in the particle dynamics described later. For most purposes in this work, it is convenient to also consider the equations of motion for the tensor quantities [1, 6, 42]

$$\mathbb{J}(t) = \mathbb{J}(\boldsymbol{x}(t), t) = \frac{\partial \boldsymbol{x}(\boldsymbol{x}_0, t)}{\partial \boldsymbol{x}_0}, \tag{1.19a}$$

$$\mathbb{Z}(t) = \mathbb{Z}(\boldsymbol{x}(t), t) = \frac{\partial \boldsymbol{v}(\boldsymbol{x}(t), t)}{\partial \boldsymbol{x}(t)}, \tag{1.19b}$$

in addition to Eqs. (1.16). Taking partial derivatives of Eqs. (1.18) with respect to $\boldsymbol{x}_0$ and $\boldsymbol{x}(t)$, respectively, and using the definitions (1.19), we obtain

$$\frac{\mathrm{d}}{\mathrm{d}t}\mathbb{J}(t) = \mathbb{Z}(t)\mathbb{J}(t), \tag{1.20a}$$

$$\frac{\mathrm{d}}{\mathrm{d}t}\mathbb{Z}(t) = \gamma[\mathbb{A}(t) - \mathbb{Z}(t)] - \mathbb{Z}(t)^2, \tag{1.20b}$$

where $\mathbb{A}(t) = \partial \boldsymbol{u}(\boldsymbol{x}(t), t)/\partial \boldsymbol{x}(t)$ is the field of fluid velocity gradients. Furthermore, $\mathbb{J}(t)$ has the initial condition $\mathbb{J}(t_0) = \mathbb{1}$.

1.5.1 Dimensionless variables

In our approximation, the whole particle-fluid system depends only on the four parameters γ, u_0, η and τ. Dedimensionalising Eqs. (1.18) with these parameters, one finds that the system is in fact characterised by only two dimensionless numbers which we call the Stokes and the Kubo numbers

[1]. The Stokes number $\mathrm{St} = 1/(\gamma\tau)$ measures the relevance of particle inertia while the Kubo number $\mathrm{Ku} = u_0\tau/\eta$ is a measure for the persistence of the flow. In this short Section, we give an overview over the two dedimensionalisation schemes – we call them the Stokes and the Kubo coordinates – that we will use in the rest of the work. We first perform the coordinate transform $t \to t/\gamma$, $\boldsymbol{u} \to \eta\gamma\boldsymbol{u}$, $\boldsymbol{x} \to \eta\boldsymbol{x}$ and $\boldsymbol{v} \to \eta\gamma\boldsymbol{v}$ and obtain the dimensionless equations [1]

$$\frac{\mathrm{d}}{\mathrm{d}t}\boldsymbol{x}(t) = \boldsymbol{v}(t), \tag{1.21a}$$

$$\frac{\mathrm{d}}{\mathrm{d}t}\boldsymbol{v}(t) = \boldsymbol{u}(\boldsymbol{x}(t),t) - \boldsymbol{v}(t), \tag{1.21b}$$

$$\frac{\mathrm{d}}{\mathrm{d}t}\mathbb{J}(t) = \mathbb{Z}(t)\mathbb{J}(t), \tag{1.21c}$$

$$\frac{\mathrm{d}}{\mathrm{d}t}\mathbb{Z}(t) = \mathbb{A}(t) - \mathbb{Z}(t) - \mathbb{Z}(t)^2, \tag{1.21d}$$

$$\langle u_i(\boldsymbol{x},t)u_j(\boldsymbol{y},t)\rangle = \mathrm{Ku}^2\mathrm{St}^2\left[1-(\boldsymbol{x}-\boldsymbol{y})^2\right]\delta_{ij}\mathrm{e}^{-(\boldsymbol{x}-\boldsymbol{y})^2/2}\mathrm{e}^{-\mathrm{St}|t-s|}, \tag{1.21e}$$

For lack of a better name, we call this first dedimensionalisation the Stokes coordinates. This scheme is useful because it makes the particle equations of motion independent of Ku and St. A second rescaling of Eqs. (1.16) reads $t \to \tau t$, $\boldsymbol{u} \to u_0\boldsymbol{u}$, $\boldsymbol{x} \to \eta x$ and $\boldsymbol{v} \to u_0\boldsymbol{v}$, and leads to a parameter-independent correlation function. We have [1]

$$\frac{\mathrm{d}}{\mathrm{d}t}\boldsymbol{x}(t) = \mathrm{Ku}\,\boldsymbol{v}(t), \tag{1.22a}$$

$$\frac{\mathrm{d}}{\mathrm{d}t}\boldsymbol{v}(t) = \mathrm{St}^{-1}\left[\boldsymbol{u}(\boldsymbol{x}(t),t) - \boldsymbol{v}(t)\right], \tag{1.22b}$$

$$\frac{\mathrm{d}}{\mathrm{d}t}\mathbb{J}(t) = \mathrm{Ku}\,\mathbb{Z}(t)\mathbb{J}(t) \tag{1.22c}$$

$$\frac{\mathrm{d}}{\mathrm{d}t}\mathbb{Z}(t) = \mathrm{St}^{-1}\left[\mathbb{A}(t) - \mathbb{Z}(t)\right] - \mathrm{Ku}\,\mathbb{Z}(t)^2, \tag{1.22d}$$

$$\langle u_i(\boldsymbol{x},t)u_j(\boldsymbol{y},t)\rangle = \left[1-(\boldsymbol{x}-\boldsymbol{y})^2\right]\delta_{ij}\mathrm{e}^{-(\boldsymbol{x}-\boldsymbol{y})^2/2}\mathrm{e}^{-|t-s|}. \tag{1.22e}$$

We call the coordinates that correspond to Eqs. (1.22) Kubo coordinates, because they are used in an approximation scheme called the Kubo expansion [1, 43]. Both sets of dimensionless variables are used in this work, because each of them is convenient for different purposes.

We have come a long way from considering the very complicated problem of inertial particles in turbulence to the equations of motion for a field of particles in a random velocity field. The next Sections will teach us how rich the dynamics of Eqs. (1.20)-(1.22) is, even after the drastic simplifications we have made. Furthermore, comparisons with the results of direct numerical simulations summarised in Ref. [1] suggest that the statistical model

is capable of explaining these results *qualitatively* and in some cases even *quantitatively*.

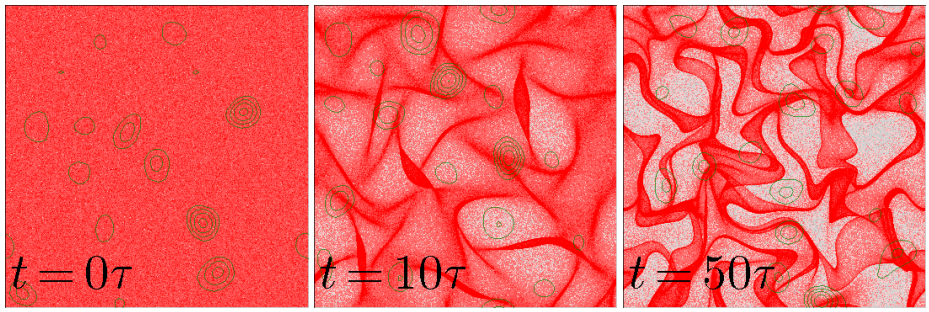

Figure 2.1: An initially homogeneous distribution of inertial particles (red) clusters in a random flow. The green lines are level lines of fluid vorticity. The Kubo and Stokes numbers are 0.1 and 10, respectively. The Figures were generated by Kristian Gustavsson and are used with permission.

2 Spatial clustering

Spatial clustering describes the formation of regions of high concentration of aerosol particles [11, 13, 14, 44, 45, 46]. Neutrally buoyant, infinitesimally small particles, called tracers, distribute homogeneously over space if the underlying turbulent flow is incompressible [26]. This is because the particle motion is restricted to the stream lines of the flow. For aerosol particles which are heavier than the fluid, this is no longer true. In this case, the particles may detach from the flow. This implies that the particle dynamics takes place in the higher-dimensional phase space and gives rise to a whole spectrum of different competing mechanisms that eventually contribute to particle clustering. Fig. 2.1 shows how an initially homogeneously distributed set of heavy (red) particles at $t = 0$ (left panel) forms regions of high and low concentration over the course of 50 fluid correlation times τ. Clustering increases the probability of particles to come close together, thereby drastically increasing collision rates [2, 13]. This is important in turbulent air clouds, where the formation of regions of high water droplet concentration is believed to increase the probability of droplet collisions, and hence facilitate droplet growth [2, 4, 26].

In this Chapter we first discuss the physical mechanisms behind particle clustering. After that we introduce observables that characterise the phenomenon and explain in which way they are relevant.

2.1 Origins of clustering

There are three main mechanisms that are known to be important for spatial particle clustering in incompressible flows. These are preferential concentration, phase-space contraction and multiplicative amplification, and caustics [1]. We explain these mechanisms in the following and briefly mention the effect of flow compressibility which is relevant in the one-dimensional models.

2.1.1 Preferential concentration

As discussed in Section 1.3, turbulence can be seen as an ensemble of vortices of different sizes. Loosely speaking, these vortices force tracer particles to roughly follow circular orbits. Heavy particles, on the other hand, spiral out of vortices because of centripetal forces, and they accumulate in regions of low vorticity and high strain. This was first noted by Maxey [39] who used an expansion around the limit $\mathrm{St}=0$, to argue for this. His approach is sketched in what follows. We start with the equations of motion in Kubo coordinates

$$\frac{\mathrm{d}}{\mathrm{d}t}\boldsymbol{x}(t)=\mathrm{Ku}\,\boldsymbol{v}(t), \tag{2.1a}$$

$$\frac{\mathrm{d}}{\mathrm{d}t}\boldsymbol{v}(t)=\mathrm{St}^{-1}\left[\boldsymbol{u}(\boldsymbol{x}(t),t)-\boldsymbol{v}(t)\right], \tag{2.1b}$$

$$\frac{\mathrm{d}}{\mathrm{d}t}\mathbb{J}(t)=\mathrm{Ku}\,\mathbb{Z}(t)\mathbb{J}(t) \tag{2.1c}$$

$$\frac{\mathrm{d}}{\mathrm{d}t}\mathbb{Z}(t)=\mathrm{St}^{-1}\left[\mathbb{A}(t)-\mathbb{Z}(t)\right]-\mathrm{Ku}\,\mathbb{Z}(t)^2, \tag{2.1d}$$

and treat the Stokes number as small. We take the underlying flow field to be incompressible and assume that all quantities can be expanded in a power series in St, the smallest order being the dynamics of tracer particles. Substituting these series expansions into Eq. (2.1), we can evaluate order by order in St and obtain a hierarchy of equations, one for each order in St. A perturbative solution for $\mathbb{Z}(t)$ can now be straightforwardly obtained. One finds to order $\mathscr{O}(\mathrm{St})$ [1, 39]

$$\mathbb{Z}(t)\sim\mathbb{A}^{(0)}(t)+\mathrm{St}\left\{\mathbb{A}^{(1)}(t)-\tfrac{\mathrm{d}}{\mathrm{d}t}\mathbb{A}^{(0)}(t)-\mathrm{Ku}\left[\mathbb{A}^{(0)}(t)\right]^2\right\}, \tag{2.2}$$

where $\mathbb{A}^{(i)}(t)=\partial^i_{\mathrm{St}}\mathbb{A}(\boldsymbol{x}(t),t)|_{\mathrm{St}=0}$. Taking the trace of Eq. (2.2), Maxey [39] found that

$$\nabla\cdot\boldsymbol{v}\sim-\mathrm{Ku}\,\mathrm{St}\,\mathrm{Tr}\left[\mathbb{A}^{(0)}(t)\right]^2=\mathrm{Ku}\,\mathrm{St}(\mathrm{Tr}\,\mathbb{O}^{(0)}\mathbb{O}^{(0)T}-\mathrm{Tr}\,\mathbb{S}^{(0)}\mathbb{S}^{(0)T}), \tag{2.3}$$

where it was used that $\mathrm{Tr}\mathbb{Z} = \nabla \cdot \boldsymbol{v}$. Here, $\mathbb{O}^{(0)}$ and $\mathbb{S}^{(0)}$ are the vorticity and strain of the fluid velocity field at $\boldsymbol{x}(t)$ and time t. Hence, straining regions, where $\mathrm{Tr}\mathbb{S}\mathbb{S}^T > \mathrm{Tr}\mathbb{O}\mathbb{O}^T$, are sinks of the particle velocity field while regions of high vorticity act as sources. As a result, weakly inertial particles tend to accumulate in straining regions of the flow in accordance with the intuitive picture discussed earlier [1]. Note that the result (2.3) suggests that the effect of preferential concentration is proportional to the Kubo number. This is intuitively clear recalling that Ku measures the persistence of the flow. In a memoryless flow with $\mathrm{Ku} \to 0$, the aerosol particles react too slowly to changes of the flow as to be able to accumulate in straining regions.

A conceptual problem with perturbative expansions of this kind is that the representation of the particle velocity field as a simple function of the smooth flow fields $\mathbb{A}^{(i)}(t)$ explicitly excludes particle-trajectory crossings. These crossings become relevant for larger St numbers and appear due to caustics in the particle phase-space dynamics. We discuss caustics in Section 2.1.3.

2.1.2 Phase-space contraction

The equations of motion governing the particle motion in aerosols are dissipative, which means that energy brought into the system eventually leaves it again. Dissipative systems have the property that their phase space volume decreases with time [31]. Consider the equations of motion in Kubo coordinates, Eq. (2.1). Phase-space contraction is quantified by the divergence of the flow, $\mathrm{div}[(\dot{\boldsymbol{x}}(t), \dot{\boldsymbol{v}}(t))]$, taken with respect to the pair $(\boldsymbol{x}(t), \boldsymbol{v}(t))$. We obtain

$$\mathrm{div}[(\dot{\boldsymbol{x}}(t), \dot{\boldsymbol{v}}(t))] = \mathrm{Ku} \sum_{i=1}^{d} \frac{\partial v_i(t)}{\partial x_i(t)} + \frac{1}{\mathrm{St}} \sum_{i=1}^{d} \left(\frac{\partial u_i(\boldsymbol{x}(t), t)}{\partial v_i(t)} - \frac{\partial v_i(t)}{\partial v_i(t)} \right) = -\frac{d}{\mathrm{St}} < 0 \,. \quad (2.4)$$

First, we observe that the divergence of the flow is negative and independent of the coordinates and of time. It follows that phase space volumes $\mathscr{W}_t$ evolve according to

$$\mathscr{W}_t = \mathscr{W}_{t_0} \mathrm{e}^{\int_{t_0}^{t} \mathrm{div}[(\dot{\boldsymbol{x}}(t), \dot{\boldsymbol{v}}(t))] \mathrm{d}t} = \mathscr{W}_{t_0} \mathrm{e}^{-\frac{d}{\mathrm{St}}(t - t_0)} \,. \quad (2.5)$$

Thus phase space volumes contract exponentially. The same is true for *spatial* volumes of particles $\mathscr{V}_t = \det \mathbb{J}(t)$ that evolve according to the flow

(2.1), due to a related phenomenon called multiplicative amplification [1]. Multiplicative amplification and phase-space contraction are naturally described by means of Lyapunov exponents [1, 45, 47], which we discuss in Section 2.2.2.

2.1.3 Caustics

Another mechanism that we know is relevant for spatial clustering is the occurrence of caustics [6, 7, 8, 15]. Caustics are singularities in the projection of the phase-space manifold on the coordinate space. Roughly speaking, because the dynamics of inertial particles takes place in $2d$ dimensional phase space, both the particle field $\boldsymbol{x}(\boldsymbol{x}_0, t)$ and its corresponding velocity field $\boldsymbol{v}(\boldsymbol{x}(t), t)$ are in general multivalued functions with respect to the d-dimensional coordinate space. Caustics have important consequences for the particle distribution. At the 'caustic lines', the tangent space of the phase-space manifold is perpendicular to the coordinate space. This implies that the particle density diverges in a square-root fashion and the probability of finding particles close to each other is strongly increased at the caustic lines [7]. The left panel in Fig. 2.2 shows caustic lines for inertial particles (in red) in a two-dimensional random flow. The right panel depicts schematically how a caustic line is created at the point x_c, where $\partial v(x,t)/\partial x$ diverges. In addition to its importance for spatial clustering, the multi-valuedness of the particle field also allows for large relative velocities between nearby particles [6, 7, 8]. For this reason, some authors call the occurrence of caustics the 'sling effect' [6, 15]: Particles may be strongly accelerated in different regions in space to come together at high relative velocity. Locally, we can define a caustic as the event that the Jacobian of the particle field $\mathbb{J}(t)$ becomes singular at finite time t_c:

$$\det \mathbb{J}(t_c) = 0\,. \tag{2.6}$$

This is equivalent to saying that the volume of the spatial parallelepiped spanned by nearby particles collapses to zero [1]. We can express this condition in terms of $\mathbb{Z}(t)$ by taking a time-derivative of $\det \mathbb{J}(t)$ and using the equation of motion (2.1c). We obtain

$$\tfrac{\mathrm{d}}{\mathrm{d}t} \det \mathbb{J}(t) = \det \mathbb{J}_t \operatorname{Tr}\left[\mathbb{J}^{-1}\dot{\mathbb{J}}\right] = \mathrm{Ku} \det \mathbb{J}(t) \operatorname{Tr} \mathbb{Z}(t)\,. \tag{2.7}$$

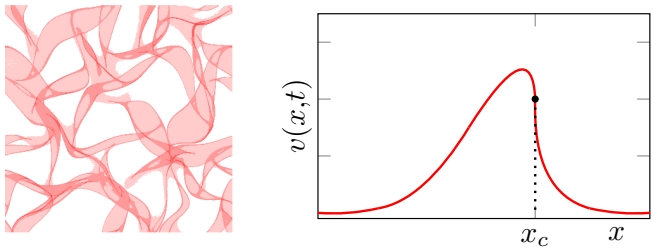

Figure 2.2: *Left:* Distribution of inertial particles in a two dimensional random flow. Caustic lines are the dark-red regions of high particle density. The figure is taken from [1] with permission. *Right:* One-dimensional schematic of the creation of a caustic at x_c.

Because $\mathbb{J}(t_0) = \mathbb{1}$ we find for $\det \mathbb{J}(t)$ as a function of $\mathbb{Z}(t)$ [1]

$$\det \mathbb{J}(t) = \mathrm{e}^{\mathrm{Ku} \int_{t_0}^{t} \mathrm{Tr}\,\mathbb{Z}(s)\mathrm{d}s}, \tag{2.8}$$

which implies that the event of caustic formation can be expressed as

$$\int_{t_0}^{t_c} \mathrm{Tr}\,\mathbb{Z}(s)\mathrm{d}s \to -\infty, \tag{2.9}$$

at finite time $t_c < \infty$.

2.1.4 Compressibility of the underlying flow

Because the models that we discuss in Chapters 3 are one-dimensional, their underlying flow must be compressible. A compressible flow leads to strong clustering of the immersed particles. This is true even for tracer particles with $\mathrm{St} = 0$, which can be seen by taking the trace of Eq. (2.2). We have

$$\mathrm{Tr}\,\mathbb{Z}(t) = \nabla \cdot \boldsymbol{v}(t) \sim \mathrm{Tr}\,\mathbb{A}^{(0)}(t) = \nabla \cdot \boldsymbol{u}(\boldsymbol{x}^{(0)}(t), t), \tag{2.10}$$

to lowest order in the Stokes number. Recall that $\boldsymbol{x}^{(0)}(t)$ is the field of inertialess tracer particles. Consequently, coordinate space volumes, which are measured by $\det \mathbb{J}(t)$, shrink at sinks where $\nabla \cdot \boldsymbol{u}(\boldsymbol{x}(t), t) < 0$. For weak inertia, clustering that is due to the compressibility of the underlying flow is characterised by a 'path-coalescence' regime [16] in which the phase-space manifold contracts to a point. For larger Stokes numbers, a phase transition occurs and the particles behave essentially as in an incompressible flow [16, 48].

2.2 Quantities that characterise spatial clustering

We now discuss three different observables that measure clustering in different ways. These are the spectrum of fractal dimensions D_q, the statistics of the finite-time Lyapunov exponents λ_t and the rate of caustic formation J.

2.2.1 Fractal dimension spectrum

Spatial clustering is characterised by inhomogeneities in the spatial distribution of aerosol particles [1, 13, 14, 30]. One way of characterising these inhomogeneities is by calculating the fractal dimension spectrum [12, 49, 50].

In order to define the most intuitive representative of the spectrum, the 'box-counting' dimension D_0, we discretise the space into small boxes of side length $\epsilon \ll 1$ and consider a large but finite number $N \gg 1$ of particles. For a homogeneous particle distribution, the expected minimum number of boxes $\langle \mathcal{N}(\boldsymbol{\varepsilon}) \rangle$ of side length ϵ needed to cover the set $\mathcal{S}$ of N particles scales as the box-size raised to the power $-d$, $\langle \mathcal{N}(\epsilon) \rangle \sim \epsilon^{-d}$. If the particle density is non-homogeneous, less boxes are needed and the scaling exponent is smaller than d. The box-counting dimension D_0 is defined by [51]

$$\langle \mathcal{N}(\epsilon) \rangle \sim \epsilon^{-D_0}, \quad \epsilon \ll 1. \tag{2.11}$$

The box-counting dimension measures, roughly speaking, how space-filling a fractal is [51, 52]. In many cases, in particular if a fractal is generated by a set of underlying equations of motion, it is furthermore equipped with a non-trivial measure, called the natural measure μ [31]. The latter contains information not only about *if* regions on the fractal are visited by the particles but also *how often* that happens. In order to study the natural measure on the fractal, we consider the probability $\mu(\boldsymbol{x}(t), \epsilon)$ that a sphere of radius $\boldsymbol{\varepsilon}$ centered at $\boldsymbol{x}(t)$ is visited by a particle. The spectrum of fractal dimensions D_q is defined in terms of the scaling relation [52]

$$\left\langle \int_{\mathcal{S}_t} \mu(\boldsymbol{x}(t), \epsilon)^{q-1} \mathrm{d}\mu(\boldsymbol{x}(t), \epsilon) \right\rangle \sim \epsilon^{(q-1)D_q}, \quad \epsilon \ll 1. \tag{2.12}$$

The integral is performed over the fractal set $\mathcal{S}_t$ at time t and the bracket $\langle \cdot \rangle$ denotes a time average. The quantity D_q is called Rényi dimension or

generalised fractal dimension [52]. From Eq. (2.12) we obtain

$$D_q = \lim_{\epsilon\to 0} \frac{1}{q-1} \frac{\log\left\langle \int_{\mathscr{S}_t} \mu(\boldsymbol{x}(t),\epsilon)^{q-1} \mathrm{d}\mu(\boldsymbol{x}(t),\epsilon)\right\rangle}{\log\epsilon}. \tag{2.13}$$

The most important fractal dimension in the present context is the correlation dimension, D_2 [13, 53, 54]. Setting $q=2$ in Eq. (2.13) we obtain

$$D_2 = \lim_{\epsilon\to 0} \frac{\left\langle \int_{\mathscr{S}_t} \mu(\boldsymbol{x}(t),\epsilon) \mathrm{d}\mu(\boldsymbol{x}(t),\epsilon)\right\rangle}{\log\epsilon}. \tag{2.14}$$

The correlation dimension is of great importance for physical particle systems, because it measures the probability of finding a second particle in a ball of radius ϵ around a reference particle [55]. That is why a convenient way of formulating Eq. (2.14), is by considering the statistics of separations of a particle pair, $Y^{(2)}(t) = \|\boldsymbol{x}_1(t) - \boldsymbol{x}_2(t)\|$. For this quantity it follows from Eq. (2.12) that [52]

$$P(Y^{(2)}(t) \le \epsilon) \sim \epsilon^{D_2}, \qquad \epsilon \ll 1. \tag{2.15}$$

More generally, consider the positions of $q \ge 2$ particles $\boldsymbol{x}_i(t)$, $i = 1,\ldots,q$, and define the quantity

$$Y^{(q)}(t) = \max_{i,j\in S_q} \{\|\boldsymbol{x}_i(t) - \boldsymbol{x}_j(t)\|\}, \tag{2.16}$$

where S_q denotes the index set $S_q = \{1,\ldots,q\}$. It can be shown [12, 52] that $Y^{(q)}(t)$ obeys the scaling relation

$$P(Y^{(q)}(t) \le \epsilon) \sim \epsilon^{D_q(q-1)}, \qquad \epsilon \ll 1, \tag{2.17}$$

for $q \ge 2$. In the majority of this work, we study the correlation dimension D_2. The other fractal dimensions are studied for $q > 2$ in paper C, where a simple relation between the different fractal dimensions is found for a particular model.

2.2.2 Finite-time Lyapunov exponents

The relative spatial dynamics of nearby particles is characterised by stretching and folding due to the random fluid velocity gradients. The transients

of these deformations are important for clustering and are described by the spatial finite-time Lyapunov exponents (FTLE) [1, 12, 18, 26, 45]. The spatial FTLE are obtained from the eigenvalues of $\mathbb{J}(t)$, which we call $\Lambda_k(t)$ with $k = 1,\dots,d$. In the limit $t \to \infty$, the absolute values of these multipliers, $|\Lambda_k(t)|$, typically scale exponentially with characteristic (Lyapunov) exponent λ_k. For large enough but finite times, the $|\Lambda_k(t)|$ are stochastic processes with exponents $\lambda_k(t)$:

$$|\Lambda_k(t)| \sim \mathrm{e}^{\lambda_k(t)t}, \quad k = 1,\dots,d\,. \tag{2.18}$$

The processes $\lambda_k(t)$ are called the spatial finite-time Lyapunov exponents (FTLE) of the system [26, 56]. The spatial FTLE approach the spatial Lyapunov exponents in the limit $t \to \infty$, $\lambda_k(t) \to \lambda_k$. In terms of the multipliers $\Lambda_k(t)$, the FTLE are expressed as $\lambda_k(t) = t^{-1}\log|\Lambda_k(t)|$. Furthermore, using Eqs. (2.8) and (2.18) we obtain

$$\sum_{k=1}^{d}\lambda_k(t) = \frac{\mathrm{Ku}}{t}\int_0^t \mathrm{Tr}\,\mathbb{Z}(t)\,\mathrm{d}t\,. \tag{2.19}$$

In the infinite-time limit we can thus find a simple expression for the sum of spatial Lyapunov exponents according to

$$\sum_{k=1}^{d}\lambda_k = \lim_{t\to\infty}\frac{\mathrm{Ku}}{t}\int_0^t \mathrm{Tr}\,\mathbb{Z}(t)\,\mathrm{d}t = \mathrm{Ku}\,\langle \mathrm{Tr}\,\mathbb{Z}\rangle\,, \tag{2.20}$$

where the the expectation value in the last equality is taken with respect to the natural measure of the dynamics.

The model systems in Chapter 3 are all one-dimensional, $d = 1$, so that Eqs. (2.19) and (2.20) in fact are expressions for the only spatial FTLE and Lyapunov exponent of the theory, respectively. That is why these equations are particularly important here. In systems with $d > 1$, the sum of all spatial Lyapunov exponents describes how spatial volumes expand ($\sum_{k=1}^{d}\lambda_k > 0$) or contract ($\sum_{k=1}^{d}\lambda_k < 0$). For a complete description of local stretching and compression, however, the whole set of Lyapunov exponents is required. In Section 2.1.2 we noted that phase-space volumes $\mathscr{W}_t$ of particles tend to contract under the flow at a constant exponential rate. In terms of the Lyapunov exponents Eq. (2.5) implies that the sum of all phase-space Lyapunov exponents sums up to $-d/\mathrm{St}$.

The statistics of the spatial FTLE is studied in terms of their joint probability density function $P(\boldsymbol{\lambda}(t)=\boldsymbol{s})$ where $\boldsymbol{\lambda}(t)=(\lambda_1(t),\ldots,\lambda_d(t))$. For large times, $t\gg 1$, $P(\boldsymbol{\lambda}(t)=\boldsymbol{s})$ takes the large deviation form [57]

$$P(\boldsymbol{\lambda}(t)=\boldsymbol{s})\approx \exp\left[-t\,I(\boldsymbol{s})\right], \qquad t\gg 1, \tag{2.21}$$

where $I(\boldsymbol{s})$ is called the rate function of the process $\boldsymbol{\lambda}(t)$. In one dimension, $d=1$, there is a simple relation between the rate function for the FTLE and the correlation dimension of the system that is discussed in Chapter 3 and Appendix A.

2.2.3 Rate of caustic formation

In Section 2.1.3 we showed that a caustic forms when the integral $\int_{t_0}^{t_c}\mathrm{Tr}\,\mathbb{Z}(s)\mathrm{d}s$ tends to $-\infty$ in finite time $t_c<\infty$. Similarly to the FTLEs discussed in the previous section we treat t_c as a random variable. We call t_i the time between the i^{th} and $(i-1)^{\text{th}}$ caustic event. The number $N(t)$ of caustics that have occurred at time $t>0$ can then be written as

$$N(t):=\max\{n: T_n\le t\}, \tag{2.22}$$

where $T_n=\sum_{i=1}^{n} t_i$. For systems with sufficiently quickly decaying correlation functions, we may assume ergodicity so that $N(t)$ constitutes a so-called renewal process [58]. For renewal processes one can prove that [58]

$$\frac{N(t)}{t}\to\frac{1}{\langle t_i\rangle}, \qquad \text{for} \qquad t\to\infty. \tag{2.23}$$

We call the limit in this equation J, the rate of caustic formation

$$J=\frac{1}{\langle t_i\rangle}=\lim_{t\to\infty}\frac{N(t)}{t}. \tag{2.24}$$

The rate of caustic formation is a measure for the importance of caustics for spatial clustering in a given system. Typically, caustics are negligible against the other clustering mechanisms when Ku and/or St are small. In this case, J shows an exponentially small activation of the type [1, 7, 8, 15]

$$J\sim \mathrm{e}^{-1/f(\mathrm{Ku},\mathrm{St})}, \tag{2.25}$$

where f is a function Ku and St. The explicit form of f is known analytically only for one-dimensional models in specific limits of Ku and St [7, 43]. We discuss these results in Section 3.4.1.

3 One-dimensional systems

In this Chapter we introduce the one-dimensional statistical models, which we use to study the observables defined in the previous Chapter. In one spatial dimension, the statistical model is much simpler than in two and three dimensions and allows for analytical treatment in limiting cases. The equations of motion in Kubo coordinates, Eq. (1.21), read in one dimension:

$$\frac{\mathrm{d}}{\mathrm{d}t}x(t) = \mathrm{Ku}\, v(t), \tag{3.1a}$$

$$\frac{\mathrm{d}}{\mathrm{d}t}v(t) = \mathrm{St}^{-1}\left[u(\boldsymbol{x}(t),t) - v(t)\right], \tag{3.1b}$$

$$\frac{\mathrm{d}}{\mathrm{d}t}j(t) = \mathrm{Ku}\, z(t) j(t), \tag{3.1c}$$

$$\frac{\mathrm{d}}{\mathrm{d}t}z(t) = \mathrm{St}^{-1}\left[A(x(t),t) - z(t)\right] - \mathrm{Ku}\, z(t)^2. \tag{3.1d}$$

Note that all field quantities are now scalars. The one-dimensional matrix of spatial deformations, $j(t) = \partial x(x_0,t)/\partial x_0$ can alternatively be described by the separation $|\Delta x(t)| = |x_1(t) - x_2(t)|$ of a closeby particle pair which has the same dynamics as $j(t)$ [1].

We now briefly discuss the implications of reduced dimensionality for the calculation of the observables discussed in Section 2.2. We start by considering the computation of the spatial FTLE. Because there is only one spatial FTLE in one dimension, Eq. (2.19) turns into the simple equation

$$\lambda(t) = \frac{1}{t}\int_0^t z(s)\mathrm{d}s\,. \tag{3.2a}$$

Consequently, from Eq. (2.20) we get for the Lyapunov exponent

$$\lambda = \lim_{t\to\infty}\lambda(t) = \langle z\rangle\,. \tag{3.3}$$

Eq. (2.9) translates into the one-dimensional caustic condition

$$\int_0^{t_c} z(s)\mathrm{d}s \to -\infty\,. \tag{3.4}$$

3.1 Generic behaviour

Equation (3.4) implies that a necessary condition for caustic formation is that $z(t) \to -\infty$ in finite time. In one dimension, this means that the dynamics of

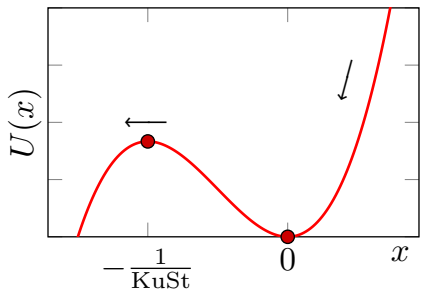

Figure 3.1: The z-coordinate moves in the potential $U(x)$, leading to a finite flux towards $z=-\infty$.

$z(t)$ needs to exhibit finite-time singularities. How these caustic singularities arise becomes clear by writing Eq. (3.1d) as

$$\frac{\mathrm{d}}{\mathrm{d}t}z(t) = -U'(z(t)) + \mathrm{St}^{-1}A(t), \tag{3.5}$$

with the potential $U(x) = \frac{\mathrm{St}^{-1}}{2}x^2 + \frac{\mathrm{Ku}}{3}x^3$. Figure 3.1 schematically shows U as a function of x. If we disregard for the moment the contribution of $A(t)$, the z-dynamics $U(x)$ has a stable fixed point at $x=0$ and an unstable one at $x=-1/(\mathrm{KuSt})$ [1]. The fixed points are shown as the red dots in Fig. 3.1. For finite and large enough values of $A(t)$, the z-coordinate can pass the unstable fixed point and escape to $-\infty$ [6, 16]. A closer analysis of the equation of motion (3.1d) shows that the singularity $z \to -\infty$ is reached in finite time and is not integrable, thus leading to a caustic by Eq. (3.4). We know from Eq. (2.8) that $j(t)$ goes to zero at a caustic, $j(t_c)=0$. For $t > t_c$, $j(t)$ must become positive again which requires that $z(t)$ is, immediately after a caustic, injected back at $+\infty$.

We conclude that $z(t)$ obeys the following dynamics: For small $A(t)$, the z-coordinate spends most of its time close to the origin. When $A(t)$ becomes larger it is more likely that $z(t)$ passes the unstable fixed point at $z=-1/(\mathrm{KuSt})$ and escapes to $-\infty$. Due to the periodic boundary conditions $z(t)$ eventually returns to the origin $z=0$ after a caustic event. Hence, after a long enough time, $z(t)$ reaches a non-equilibrium steady state characterised by a constant negative flux.

3.2 Statistical models in one dimension

In one dimension the Fourier sum (1.4) for $u(x,t)$ discussed in Section 1.5, reads in Kubo coordinates

$$u(x,t) = \partial_x \phi(x,t) = N \sum_{k=-\infty}^{\infty} ik\, a_k(t) \mathrm{e}^{ikx-k^2/4}, \tag{3.6}$$

where $N = \left(\sqrt{2\pi}\eta/L\right)^{1/2}$. Recall that $a_k(t)$ are chosen to be independent Ornstein-Uhlenbeck processes. Consequently, $A(x,t) = \partial_x u(x,t)$ is a Gaussian random field with zero mean and correlation

$$\langle A(x,t)A(y,s)\rangle = \left\{[(x-y)^2-3]^2-6\right\} \mathrm{e}^{-(x-y)^2/2} \mathrm{e}^{-|t-s|}. \tag{3.7}$$

The model is applicable to the whole range of both Ku and St but it is hard to obtain analytical results for it, even in one spatial dimension. In what follows, we introduce three versions of the statistical model for which analytical results can be obtained.

3.2.1 White-noise model

The white-noise model is obtained by using the equations of motion is Stokes coordinates, Eq. (1.21), and simultaneously letting $\mathrm{Ku} \to 0$ and $\mathrm{St} \to \infty$ so that $\varepsilon^2 = 3\mathrm{Ku}^2\mathrm{St}$ remains constant. In the white-noise limit, the correlation function turns into a delta function in time:

$$\langle A(x,t)A(y,s)\rangle \to 2\varepsilon^2 \left\{[(x-y)^2-3]^2-6\right\} \mathrm{e}^{-(x-y)^2/2} \delta(t-s). \tag{3.8}$$

Because the particles move too slowly compared to the flow to accumulate in straining regions, there is no preferential concentration in the white-noise model. Hence, the random field $A(x,t)$ at fixed x has the same statistics as $A(x(t),t)$, which means in turn that $A(t) = \xi_t$, where ξ_t is a Gaussian white-noise [59, 60] with correlation

$$\langle \xi_t \xi_s \rangle = 2\varepsilon^2 \delta(t-s). \tag{3.9}$$

The equations of motion for $j(t)$ and $z(t)$ read in the white-noise model

$$\frac{\mathrm{d}}{\mathrm{d}t} x(t) = z(t)x(t), \tag{3.10a}$$

$$\frac{\mathrm{d}}{\mathrm{d}t} z(t) = \xi_t - z(t) - z^2(t). \tag{3.10b}$$

Modelling $A(t)$ by the Gaussian white-noise ξ_t corresponds to the physical situation of highly inertial particles ($\mathrm{St}\to\infty$) in a very quickly varying flow ($\mathrm{Ku}\to 0$). The set of stochastic differential equations given in Eqns. (3.10) constitutes a Markov system which can be treated using Fokker-Planck equations [59, 60]. This is one of the reasons why the white-noise model has been studied extensively in one [1, 10, 61, 62] and higher dimensions [47, 53, 54, 63].

3.2.2 Telegraph model

In the so-called telegraph model [17] the velocity gradient $A(t)$ is modelled by a telegraph process η_t. The latter is a jump process that takes only two different values, A_0 and $-A_0$, where $A_0>0$ is the amplitude of the process. Transitions from A_0 to $-A_0$ occur with rate ν_- and back from $-A_0$ to A_0 with rate ν_+. For large times, η_t reaches a steady state characterised by the probabilities

$$\lim_{t\to\infty} P\left(\eta_t = A_0\right) = \frac{\nu_+}{\nu}, \qquad \lim_{t\to\infty} P\left(\eta_t = -A_0\right) = \frac{\nu_-}{\nu}, \tag{3.11a}$$

where we denote $\nu \equiv \nu_+ + \nu_-$. The mean value $\mu = \langle \eta_t \rangle$ and correlation function $\langle\!\langle \eta_t \eta_s \rangle\!\rangle = \langle \eta_t \eta_s\rangle - \langle \eta_t\rangle\langle \eta_s\rangle$ for the telegraph process can be obtained explicitly [60]. The steady-state correlation function takes the simple form

$$\langle\!\langle \eta_t \eta_s \rangle\!\rangle = \left(A_0^2 - \mu^2\right) \mathrm{e}^{-\nu|t-s|}. \tag{3.12}$$

Comparing Eq. (3.12), to Eq. (3.7) we observe that we can parametrise the telegraph model in terms of Ku, St and μ if we identify

$$\nu = \mathrm{St}, \qquad 3\mathrm{Ku}^2\mathrm{St}^2 = A_0^2 - \mu^2. \tag{3.13}$$

Closer inspection of the model [17], reveals that in order for the combined process $(j(t), z(t), \eta_t)$ to be stationary, one needs to define μ as a function of the parameters Ku and St. One possible and consistent choice is to fix μ to be the negative root[1] of the quadratic equation [17]

$$\mu^2 + \mu\mathrm{St}(\mathrm{St}+1) + 3\mathrm{Ku}^2\mathrm{St}^2 = 0. \tag{3.14}$$

Thus $\langle A(x(t),t)\rangle = \langle \eta_t\rangle = \mu < 0$ even though $\langle A(x,t)\rangle = 0$ for all x. Hence, the consistency condition (3.14) introduces preferential sampling of negative

[1] The model corresponding to the positive root turns out to be unphysical.

fluid gradients in the model [17]. The quadratic equation (3.14) has real solutions for μ as long as

$$\mathrm{Ku} \leq (\mathrm{St}+1)/\sqrt{12}\,, \tag{3.15}$$

which prescribes the regime of applicability of the model. The telegraph model has several interesting properties. Apart from being mathematically tractable, the model exhibits a region in (Ku, St) state space, where no caustics occur, because the noise η_t is bounded [17]. Further, the telegraph process turns into the Gaussian white-noise for $\mathrm{St}\to\infty$ and $\mathrm{Ku}\to 0$ if $\mathrm{Ku}^2\mathrm{St}=\varepsilon^2/3$ remains constant. In this sense, it is a generalisation of the white-noise model discussed in Section 3.2.1, with finite correlation time.

3.2.3 Persistent-flow model

The persistent-flow model is another limit of the statistical model that we have come across recently. We discuss the results for this model only briefly in this Chapter and leave details to a future publication. The model is obtained by taking $\mathrm{Ku}\to\infty$ and $\mathrm{St}\to 0$ such that $\mathrm{Ku}^2\mathrm{St}^2=\kappa^2/3$ remains constant [1]. Physically, this limit describes a situation in which the flow persists for many relaxation times of the particle dynamics [61]. The particles at each instance in time adapt to the adiabatic changes of the flow field. In this limit, the correlation function for $A(x,t)$ in Stokes coordinates turns into

$$\langle A(x,t)A(y,s)\rangle \to 3\kappa^2\left\{[(x-y)^2-3]^2-6\right\}\mathrm{e}^{-(x-y)^2/2}\,. \tag{3.16}$$

Note that the exponential time correlation is constant in this limit, $\mathrm{e}^{-\mathrm{St}|t-s|}\to 1$ and the flow field loses its time dynamics. The Gaussian statistics of $A(x,t)$ is obtained from averaging over different realisations of the flow. Because changes of the flow field are infinitely slow, there is strong preferential sampling of negative fluid velocity gradients. Obtaining realistic but non-trivial statistics for $A(x(t),t)$ in the persistent-flow model is a non-trivial task. Naively, particles in a highly persistent flow accumulate at those zeros of $u(x,t)$ at which the corresponding gradients $A(x,t)$ are negative. For Gaussian random functions, the distribution of these gradients is given by the Kac-Rice formula for random functions [64, 65, 66]. If we call $\bar{A}=\lim_{t\to\infty}A(x(t),t)$, the statistics of gradients according to the Kac-Rice formula reads [66]

$$P(\bar{A}=a)=\frac{|a|}{\kappa^2}\mathrm{e}^{-a^2/(2\kappa^2)}\theta(-a)\,. \tag{3.17}$$

Trivially, the gradient statistics in Eq. (3.17) forbids positive gradients $P(\bar{A} > 0) = 0$. The correlation function is given by

$$\lim_{t,s\to\infty} \langle\!\langle A(x(t),t)A(x(s),s)\rangle\!\rangle = \langle \bar{A}^2\rangle - \langle\bar{A}\rangle^2 = 2\kappa^2 \,. \tag{3.18}$$

A naive application of the Kac-Rice statistics does, however, not include the following dynamical effect [67]: Even if $u(x,t)$ changes its shape very slowly, zeros of $u(x,t)$ can still appear and disappear at a low but finite rate. Whenever a stable zero of $u(x,t)$ disappears, the particles that were trapped there need to travel to the next stable zero and sample non-negative flow gradients on their way [67]. Including this effect leads to a non-vanishing probability of positive gradients, $P(\bar{A} > 0) > 0$, in contradiction to the Kac-Rice statistics (3.17). This more sophisticated approach is ongoing work. As a proof of concept, we describe here the case of a Gaussian density but with mean $\langle\bar{A}\rangle$ and variance $\langle\!\langle \bar{A}^2\rangle\!\rangle$ adjusted to the Kac-Rice statistics (3.17). We believe this distribution has similar properties as the realistic density including the aforementioned dynamical effect. Our density $P(\bar{A} = a)$ thus reads

$$P(\bar{A} = a) = \frac{\mathrm{e}^{-\frac{(a-\langle\bar{A}\rangle)^2}{4\kappa^2}}}{\sqrt{4\pi\kappa^2}} \,. \tag{3.19}$$

with mean and variance

$$\langle\bar{A}\rangle = -\sqrt{\frac{\pi}{2}}\kappa \,, \qquad \langle\!\langle \bar{A}^2\rangle\!\rangle = 2\kappa^2 \,. \tag{3.20}$$

Because $\bar{A}$ is treated as a constant in the equation of motion for $z(t)$, the model is exactly solvable, independent of the chosen statistics of $\bar{A}$.

3.3 Observables

In this Section, we compute the observables defined in Section 2.2 in terms of the three models discussed above.

3.3.1 Probability distributions

In all three models, the z-coordinate has a statistical steady state distribution with a finite negative flux, given by the rate of caustic formation. For the

white-noise model, this distribution is obtained from the Fokker-Planck equation corresponding to the white-noise equation of motion (3.10). We have [1]

$$P(z(t)=z)=\frac{J}{\varepsilon^2}\mathrm{e}^{-U(z)/\varepsilon^2}\int_{-\infty}^{z}\mathrm{e}^{U(t)/\varepsilon^2}\mathrm{d}t\,, \tag{3.21}$$

with $U(x)=x^2/2+x^3/3$ and J given by

$$J^{-1}=\int_{-\infty}^{\infty}\mathrm{e}^{-U(s)/\varepsilon^2}\int_{-\infty}^{s}\mathrm{e}^{U(t)/\varepsilon^2}\mathrm{d}t\,\mathrm{d}s\,. \tag{3.22}$$

The distribution $P(z(t)=z)$ has power-law tails for $|z|\to\infty$. These are due to the events that the $z(t)$ coordinate escapes to $-\infty$. Indeed, the weight of the tails for large z is directly proportional to the rate of caustic formation J according to

$$P(z(t)=z)\sim\frac{J(\varepsilon)}{z+z^2}\,,\qquad |z|\to\infty\,. \tag{3.23}$$

The same asymptotic relation holds true for both the telegraph and the persistent-flow model, only replacing $J(\varepsilon)$ in Eq. (3.23) by $J(\mathrm{Ku},\mathrm{St})$ and $J(\kappa)$, respectively. The derivation of the densities varies, however, since the Fokker-Planck equation can be used only in the white-noise model. For the telegraph model $P(z(t)=z)$ can be obtained from the 'Formula of differentiation' [68] which was done in Ref. [17]. In the persistent-flow model the conditional distribution $P(z(t)=z|\bar{A}=a)$ is computed for constant $A(t)=\bar{A}$. Then one uses

$$P(z(t)=z)=\int_{\mathbb{R}}P(z(t)=z|\bar{A}=a)P(\bar{A}=a)\mathrm{d}a\,, \tag{3.24}$$

and Eq. (3.19) to obtain the distribution function. Figure 3.2 shows the distributions $P(z(t)=z)$ for the three different models, the white-noise model, the telegraph model and the persistent-flow model, in the left, middle and right panels, respectively. All distributions have been obtained analytically using the methods outlined above. The dashed lines show the corresponding asymptotics (3.23) which agree well with the densities at large z. The expressions for the rate of caustic formation that enter in Eq. (3.23) were obtained analytically in terms of integrals similar to Eq. (3.22), but are not shown here. Note that for the telegraph model, two different distributions are shown in the middle panel of Fig. 3.2, one for small St and large Ku (light

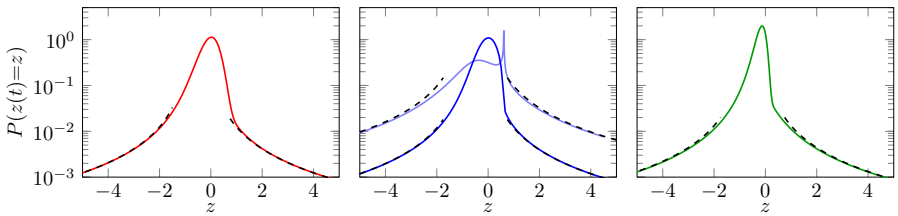

Figure 3.2: *Left:* Steady-state distribution $P(z(t) = z)$ for the white-noise model obtained from Eq. (3.21) with $\varepsilon^2 = 0.1$ (red) and the asymptotics (3.23) (black dashed). *Middle:* Distributions obtained from the telegraph model with $(\mathrm{Ku}, \mathrm{St}) = (0.5, 1.0)$ (light blue) and $(\mathrm{Ku}, \mathrm{St}) = (0.0577, 10)$ (dark blue). *Right:* Distribution obtained from the persistent-flow model with $\kappa = 0.1$.

blue) and the other one for small Ku and large St. The exact values for (Ku, St) are given in the Figure text. For large Ku and small St, the density develops an integrable singularity at the stable fixed point, which is absent in the other models [17]. The probability distributions depend surprisingly little on the choice of model. This can be understood phenomenologically by returning to the picture of the escape from the stable fixed point discussed in Section 3.1: The main ingredients that shape the z-distribution are given by the attraction towards the stable fixed point on the one hand and the escape process with subsequent return on the other hand. While the former shapes the maximum around the origin, the latter leads to the power-law tails.

3.3.2 Lyapunov exponent

A compressible underlying flow leads to strong particle clustering indicated by a negative spatial Lyapunov exponent, $\lambda < 0$. The Lyapunov exponent for the models is calculated from Eq. (3.3) using the z-distributions obtained in the previous Section. In all three models we consider in this work, the Lyapunov exponent is negative at small inertia parameter. A negative Lyapunov exponent implies that all paths in the particle dynamics eventually coalesce, which is the strongest form of clustering. For larger inertia, the Lyapunov exponent becomes positive [16]. This behaviour is known for the white-noise model [16, 48], the telegraph model [17] and can also be observed in the persistent-flow model. The left panel in Fig. 3.3 shows the Lyapunov exponents for the white-noise model (red curve) as a function of ε^2 as well as for the persistent-flow model (green curve) as a function of κ. The path-

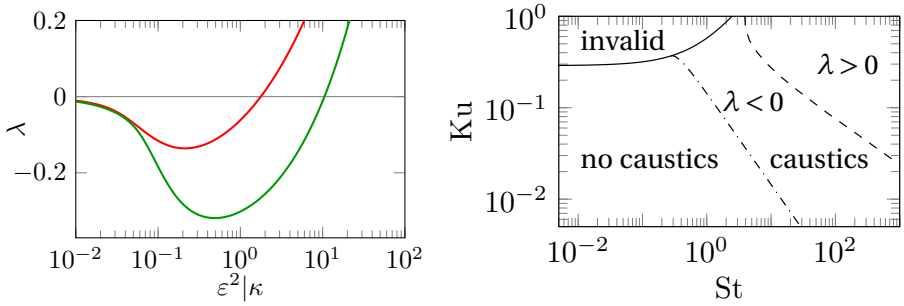

Figure 3.3: *Left:* Lyapunov exponent in the white-noise model (red) and for the persistent-flow model (green) as functions of the respective inertia parameters ε^2 and κ. *Right:* Phase diagram for the telegraph model in the (Ku, St) plane.

coalescence transition occurs at $\varepsilon \approx 1.33$ and $\kappa \approx 10.42$ for the white-noise and persistent-flow models, respectively. The right panel shows the more intricate phase diagram of the telegraph model [17] in the (Ku, St) plane. The black dashed line indicates the location of the path coalescence transition. The dash-dotted line separates the phase where caustics occur from that where caustics are absent. The solid black line defines the regime of validity according to Eq. (3.15).

3.3.3 Finite-time Lyapunov exponents

In this Section, we discuss how the statistics of the FTLE is obtained for the white-noise and the persistent-flow model. We leave out the telegraph model from the discussion, because we have not been able to obtain sufficiently accurate results for it yet. We determine the rate function $I(s)$ for the FTLE by Legendre transform of the corresponding scaled cumulant generating function $G_s(k)$ [57]. The latter is defined by

$$G_s(k) = \lim_{t\to\infty} \frac{1}{t} \log\langle e^{k\,t\,\lambda(t)}\rangle = \lim_{t\to\infty} \frac{1}{t} \log\langle j(t)^k\rangle\,. \tag{3.25}$$

The rate function $I(s)$ is given by the Legendre transform of $G_s(k)$ [69, 70]

$$I(s) = \sup_{k\in\mathbb{R}} [k\,s - G_s(k)]\,. \tag{3.26}$$

Hence, our task is to calculate the scaled cumulant generating function. For the persistent-flow model, it can obtained analytically by means of an

integral, that we do not show here. In the white-noise model, the cumulant generating function is obtained as the largest eigenvalue $\zeta^{\max}(k) = G_s(k)$ of a differential operator, the so-called tilted generator $\mathscr{L}_k$ [57, 71], which depends on the parameter k. The tilted generator for the FTLE is given by [71]

$$\mathscr{L}_k = \mathscr{L} + kz\,, \quad \text{with} \quad \mathscr{L} = \partial_z\big[z + z^2 + \varepsilon^2\partial_z\big]\,. \tag{3.27}$$

Note that for $k = 0$ the $\mathscr{L}_k$ reduces to the Fokker-Planck operator $\mathscr{L}$ corresponding to Eq. (3.10b). For small ε the largest eigenvalue $\zeta^{\max}(k)$ can be calculated from Eq. (3.27) in perturbation theory. One finds

$$G_s(k) \sim \varepsilon^2 k(k-1)\big[1 + (5-4k)\varepsilon^2 + \big(32k^2 - 86k + 60\big)\varepsilon^4 + \big(-336k^3 + 1437k^2 - 2135k + 1105\big)\varepsilon^6 + \ldots\big]\,. \tag{3.28}$$

This perturbative result becomes important in the next Section. Exact numerical expressions for $\zeta^{\max}(k)$ are calculated from Eq. (3.27) via shooting [10, 71]. Performing a Legendre transform we find the rate functions $I(s)$. The left panel of Fig. 3.4 shows the rate function $I(s)$ for the white-noise model for $\varepsilon = 0.5$, 1.5 and 10 in black, blue and red, respectively. The right panel shows $I(s)$ in the persistent-flow models for $\kappa = 0.5$ (green), 1.5 (lime) and 10 (olive). Note that the location of the minimum of $I(s)$ is given by the Lyapunov exponent. Because the Lyapunov exponents change sign at finite inertia parameter, so do the locations of the minima of the rate functions. In both models, we observe that $I(s)$ becomes broader as the inertia parameter increases. This suggests that even if the (only) Lyapunov exponent is positive, particle trajectories may approach each other for a long time, allowing for spatial clustering even at positive Lyapunov exponent [71, 72].

3.4 Correlation dimension

The correlation dimension is given by the non-trivial zero of the scaled cumulant generating function $G_s(k)$ discussed in the previous Section [12, 18, 54, 73, 74]:

$$G_s(-D_2) = 0\,, \tag{3.29}$$

A derivation of this formula based on Ref. [74] is given in Appendix A. We now use (3.29) to calculate D_2 for the two models, starting with the white-noise

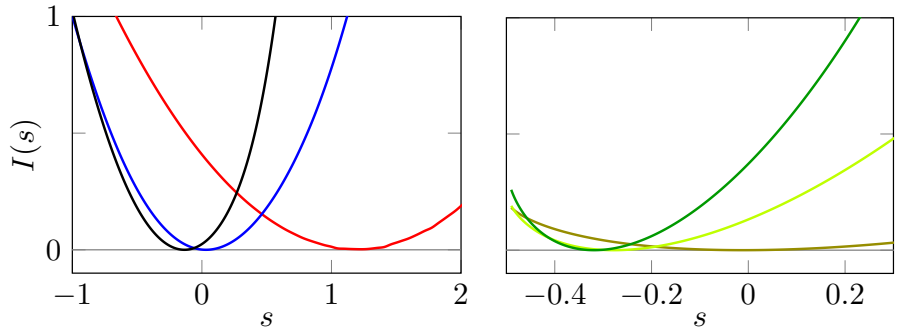

Figure 3.4: *Left:* Rate function $I(s)$ in the white-noise model for $\varepsilon = 0.5$, 1.5 and 10, black, blue and red, respectively. *Right:* Rate function $I(s)$ for persistent-flow model for $\kappa = 0.5$, 15 and 10, green, lime and olive, respectively.

model. Note that for the latter, the tilted-generator approach in combination with Eq. (3.29) is equivalent to a method of determining D_2 based on a separation ansatz for the Fokker-Planck equation, that was employed in [10, 54, 75] and paper B. Consider first the perturbative result for D_2 obtained from the perturbation expansion of $G_s(k)$ given in Eq. (3.28). The infinite series expression (3.28) is multiplied by $k(k-1)$. This means that $k^* = 1$ is a non-trivial root of $G_s(k)$ to all orders in perturbation theory. Hence, we find that the perturbation expansion of D_2 truncates after the first term [10, 54, 75]:

$$D_2 \sim -1\,. \tag{3.30}$$

How a negative correlation dimension in one dimension can be interpreted is discussed in paper B. Using the exact result for $G_s(k)$ calculated from numerically solving Eq. (3.27) we observe that Eq. (3.30) is a very poor approximation of D_2 at finite ε. The left panel in Fig. 3.5 shows D_2 obtained from Eq. (3.29) for the white-noise model as the red curve. In paper B we improved the asymptotic expansion (3.30) by an exponentially small correction

$$D_2 \sim -1 + \frac{\mathrm{e}^{-1/(6\varepsilon^2)}}{\pi}\,, \tag{3.31}$$

which is shown by the black dashed line in the left panel of Fig. 3.5. Details on the calculation are given in paper B. For larger ε, the correlation dimension increases and becomes positive for $\varepsilon > \varepsilon_c$. The same is true for the correlation

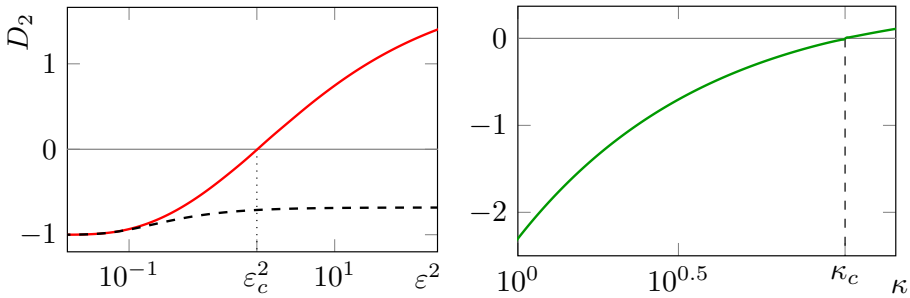

Figure 3.5: *Left:* Correlation dimension in the white-noise model shown in red, asymptotic expression (3.31) (black dashed line). *Right:* Correlation dimension for the persistent-flow model (green line).

dimension of the persistent-flow model which is given in the right panel of Fig. 3.5. The correlation dimension starts out at large negative values for small κ and becomes positive for $\kappa > \kappa_c \approx 10.4$.

3.4.1 Rate of caustic formation

We now briefly discuss explicit results for the activated form (2.25) of the rate of caustic formation at small inertial parameter. In the white-noise model, J can be obtained analytically and is given by the integral expression (3.22). For small ε the integral can be evaluated using a saddle point approximation, and one obtains [1]

$$J \sim \frac{\mathrm{e}^{-1/(6\varepsilon^2)}}{2\pi}. \tag{3.32}$$

Hence the activation function f defined in Eq. (2.25) is quadratic in Ku and linear in St, $f(\mathrm{Ku},\mathrm{St}) = 18\mathrm{Ku}^2\mathrm{St}$. In the persistent-flow model, we obtain the asymptotic form of J for small κ by analysing the tails in the distribution function $P(z(t)=z)$:

$$J \sim \frac{4\sqrt{2}}{\pi}\kappa^2 \mathrm{e}^{-\frac{1}{64\kappa^2}}, \tag{3.33}$$

which means that $f(\mathrm{Ku},\mathrm{St}) = 192\mathrm{Ku}^2\mathrm{St}^2$. For the telegraph model recall that there exists a regime in the (Ku, St) plane, where the rate of caustic formation is exactly zero, see right panel in Fig. 3.3. Around the regime border, a saddle point expansion similar to that for the white-noise model can be applied.

We find for the limit combined limit $\mathrm{St} \to \infty$ and $\mathrm{Ku} \to 0$ so that $\kappa = \sqrt{3}\mathrm{Ku}\,\mathrm{St}$ stays finite, the expression

$$J \sim \frac{1}{2\pi} \exp\left\{-2\mathrm{St}\left[\chi^- \operatorname{atan}(\chi^-) - \chi^+ \operatorname{atanh}(\chi^+)\right]\right\} \tag{3.34}$$

with $\chi^\pm = 1/\sqrt{4\kappa \pm 1}$ for $\kappa > 1/4$ and $J = 0$ otherwise. Note that the factor St can alternatively be written as $\mathrm{St} = \kappa/(\mathrm{Ku}\sqrt{3})$, which means that the expression is non-analytic in both $1/\mathrm{St}$ and Ku in the given limit. The activation function f has a non-polynomial form for the telegraph model.

3.5 Conclusions

We conclude that in one-dimensional statistical models the observables that characterise spatial clustering can be computed analytically or numerically with high accuracy. These one-dimensional results are very useful because the statistical models are similar in higher dimensions [1]. The different one-dimensional models share common features such as power-law tails in the z-distribution that scale with the respective rate of caustic formation and a path-coalescence transition [16, 48] as a function of their respective inertia parameter(s). Outside the path-coalescence phase, the one-dimensional models show clustering even though the spatial Lyapunov exponents is positive [72]. This is explained by the broad shape of the rate function for the FTLE [71].

Part II
Current and future work

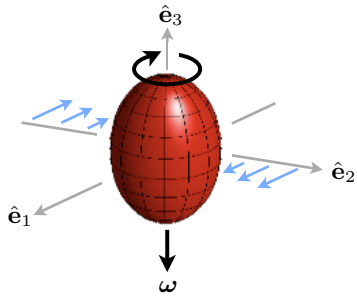

Figure 4.1: Spheroid in a shear flow in the log-rolling position. Taken from paper A.

4 Summary of research papers

In this Section we summarise the results of the three research papers A-C. In particular we explain how they are connected to the introductory text given in the previous Chapters.

4.1 Research paper A

In this paper, we calculated the angular velocity $\omega = \|\boldsymbol{\omega}\|$ of a small spheroidal particle in a simple shear flow in log-rolling position. In this position, the symmetry axis of the spheroid is oriented perpendicular to the shear plane, see Fig. 4.1, hence rendering the fluid dynamical problem steady. The characteristic Reynolds number defined in Section 1.3.1 is given by the shear Reynolds number

$$\mathrm{Re}_s = \frac{a^2 s}{\nu}, \tag{4.1}$$

where a is major semiaxis length of the particle, s is the shear rate and ν is the kinematic viscosity of the flow. When Re_s is small, the angular velocity can be expanded in a perturbation series. As noted in Section 1.4.1 the convective term $(\boldsymbol{w}\cdot\nabla)\boldsymbol{w}$ constitutes a singular perturbation to the Stokes equation (1.14). Hence, regular perturbation theory breaks down far away from the particle. We used a matched asymptotic expansion of the flow field $\boldsymbol{w}$, see

Section 1.4.1, to obtain ω to order $\mathrm{Re}_\mathrm{s}^{3/2}$:

$$\omega \sim -\frac{s}{2} + 0.0540\frac{3sD}{10\pi}\mathrm{Re}_\mathrm{s}^{3/2}, \tag{4.2}$$

where D is a parameter that depends on the particle shape. We conducted direct numerical simulations of the problem and observed excellent agreement. In the special case of a sphere, where $D = 10\pi/3$, the result differs from that obtained in Ref. [76] by a factor of roughly three. The numerical simulations, however, support our results. Furthermore, in a recent study [77] the authors considered the case of general spheroid orientation (including log-rolling) and obtained Eq. (4.2) as a special case.

4.2 Research paper B

In paper B we studied the distribution of separations and relative velocities in polydisperse turbulent suspensions of heavy particles, using the statistical model discussed in Section 1.5 and Chapter 3. Systems of particles of different Stokes numbers are common in nature which is why it is important to understand their dynamics. We studied these systems using the statistical model for of particles of *two* different Stokes numbers, St_1 and St_2. The first part of the work involved a numerical study of the two dimensional statistical model with finite Ku and St which we discussed in Section 1.3.3. For bidisperse systems, the different particle species obey two different sets of equations of motion (1.22), with St_1 and St_2, respectively. We observed that the distribution $\varrho(v_r, r)$ of relative velocities v_r between different Stokes-number particles develops a plateau at small separations r that cuts off the power-law distribution. The plateau is characterised by a cutoff scale v_c. A similar behaviour had been found for the spatial distribution in Refs. [13, 14] with the corresponding spatial cutoff scale r_c. Using a variant of the one-dimensional white-noise model discussed in Section 3.2.1, we were able to show that in one dimension, the scales v_c and r_c depend linearly upon the dimensionless quantity

$$\theta = \frac{|\mathrm{St}_1 - \mathrm{St}_2|}{\mathrm{St}_1 + \mathrm{St}_2}. \tag{4.3}$$

Interestingly, this linear dependence holds true even for the two-dimensional statistical model. The left panel in Fig. 4.2 shows how the plateau in $\varrho(v_r, r)$

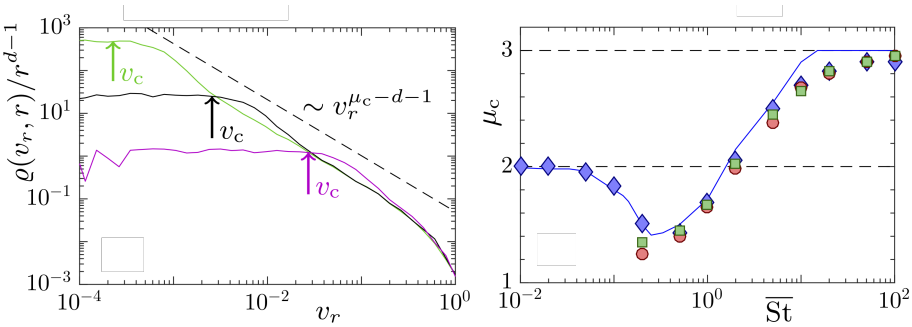

Figure 4.2: Statistical model simulations for $d = 2$, $\mathrm{Ku} = 1$ *Left:* $\varrho(v_r, r)/r^{d-1}$ evaluated for small r, $\overline{\mathrm{St}} = 1$ and $\theta = 10^{-3}$, 10^{-2} and 10^{-1} as the green, black and magenta lines, respectively. The crossover scales v_c are shown as arrows. *Right:* Power-law exponent μ_c as a function of $\overline{\mathrm{St}}$ for small θ. Exponent for the power-law tails in v_r for fixed small r with $\theta = 10^{-3}$ (green boxes) and $\theta = 10^{-2}$ (red circles). Exponent for power-law tails in r for fixed small v_r with $\theta = 10^{-2}$ (blue diamonds). Numerical data for μ_c (solid blue line). Figures taken from paper B.

at small r develops for $\theta = 10^{-3}$, 10^{-2} and 10^{-1} as the green, black and magenta lines, respectively. Further, we found that the spatial correlation dimensionμ_c[1] of the monodisperse particle system discussed in Section 2.2.1, determines the shape of the tails in the bidisperse distribution $\varrho(v_r, r)$ when replacing the Stokes number by the mean Stokes number defined as

$$\overline{\mathrm{St}} = \frac{\mathrm{St}_1 \mathrm{St}_2}{\mathrm{St}_1 + \mathrm{St}_2}. \tag{4.4}$$

This holds both for the one-dimensional white noise model and the two-dimensional statistical model. The right panel in Fig. 4.2 shows μ_c in the two-dimensional monodisperse model as a function of $\overline{\mathrm{St}}$ as the blue line. The symbols show the corresponding exponent in the tails of the bidisperse system. The tails for large r and small v_r, blue diamonds ($\theta = 10^{-3}$), and for large v_r and small r, green boxes and red circles ($\theta = 10^{-3}$ and 10^{-2}, respectively) have the same exponent just as in the monodisperse case [9].

[1]Note that here, the difference between the *spatial* correlation dimension μ_c and the *phase-space* correlation dimension D_2 is relevant. They are related by $\mu_c = \min[D_2, d]$, see Refs. [10, 53, 73].

We further found that finite θ regularises the path-coalescence transition, discussed in Secs. 2.1.4 and 3.3.2, in the one-dimensional bidisperse white-noise model. In the path-coalescence regime at small θ, the distribution of separations and relative velocities obtains power-law tails with negative correlation dimension $\mu_c < 0$. For small inertial parameter $\overline{\varepsilon} = 3\mathrm{Ku}^2\overline{\mathrm{St}}$ we were able to show that μ_c behaves asymptotically as

$$\mu_c \sim -1 + \frac{\mathrm{e}^{-1/(6\overline{\varepsilon}^2)}}{\pi}, \tag{4.5}$$

for $\overline{\varepsilon} \ll 1$. This can be written as $\mu_c \sim -1 + 2J$, where J is the rate of caustic formation in the model. This finding allows to interpret in physical terms earlier findings of negative correlation dimensions in the path-coalescence regime [9, 10, 75].

4.3 Research paper C

In this paper, we considered a one-dimensional, discrete-time model for inertial particles in fluid turbulence, the so-called correlated random walk model [72, 78]. In this model, the random displacements of an ensemble of walkers x_n are generated by a Gaussian random function $f_n(x) = u(x, t_n)$. This random function is identical to the one-dimensional random velocity field in Section 3.2, but uncorrelated in (discrete) time:

$$\langle f_n(x) f_m(y) \rangle = \alpha^2 \delta_{nm} \exp\left[-\frac{(x-y)^2}{2} \right], \tag{4.6}$$

where α is the dimensionless inertial parameter of the model. Due to the spatial correlations of the field $f_n(x)$, nearby walkers are correlated. The model shows similar behaviour as the one-dimensional continuous time white-noise model. Thus it exhibits a path-coalescence regime with associated negative correlation dimension. For small α one finds similarly to Eq. (4.5)

$$D_2 \sim -1 + 4 J_{\mathrm{CR}}, \tag{4.7}$$

where J_{CR} is the rate of trajectory crossings, which corresponds to the rate of caustic formation in continuous time. We identified a particularly simple kind of trajectory crossing in the model, which we called 'linear crossings'. Linear crossings are predominant at small separations and do not change the relative order of nearby walkers. Using an argument based on these crossings, we were able to use the scaling relation for D_q given in Eq. (2.17) to express D_q in terms of D_2:

$$D_q = \frac{D_2}{q-1}, \tag{4.8}$$

for $q > 2$.

5 Conclusions and Outlook

In this Licentiate thesis, we discussed statistical models of heavy particles in turbulence. After motivating statistical models in Chapter 1 we focussed on their one-dimensional versions in Chapter 3 and paper C. In Chapter 4 and paper B, we showed that one-dimensional models are useful in explaining the results of statistical models in higher dimensions. Thus the distribution of separations and relative velocities between the heavy particles could be explained qualitatively using a one-dimensional white-noise model. The mathematical structure of the observables, the correlation dimension D_2, the finite-time Lyapunov exponents $\lambda(t)$ and the rate of caustic formation J, are richer than one might naively expect from the apparent simplicity of the one-dimensional models. On the basis of our results, we speculated in papers B and C that the correlation dimension must be represented by a 'trans-series' [79] of the form

$$D_2 \sim \sum_{k,l,m} a_{klm} \varepsilon^k \mathrm{e}^{-l\,s(\varepsilon)} \log^m[\varepsilon]\,, \tag{5.1}$$

in order to explain its characteristic dependence on the inertial parameter ε (α in paper C).

In the future, we want to study how this structure arises in two and three dimensional systems. The correlation dimension and the Lyapunov exponents in these higher-dimensional models have characteristic minima which are not explained by perturbation theory [16, 53, 54]. It would be interesting to understand if the locations of these minima can be calculated using trans-series expansions. In order to tackle this question mathematically, we need to find out if and how matched asymptotic expansions, that take into account rare caustic events, can be used in higher dimensions. Explaining these characteristic minima would be a great success, since it is observed also in simulations [49, 80].

A related but different problem concerns the Lyapunov exponent in the one-dimensional white-noise model. The perturbation expansion for this quantity is asymptotic [37] but can be resummed using Padé-Borél resummation [81]. The result agrees very well with the known analytic formula [1]. The Padé-Borél technique fails, however, for the Lyapunov exponent in the white-noise limits in two and three dimensions. The weak-inertia expansion

for the one-dimensional telegraph model is very similar to that of the white-noise limit. It is, however, more general and contains the weak-inertia limit of the white-noise model as a special case. Our plan is therefore to develop a perturbation theory for the weak-inertia limit of the telegraph model, to resum the corresponding series using Padé-Borél resummation, and compare the result to the exact expression, which is known in form of an integral [17]. This could explain why the perturbation theory for the Lyapunov exponent does *not* fail in the one-dimensional white-noise model. An analysis of this kind is relatively simple and could give important insights into the more ambitious question discussed in the previous paragraph.

Another future project concerns the realistic modelling of the statistics of velocity gradients in the one-dimensional persistent-flow model. As discussed in Section 3.2.3, this analysis must refer to non-local effects of preferential sampling of particles. Thus the particles spend most of their time at stable zeros of the flow $u(x,t)$. These zeros vanish at a certain rate, so that the particles travel possibly long distances before ending up at the next stable zero of $u(x,t)$. In the process, they sample positive velocity gradients which affects the velocity gradient statistics experienced by the particles measurably. We plan to use the properties of Gaussian random functions to find these gradient statistics.

Finally, it could be of interest to study the distribution of time intervals between caustics t_c, mentioned in Section 2.2.3. In the weak-inertia limit, this time is known to be exponentially distributed with mean $1/J$ [63]. At finite inertia, on the other hand, the distribution is different. It could be of interest to compare the probability distribution of t_c from the one-dimensional models with that in higher dimensional statistical models, and turbulence simulations. Caustics are considered essentially one-dimensional phenomena [18, 61]. Comparing the time distributions in different dimensions would put this statement to the test. We plan to approach this question using both theory and simulations. In the white-noise model the distribution of t_c can be calculated by interpreting t_c as the first-passage time from $z(0)=\infty$ to $z(t_c)=-\infty$ and solving a Backward-Kolmogorov equation [59, 60]. In the persistent-flow model the distribution is easily obtained analytically [61].

Bibliography

[1] GUSTAVSSON, K & MEHLIG, B 2016 Statistical models for spatial patterns of heavy particles in turbulence. *Advances in Physics* **65** (1), 1–57.

[2] PUMIR, A & WILKINSON, M 2016 Collisional aggregation due to turbulence. *Annual Review of Condensed Matter Physics* **7**, 141–170.

[3] SHAW, R. A 2003 Particle-turbulence interactions in atmospheric clouds. *Annu. Rev. Fluid Mech.* **35** (1), 183—-227.

[4] BODENSCHATZ, E, MALINOWSKI, S. P, SHAW, R. A & STRATMANN, F 2010 Can we understand clouds without turbulence? *Science* **327** (5968), 970–971.

[5] DEVENISH, B. J, BARTELLO, P, BRENGUIER, J. L, COLLINS, L. R, GRABOWSKI, W. W, IJZERMANS, R. H, MALINOWSKI, S. P, REEKS, M. W, VASSILICOS, J. C, WANG, L. P & WARHAFT, Z 2012 Droplet growth in warm turbulent clouds. *Quarterly Journal of the Royal Meteorological Society* **138** (667).

[6] FALKOVICH, G, FOUXON, A & STEPANOV, G 2002 Acceleration of rain initiation by cloud turbulence. *Nature* **419**, 151–154.

[7] WILKINSON, M & MEHLIG, B 2005 Caustics in turbulent aerosols. *Europhysics Letters* **71** (2).

[8] WILKINSON, M, MEHLIG, B & BEZUGLYY, V 2006 Caustic activation of rain showers. *Physical Review Letters* **97** (4).

[9] GUSTAVSSON, K & MEHLIG, B 2011 Distribution of relative velocities in turbulent aerosols. *Physical Review E - Statistical, Nonlinear, and Soft Matter Physics* **84** (4).

[10] GUSTAVSSON, K & MEHLIG, B 2014 Relative velocities of inertial particles in turbulent aerosols. *Journal of Turbulence* **15** (1).

[11] BEC, J 2003 Fractal clustering of inertial particles in random flows. *Physics of Fluids* **15** (11).

[12] BEC, J, GAWEDZKI, K & HORVAI, P 2004 Multifractal clustering in compressible flows. *Physical Review Letters* **92** (22).

[13] BEC, J, CELANI, A, CENCINI, M & MUSACCHIO, S 2005 Clustering and collisions of heavy particles in random smooth flows. *Physics of Fluids (1994-present)* **17** (7), 073301.

[14] CHUN, J, KOCH, D. L, RANI, S. L, AHLUWALIA, A & COLLINS, L. R 2005 Clustering of aerosol particles in isotropic turbulence. *Journal of Fluid Mechanics* **536**, 219–251.

[15] FALKOVICH, G & PUMIR, A 2007 Sling Effect in Collisions of Water Droplets in Turbulent Clouds. *J. Atmos. Sci.* **64**, 4497–4505.

[16] WILKINSON, M & MEHLIG, B 2003 Path coalescence transition and its applications. *Physical Review E - Statistical Physics, Plasmas, Fluids, and Related Interdisciplinary Topics* **68** (4).

[17] FALKOVICH, G, MUSACCHIO, S, PITERBARG, L & VUCELJA, M 2007 Inertial particles driven by a telegraph noise. *Physical Review E - Statistical, Nonlinear, and Soft Matter Physics* **76** (2).

[18] BEC, J, CENCINI, M, HILLERBRAND, R & TURITSYN, K 2008 Stochastic suspensions of heavy particles. *Physica D: Nonlinear Phenomena* **237**.

[19] HAPPEL, J & BRENNER, H 1983 *Low Reynolds Number Hydrodynamics*. Kluwer Academic Publishers Group.

[20] KIM, S & KARRILA, S. J 1991 *Microhydrodynamics: principles and selected applications*. Boston: Butterworth-Heinemann.

[21] NAVIER, C. L. M. H 1823 Memoire sur les lois du mouvement des fluides. *Memoires de l'Academie Royale des Sciences de l'Instit de France* **6**, 389–440.

[22] POPE, S. B 2000 *Turbulent flows*. Cambridge, UK: Cambridge University press.

[23] FRISCH, U 1997 *Turbulence*. Cambridge, UK: Cambridge University Press.

[24] YAVUZ, M. A, KUNNEN, R. P, VAN HEIJST, G. J & CLERCX, H. J 2018 Extreme Small-Scale Clustering of Droplets in Turbulence Driven by Hydrodynamic Interactions. *Physical Review Letters* **120** (24).

[25] ELGHOBASHI, S 1994 On predicting particle-laden turbulent flows. *Applied Scientific Research* **52** (4).

[26] FALKOVICH, G, GAWEDZKI, K & VERGASSOLA, M 2001 Particles and fields in fluid turbulence. *Reviews of Modern Physics* **73** (4), 913–975.

[27] KOLMOGOROV, A. N 1941 The local structure of turbulence in incompressible viscous fluid for very large Reynolds numbers. *Doklady Akademii Nauk Sssr* **30** (4).

[28] KOLMOGOROV, A. N 1941 Dissipation of energy in locally isotropic turbulence. *Proceedings of the USSR Academy of Sciences (Russian)* **32**, 16–18.

[29] RICHARDSON, L. F 2007 *Weather prediction by numerical process, second edition*. Cambridge University Press.

[30] SAW, E. W, SHAW, R. A, AYYALASOMAYAJULA, S, CHUANG, P. Y & GYLFASON, Á 2008 Inertial clustering of particles in high-reynolds-number turbulence. *Physical Review Letters* **100** (21).

[31] CVITANOVIC, P, ARTUSO, R, MAINIERI, R, TANNER, G, VATTAY, G, WHELAN, N & WIRZBA, A 2005 Chaos: classical and quantum. *ChaosBook. org (Niels Bohr Institute, Copenhagen 2005)* **69**.

[32] SHE, Z.-S, JACKSON, E & ORSZAG, S. A 1990 Intermittent vortex structures in homogeneous isotropic turbulence. *Nature* **344** (6263).

[33] GUSTAVSSON, K 2009 Advective collisions in random flows. Licentiate thesis, University of Gothenburg.

[34] CANDELIER, F, EINARSSON, J & MEHLIG, B 2016 Angular dynamics of a small particle in turbulence. *Physical Review Letters* **117** (20).

[35] VEYSEY, J & GOLDENFELD, N 2007 Simple viscous flows: From boundary layers to the renormalization group. *Reviews of Modern Physics* **79** (3), 883–927.

[36] HINCH, E. J 1991 *Perturbation Methods*. Cambridge: Cambridge University Press.

[37] BENDER, C. M & ORSZAG, S. A 1978 *Advanced Mathematical Methods for Scientists and Engineers*. New York, USA: McGraw-Hill.

[38] MAXEY, M. R & CORRSIN, S 1986 Gravitational settling of aerosol particles in randomly oriented cellular flow fields. *J. Atm. Sci* **43**, 1112–1134.

[39] MAXEY, M. R 1987 The gravitational settling of aerosol particles in homogeneous turbulence and random flow fields. *Journal of Fluid Mechanics* **174**, 441–465.

[40] GUSTAVSSON, K, VAJEDI, S & MEHLIG, B 2014 Clustering of particles falling in a turbulent flow. *Physical Review Letters* **112** (21).

[41] BEC, J, HOMANN, H & RAY, S. S 2014 Gravity-driven enhancement of heavy particle clustering in turbulent flow. *Physical Review Letters* **112** (18).

[42] GUSTAVSSON, K, MENEGUZ, E, REEKS, M & MEHLIG, B 2012 Inertial-particle dynamics in turbulent flows: Caustics, concentration fluctuations and random uncorrelated motion. *New Journal of Physics* **14** (11).

[43] GUSTAVSSON, K & MEHLIG, B 2011 Ergodic and non-ergodic clustering of inertial particles. *EPL* **96** (6).

[44] WANG, L & MAXEY, M. R 1993 Settling velocity and concentration distribution of heavy particles in homogeneous isotropic turbulence. *J. Fluid Mech.* **256**, 27–68.

[45] BEC, J, BIFERALE, L, BOFFETTA, G, CENCINI, M, MUSACCHIO, S & TOSCHI, F 2006 Lyapunov exponents of heavy particles in turbulence. *Physics of Fluids* **18** (9).

[46] BEC, J, BIFERALE, L, CENCINI, M, LANOTTE, A, MUSACCHIO, S & TOSCHI, F 2007 Heavy particle concentration in turbulence at dissipative and inertial scales. *Physical Review Letters* **98** (8).

[47] WILKINSON, M, MEHLIG, B, ÖSTLUND, S & DUNCAN, K. P 2007 Unmixing in random flows. *Physics of Fluids* **19** (11).

[48] DEUTSCH, J. M 1985 Aggregation-disorder transition induced by fluctuating random forces. *Journal of Physics A: General Physics* **18** (9).

[49] BEC, J, BIFERALE, L, CENCINI, M, LANOTTE, A. S & TOSCHI, F 2011 Spatial and velocity statistics of inertial particles in turbulent flows. *Journal of Physics: Conference Series* **333** (1).

[50] BEC, J 2005 Multifractal concentrations of inertial particles in smooth random flows. *J. Fluid Mech.* **528**, 255–277.

[51] OTT, E 2002 *Chaos in dynamical systems, 2nd edition*. Cambridge, UK: Cambridge Univeristy Press.

[52] HARTE, D 2001 *Multifractals: theory and applications*. Chapman and Hall/CRC.

[53] WILKINSON, M, MEHLIG, B & GUSTAVSSON, K 2010 Correlation dimension of inertial particles in random flows. *EPL* **89** (5).

[54] GUSTAVSSON, K, MEHLIG, B & WILKINSON, M 2015 Analysis of the correlation dimension of inertial particles. *Phys. Fluids* **27** (7).

[55] GRASSBERGER, P & PROCACCIA, I 1983 Measuring the strangeness of Attractors. *Physica D: Nonlinear Phenomena* **9** (1-2).

[56] SCHOMERUS, H & TITOV, M 2002 Statistics of finite-time Lyapunov exponents in a random time-dependent potential. *Physical Review E* **66** (6).

[57] TOUCHETTE, H 2009 The large deviation approach to statistical mechanics. *Physics Reports* **478** (1), 1–69.

[58] GRIMMETT, G & STIRZAKER, D 2001 *Probability and Random Processes*. Oxford University Press.

[59] VAN KAMPEN, N 2007 Stochastic Processes in Physics and Chemistry. In *Stochastic Processes in Physics and Chemistry*. Elsevier.

[60] GARDINER, C. W 2009 *Handbook of Stochastic Methods: For the Natural and Social Sciences*. Springer.

[61] DEREVYANKO, S. A, FALKOVICH, G, TURITSYN, K & TURITSYN, S 2016 Lagrangian and Eulerian descriptions of inertial particles in random flows. *Journal of Turbulence* **8** (No. 16).

[62] CHETRITE, R, FALKOVICH, G & GAWEDZKI, K 2008 Fluctuation relations in simple examples of non-equilibrium steady states. *Journal of Statistical Mechanics: Theory and Experiment* **2008** (08), P08005.

[63] MEHLIG, B & WILKINSON, M 2004 Coagulation by random velocity fields as a kramers problem. *Physical Review Letters* **92** (25).

[64] RICE, S. O 1944 Mathematical analysis of random noise. *Bell System Technical Journal* **23** (3), 282–332.

[65] KAC, M 1948 On the average number of real roots of a random algebraic equation. *Proceedings of the London Mathematical Society* **2** (1), 390–408.

[66] GUSTAVSSON, K & MEHLIG, B 2013 Lyapunov Exponents for Particles Advected in Compressible Random Velocity Fields at Small and Large Kubo Numbers. *Journal of Statistical Physics* **153** (5).

[67] MEHLIG, B, WILKINSON, M, BEZUGLYY, V, GUSTAVSSON, K & NAKAMURA, K 2009 Multiple regimes of diffusion. *Phys. Rev. E* **80**.

[68] SHAPIRO, V. E & LOGINOV, V. M 1978 Formulae of differentiation and their use for solving stochastic equations. *Physica A* **91**, 563–574.

[69] GÄRTNER, J 1977 On Large Deviations from the Invariant Measure. *Theory of Probability & Its Applications* **22** (1), 24–39.

[70] ELLIS, R. S 2007 *Entropy, large deviations, and statistical mechanics*. Springer.

[71] HUBER, G, PRADAS, M, PUMIR, A & WILKINSON, M 2018 Persistent stability of a chaotic system. *Physica A: Statistical Mechanics and its Applications* **492**, 517–523.

[72] WILKINSON, M, MEHLIG, B, GUSTAVSSON, K & WERNER, E 2012 Clustering of exponentially separating trajectories. *The European Physical Journal B* **85** (1), 18.

[73] BEC, J, CENCINI, M & HILLERBRAND, R 2007 Heavy particles in incompressible flows: The large Stokes number asymptotics. *Physica D: Nonlinear Phenomena* **226** (1).

[74] PIKOVSKY, A. S 1992 Statistics of trajectory separation in noisy dynamical systems. *Physics Letters A* **165** (1), 33–36.

[75] WILKINSON, M, GUICHARDAZ, R, PRADAS, M & PUMIR, A 2015 Power-law distributions in noisy dynamical systems. *EPL* **111** (5).

[76] LIN, C.-J, PEERY, J. H & SCHOWALTER, W. R 1970 Simple shear flow round a rigid sphere: inertial effects and suspension rheology. *Journal of Fluid Mechanics* **44** (01), 1–17.

[77] MARATH, N. K & SUBRAMANIAN, G 2017 The effect of inertia on the time period of rotation of an anisotropic particle in simple shear flow. *Journal of Fluid Mechanics* **830**, 165–210.

[78] PRADAS, M, PUMIR, A, HUBER, G & WILKINSON, M 2017 Convergent chaos. *Journal of Physics A: Mathematical and Theoretical* **50** (27).

[79] DORIGONI, D 2014 An introduction to resurgence, trans-series and alien calculus. *arXiv preprint arXiv:1411.3585* .

[80] BHATNAGAR, A, GUSTAVSSON, K & MITRA, D 2018 Statistics of the relative velocity of particles in turbulent flows: Monodisperse particles. *Physical Review E* **97** (2), 23105.

[81] ELETSKY, V. L & POPOV, V. S 1978 On the Padé-Borel summation of perturbation series. *Physics Letters B* **77** (4-5).

[82] MEIBOHM, J, CANDELIER, F, ROSÉN, T, EINARSSON, J, LUNDELL, F & MEHLIG, B 2016 Angular velocity of a spheroid log rolling in a simple shear at small Reynolds number. *Physical Review Fluids* **1** (8).

[83] MEIBOHM, J, PISTONE, L, GUSTAVSSON, K & MEHLIG, B 2017 Relative velocities in bidisperse turbulent suspensions. *Physical Review E* **96** (6).

[84] DUBEY, A, MEIBOHM, J, GUSTAVSSON, K & MEHLIG, B 2018 Fractal dimensions and trajectory crossings in correlated random walks. *arXiv preprint arXiv:1806.08207* .

PART III
APPENDIX

A Correlation dimension and FTLE

We now prove the relation (3.29). The proof goes along the same lines as that given in Ref. [74] for discrete noisy dynamical systems. Consider the equations of motion for the white-noise model (3.10):

$$\dot{j}(t) = z(t)j(t), \tag{A.1a}$$

$$\dot{z}(t) = \xi_t - z(t) - z(t)^2. \tag{A.1b}$$

Transforming $j(t)$ in Eq. (A.1a) into $y(t) = \log|j(t)|$, we obtain $\dot{y}(t) = z(t)$. If we now integrate both sides of this equation from 0 to $t_n = nT$ with $T \gg 1$ we obtain

$$X_n = \int_0^{t_n} z(t)\mathrm{d}t\,, \tag{A.2}$$

where $X_n = y(t_n) - y(0) = \log|j(t_n)|$. The random variables X_n obey the recurrence

$$X_{n+1} = X_n + T\lambda_n\,, \tag{A.3}$$

with $\lambda_n = T^{-1}\int_{t_n}^{t_{n+1}} z(t)\mathrm{d}t = \lambda(nT)$. In the last step we noted that λ_n is equal to the spatial FTLE, $\lambda(nT)$, of the system. Hence, λ_n obeys a large deviation principle according to

$$P(\lambda_n = s) \approx \mathrm{e}^{-TI(s)}. \tag{A.4}$$

For long enough T, and sufficiently quickly decaying correlation function $c(|t-s|) = \langle z(t)z(s)\rangle - \langle z(t)\rangle\langle z(s)\rangle$, we can treat X_n and λ_n as independent random variables. Hence, Eq. (A.3) suggests that the probability density for X_{n+1}, $P(X_{n+1} = x)$, is given by the convolution

$$P(X_{n+1} = x) = \int_{-\infty}^{\infty} P(\lambda_n = s)P(X_n = x - Ts)\mathrm{d}s\,. \tag{A.5}$$

In the steady state, X_{n+1} and X_n are equal in distribution, which means that $P(X_{n+1}=x)=P(X_n=x)$. Substituting this condition into Eq. (A.5) we obtain an integral equation for $P(X_n=x)$ with solution $P(X_n=x)\sim \mathrm{e}^{\mu x}$, with some constant μ. Because $X_n=\log|j(t_n)|$, the density of $j(t)$ is given by the power-law

$$P(j(t)=x)\sim x^{\mu-1}\,. \tag{A.6}$$

We compare this expression to the scaling relation (2.17) and recall that $j(t)$ has the same dynamics as the particle pair separation $|x_1(t)-x_2(t)|$. Using this we conclude that $\mu=D_2$. We now substitute the expression for $P(X_n=x)$ into Eq. (A.5) and use the large deviation form (A.4). We obtain

$$\int_{-\infty}^{\infty}\mathrm{e}^{-T(I(s)+D_2 s)}\mathrm{d}s\approx 1\,, \tag{A.7}$$

which we, in turn, evaluate using Laplace's method for $T\gg 1$ [37]. We arrive at the asymptotic relation $\exp[-TG_s(-D_2)]\approx 1$, where

$$G_s(k)=\inf_{s\in\mathbb{R}}(I(s)-ks)=\sup_{s\in\mathbb{R}}(ks-I(s))\,, \tag{A.8}$$

is the scaled cumulant generating function of the FTLE. Clearly this derivation suggests that

$$G_s(-D_2)=0\,, \tag{A.9}$$

which is what we wanted to show. Note that $\mu=0$ and, thus $P(X_n=x)=\text{const}$ is another, trivial solution of Eq. (A.5). This trivial solution is independent of the underlying dynamics, and comes solely from the normalisation of $P(\lambda_n=s)$ to unity. We conclude that the non-zero root of $G_s(k)$ is the physical one.

Part IV
Research papers

Paper A

https://doi.org/10.1103/PhysRevFluids.1.084203

Angular velocity of a spheroid log rolling in a simple shear at small Reynolds number

J. Meibohm,[1] F. Candelier,[2] T. Rosén,[3] J. Einarsson,[1] F. Lundell,[3] and B. Mehlig[1]
[1]*Department of Physics, Gothenburg University, SE-41296 Gothenburg, Sweden*
[2]*University of Aix-Marseille, CNRS, IUSTI UMR 7343, 13 013 Marseille, Cedex 13, France*
[3]*KTH Mechanics, Royal Institute of Technology, SE-100 44 Stockholm, Sweden*
(Received 27 May 2016; published 22 December 2016; publisher error corrected 3 January 2017)

We analyze the angular velocity of a small neutrally buoyant spheroid log rolling in a simple shear. When the effect of fluid inertia is negligible the angular velocity $\boldsymbol{\omega}$ equals half the fluid vorticity. We compute by singular perturbation theory how weak fluid inertia reduces the angular velocity in an unbounded shear, and how this reduction depends upon the shape of the spheroid (on its aspect ratio). In addition we determine the angular velocity by direct numerical simulations. The results are in excellent agreement with the theory at small but not too small values of the shear Reynolds number Re_s, for all aspect ratios considered. For the special case of a sphere we find $\omega/s = -1/2 + 0.0540\,\mathrm{Re}_s^{3/2}$ where s is the shear rate. The $O(\mathrm{Re}_s^{3/2})$ correction differs from that derived by Lin *et al.* [J. Fluid Mech. **44**, 1 (1970)], who obtained a numerical coefficient roughly three times larger.

DOI: 10.1103/PhysRevFluids.1.084203

I. INTRODUCTION

The angular dynamics of a small, neutrally buoyant particle in a viscous fluid is determined by the local fluid-velocity gradients. In the creeping-flow limit the particle rotates in such a way that the torque exerted by the fluid vanishes at every instant in time. For larger particles this is no longer true, in general. The particle angular momentum may change as the particle rotates, and the fluid near the particle is accelerated. It is usually a difficult problem to compute the effect of particle and fluid inertia on the dynamics of particles in flows.

In this paper we calculate the leading inertial correction to the angular velocity of a neutrally buoyant spheroid that rotates in an unbounded shear so that its axis of symmetry is aligned with the flow vorticity (Fig. 1). This motion is referred to as "log rolling." For an oblate spheroid this orbit is stable, whereas it is unstable for a prolate spheroid [1]. The calculations summarized in this paper provide the corresponding angular velocity.

In the log-rolling orbit the locus of the particle surface does not change as a function of time. This simplifies the calculations considerably, because we can consider the steady problem. The latter is also easiest to analyze in direct numerical simulations because it is not necessary to change the numerical mesh as the particle moves.

In the log-rolling orbit the angular velocity aligns with the vorticity axis $\hat{\mathbf{e}}_3$ (Fig. 1), and we find

$$\omega \equiv \boldsymbol{\omega}\cdot\hat{\mathbf{e}}_3 \sim -\frac{s}{2} + 0.0540\,\frac{3sD}{10\pi}\,\mathrm{Re}_s^{3/2} \tag{1}$$

to order $O(\mathrm{Re}_s^{3/2})$. The first term on the r.h.s. corresponds to the angular velocity in the creeping-flow limit, equal to $-s/2$ for an unbounded shear with shear rate s [2]. The second term on the r.h.s describes the inertial correction for small shear Reynolds number $\mathrm{Re}_s \equiv a^2 s/\nu$, and ν is the kinematic viscosity of the fluid. Furthermore D is a shape parameter that depends on the aspect ratio of the spheroid. For a sphere we have $D = 10\pi/3$, and the general expression is given in Eq. (20) below. It turns out that $D > 0$ for all aspect ratios, so that the effect of fluid inertia reduces the magnitude of the angular velocity. But we note that there are other examples where fluid inertia increases the angular velocity of a neutrally buoyant sphere [3].

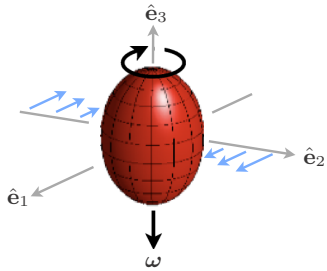

FIG. 1. Spheroid log rolling in a simple shear. The r_2 coordinate is aligned with the shear direction, and the r_3 coordinate is the negative vorticity direction. The axis of symmetry of the particle and its angular velocity $\boldsymbol{\omega} = \omega\hat{\boldsymbol{e}}_3$ are aligned with the flow vorticity.

For a spherical particle Eq. (1) reduces to $\omega/s \sim -1/2 + 0.0540\,\mathrm{Re}_s^{3/2}$. This is different from a result obtained by Lin *et al.* [4], who found a coefficient of 0.1538 for the inertial correction, instead of 0.0540. Our result is consistent with that of Stone *et al.* [5], who used a different technique. We also performed direct numerical simulations of the problem to determine the angular velocity. For a spherical particle the results are shown in Fig. 2. We see that Eq. (1) agrees well with the simulation results when Re_s is neither too large nor too small.

Why do the numerical results agree with Eq. (1) only at intermediate values of Re_s? This is a consequence of the fact that fluid inertia causes a singular perturbation of the creeping-flow

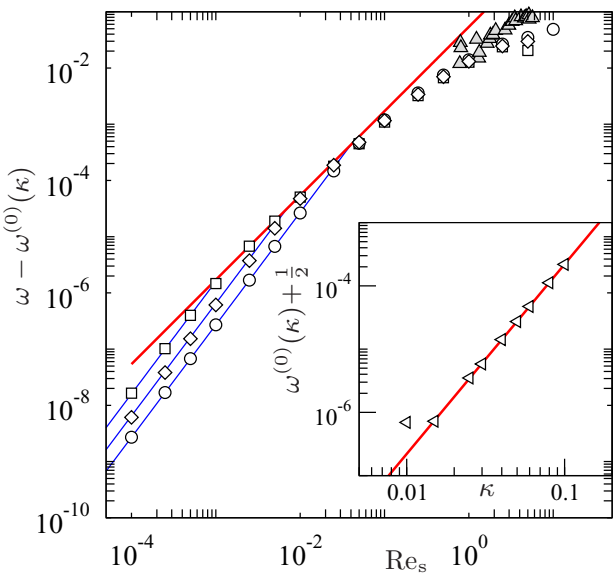

FIG. 2. $\mathrm{Re}_s^{3/2}$ correction to the angular velocity of a spherical particle. Open symbols show results of our direct numerical simulations (Sec. V) for $\kappa = 0.01$ (□), 0.025 (◇), and 0.05 (○). Here $\kappa = 2a/L$, a is the radius of the sphere, and L is the linear dimension of the simulation domain. The thick solid (red) line shows Eq. (1), valid for an unbounded shear. The thin solid (blue) lines correspond to a quadratic Re_s dependence; they show fits to Eq. (49). Also shown are experimental results by Poe and Acrivos (Sec. VI), filled triangles. The creeping-flow limit of the angular velocity in the finite, bounded system is denoted by $\omega^{(0)}(\kappa)$, and $\omega^{(0)}(\kappa) \to -\frac{1}{2}$ as $\kappa \to 0$. The inset shows $\omega^{(0)}(\kappa)+\frac{1}{2}$ as a function of κ (◁). The thick solid line (red) shows Eq. (48), with the fit parameter $C = 0.22$.

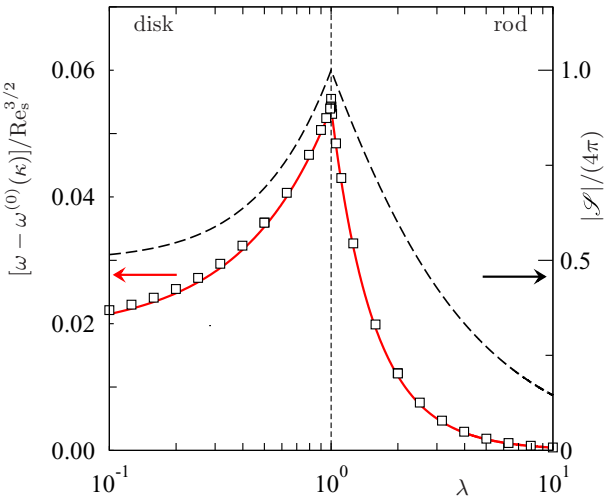

FIG. 3. $\mathrm{Re}_s^{3/2}$ correction to the angular velocity of a neutrally buoyant spheroid log rolling in a simple shear, as a function of the aspect ratio λ. Shown are results of our direct numerical simulations (Sec. V, □) for $\mathrm{Re}_s = 3 \times 10^{-3}$ and $\kappa = 0.01$. The theoretical result [Eq. (1), valid for an unbounded shear] is shown as a solid red line. The red arrow points to the corresponding axis. Also shown is the surface area $|\mathscr{S}|$ of the particle (black dashed line). The corresponding axis is on the r.h.s. (black arrow).

problem. Even at very small shear Reynolds number the perturbation is not negligible far away from the particle, at distances larger than the Saffman length $\ell_S \equiv a/\sqrt{\mathrm{Re}_s}$. This means that a regular expansion of the solution to the particle (the "inner solution") must match an approximate "outer solution" that takes into account convective fluid inertia but does not fulfill the no-slip boundary conditions on the particle surface. The power $\mathrm{Re}_s^{3/2}$ in Eq. (1) is due to the singular nature of the perturbation. The small parameter of the problem is $\epsilon \equiv \sqrt{\mathrm{Re}_s}$.

The numerical simulations shown in Fig. 2 were performed for a bounded shear, and the simulation domain is a cube with side length L (and we define $\kappa \equiv 2a/L$). We expect Eq. (1) to agree with the numerical results when $L \gg \ell_S$; in the opposite limit the perturbation is in effect regular. Figure 2 confirms this picture: the numerical results converge to Eq. (1) as L increases, but there are substantial deviations at small values of Re_s, as mentioned above. In this regime the inertial correction to the angular velocity is quadratic in Re_s (thin solid blue lines in Fig. 2). That there is no term linear in Re_s is a consequence of the symmetry of the problem. Naturally the perturbation theory must also fail at large Re_s. Equation (1) works reasonably well up to $\mathrm{Re}_s \approx 5 \times 10^{-2}$.

For a spheroidal particle the steady-state angular velocity depends on the particle shape. Figure 3 shows our results for the inertial correction of the angular velocity as a function of the particle aspect ratio at small but finite Re_s. For a prolate spheroid the aspect ratio is defined as $\lambda \equiv a/b$, where a is the major semiaxis length of the particle, and b is the minor semiaxis length. For oblate spheroids the aspect ratio is defined as $\lambda \equiv b/a$ [1]. Since the shear Reynolds number is defined in terms of the major semiaxis length of the particle, we leave a unchanged as we vary the particle shape.

In Fig. 3 the theoretical result (1) (red line) is compared to results of direct numerical simulations (white squares) of a large system ($\kappa = 0.01$) at $\mathrm{Re}_s = 3 \times 10^{-3}$. We find excellent agreement.

The asymptotic matching method described in this paper is slightly different from that used by other authors and has distinct advantages for the present problem. Therefore, we briefly comment on the differences here. We obtain the outer solution as an expansion in $\boldsymbol{k}$-space, applying the approach described in Ref. [6]. But we use a new way of generating the terms in this expansion that substantially simplifies the asymptotic matching. We obtain the angular velocity to order ϵ^3 in terms of a lower-order solution, valid to order ϵ. The method employed by Stone *et al.* [5], based

on the reciprocal theorem, has the same advantage. Our calculations show that their method yields precisely the same integral expressions as our asymptotic matching. It remains to be investigated how general this correspondence is.

II. FORMULATION OF THE PROBLEM

We consider a small neutrally buoyant spheroid rotating in a simple shear with shear rate s. We assume that the axis of symmetry of the particle is aligned with the fluid vorticity (Fig. 1) and that the center-of-mass of the particle is advected by the flow. Our aim is to determine how weak inertia affects the angular dynamics. In the log-rolling orbit, the angular velocity $\boldsymbol{\omega}$ aligns with the vorticity axis $\hat{\mathbf{e}}_3$ at all times. We compute $\omega \equiv \boldsymbol{\omega} \cdot \hat{\mathbf{e}}_3$ as an expansion in $\epsilon \equiv \sqrt{\mathrm{Re}_s}$:

$$\omega = \omega^{(0)} + \epsilon\omega^{(1)} + \epsilon^2\omega^{(2)} + \epsilon^3\omega^{(3)} + \cdots . \tag{2}$$

We calculate ω from the condition that the torque must vanish in the steady state, $\boldsymbol{\tau} = 0$. The torque is determined by the solution of the Navier-Stokes equations:

$$\epsilon^2(\partial_t u_i + u_j\partial_j u_i) = -\partial_i p + \partial_j\partial_j u_i, \;\; \partial_j u_j = 0, \tag{3}$$

written in dimensionless variables. As time scale we take the inverse shear rate s^{-1}, as length scale we take the length a of the major axis of the particle, and as velocity and pressure scales we take as and μs, respectively. Here μ is the dynamic viscosity of the fluid. The torque that the fluid exerts upon the particle is measured in units of $\mu s a^3$. All equations in the remainder of this paper are written in dimensionless variables.

In Eq. (3), u_i are the components of the fluid velocity and p is the pressure. We use the implicit summation convention that repeated indices are summed over from 1 to 3. The boundary conditions are no slip on the surface $\mathscr{S}$ of the particle, and that the fluid velocity is undisturbed infinitely far away:

$$u_i = \varepsilon_{ijk}\omega_j r_k \quad \text{for } \boldsymbol{r} \in \mathscr{S}, \quad \text{and } u_i \to u_i^{(\infty)} \text{ as } r \to \infty. \tag{4}$$

Here $u_i^{(\infty)}$ are the components of the undisturbed fluid velocity, $r = |\boldsymbol{r}|$, $\boldsymbol{r}$ is the Cartesian coordinate vector with components (r_1, r_2, r_3), and the origin of the coordinate system is located at the center of the particle. Further ε_{ijk} is the Levi-Civita symbol. For the simple shear shown in Fig. 1 we have

$$u_i^{(\infty)} = A_{ij}^{(\infty)} r_j \quad \text{with} \quad A_{ij}^{(\infty)} = \delta_{i1}\delta_{j2}. \tag{5}$$

Here $A_{ij}^{(\infty)} \equiv \partial_j u_i^{(\infty)}$ are the undisturbed fluid-velocity gradients, and δ_{ij} is the Kronecker symbol.

We decompose the fluid velocity into the undisturbed velocity $u_i^{(\infty)}$ and the disturbance velocity u_i', and decompose the pressure in a similar way:

$$u_i = u_i^{(\infty)} + u_i', \quad p = p^{(\infty)} + p'. \tag{6}$$

Since the locus of the particle surface does not change as a function of time we may consider the steady disturbance problem:

$$\epsilon^2\left(A_{jk}^{(\infty)} r_k \partial_j u_i' + A_{ij}^{(\infty)} u_j' + u_j'\partial_j u_i'\right) = -\partial_i p' + \partial_j\partial_j u_i'. \tag{7}$$

The boundary conditions for u_i' follow from Eq. (4):

$$u_i' = \varepsilon_{ijk}\omega_j r_k - u_i^{(\infty)} \quad \text{for } \boldsymbol{r} \in \mathscr{S}, \tag{8a}$$

$$u_i' \to 0 \quad \text{as } r \to \infty. \tag{8b}$$

Setting $\epsilon = 0$ in Eq. (7) corresponds to the Stokes limit. The disturbance flow in this limit, $u_i^{(0)}$, is well known. At finite values of ϵ, by contrast, Eq. (7) is difficult to solve because the inertial terms on the l.h.s. of Eq. (7) constitute a singular perturbation of the Stokes problem.

The singular nature of the perturbation is verified as follows. The leading large-r term in the Stokes solution of our problem decays as $u_i^{(0)} \sim r^{-2}$. This allows us to estimate the terms on the l.h.s. of Eq. (7) as $r \to \infty$:

$$\epsilon^2 A_{jk}^{(\infty)} r_k \partial_j u_i^{(0)} \sim \epsilon^2 A_{ij}^{(\infty)} u_j^{(0)} \sim \epsilon^2 r^{-2}, \tag{9a}$$

$$\epsilon^2 u_j^{(0)} \partial_j u_i^{(0)} \sim \epsilon^2 r^{-5}. \tag{9b}$$

The inertial terms (9a) balance the viscous term

$$\partial_j \partial_j u_i^{(0)} \sim r^{-4} \tag{10}$$

at the Saffman length ℓ_S (equal to $1/\epsilon$ in dimensionless variables). Thus even at very small shear Reynolds number the effect of convective fluid inertia cannot be neglected at distances larger than the Saffman length. We conclude that the problem is singular, perturbation theory requires matched asymptotic expansions [7,8]. In the "inner region" ($r < \ell_S$) regular perturbation theory can be used. The inner solution satisfies the boundary condition (8a) close to the particle. At $r \sim \ell_S$ the inner solution is matched to a solution obtained in the "outer region" ($r > \ell_S$) that takes into account convective fluid inertia and satisfies the boundary condition (8b).

III. METHOD

A. Inner solution

We seek regular perturbation expansions of the disturbance velocity and the pressure in the inner region:

$$u'_{\mathrm{in},i}(\boldsymbol{r}) = u^{(0)}_{\mathrm{in},i}(\boldsymbol{r}) + \epsilon\, u^{(1)}_{\mathrm{in},i}(\boldsymbol{r}) + \epsilon^2\, u^{(2)}_{\mathrm{in},i}(\boldsymbol{r}) + \cdots, \tag{11a}$$

$$p'_{\mathrm{in}}(\boldsymbol{r}) = p^{(0)}_{\mathrm{in}}(\boldsymbol{r}) + \epsilon\, p^{(1)}_{\mathrm{in}}(\boldsymbol{r}) + \epsilon^2\, p^{(2)}_{\mathrm{in}}(\boldsymbol{r}) + \cdots. \tag{11b}$$

The boundary conditions (8a) read order by order:

$$u^{(0)}_{\mathrm{in},i}(\boldsymbol{r}) = \varepsilon_{ijk}\omega_j^{(\infty)} r_k - u_i^{(\infty)} \qquad \text{for } \boldsymbol{r} \in \mathscr{S}, \tag{12a}$$

$$u^{(n)}_{\mathrm{in},i}(\boldsymbol{r}) = \varepsilon_{ijk}\omega_j^{(n)} r_k \quad \text{for } n \geqslant 1 \text{ and } \boldsymbol{r} \in \mathscr{S}. \tag{12b}$$

These boundary conditions do not suffice to determine the inner solution. Therefore each term in the expansion (11a) is matched to its counterpart in the outer solution at distance $r \sim \ell_S$ from the particle.

B. Outer solution

To determine the outer solution we solve

$$\epsilon^2\big(A_{jk}^{(\infty)} r_k \partial_j u'_{\mathrm{o},i} + A_{ij}^{(\infty)} u'_{\mathrm{o},j}\big) = -\partial_i p' + \partial_j \partial_j u'_{\mathrm{o},i} + f_i \tag{13}$$

in the outer region. The subscript "o" stands for "outer." In Eq. (13) we have neglected the nonlinear convective term $u'_j \partial_j u'_i$. At the end of this section we verify that the error is of order $O(\epsilon^4)$. The source term f_i is introduced to account for the presence of the particle: $f_i(\boldsymbol{r}) = D_{ij}\partial_j\, \delta(\boldsymbol{r})$. Here $\delta(\boldsymbol{r})$ is the three-dimensional Dirac delta function. The coefficients D_{ij} must be determined so that the outer solution matches the inner solution. We expect that the disturbance flow due to the particle can be represented in the outer region by a (symmetric) stresslet in the $\hat{\mathbf{e}}_1$-$\hat{\mathbf{e}}_2$ plane. Hence we make the *ansatz* $D_{11} = D_{22} = D_{3i} = 0$ and $D_{21} = D_{12} \equiv D$ (the "dipole strength" D is determined by matching below).

Since Eq. (13) is linear it can be solved by Fourier transform. In Sec. IV we compute the expansion of the Fourier transform $\hat{u}'_{\mathrm{o},i}(\boldsymbol{k})$ in powers of $\epsilon \equiv \sqrt{\mathrm{Re}_\mathrm{s}}$:

$$\hat{u}'_{\mathrm{o},i}(\boldsymbol{k}) = \hat{\mathcal{T}}_i^{(0)}(\boldsymbol{k}) + \epsilon\hat{\mathcal{T}}_i^{(1)}(\boldsymbol{k}) + \epsilon^2\hat{\mathcal{T}}_i^{(2)}(\boldsymbol{k}) + \epsilon^3\hat{\mathcal{T}}_i^{(3)}(\boldsymbol{k}) + \cdots . \tag{14}$$

It turns out that the odd terms in this expansion are generalized functions of $\boldsymbol{k}$ [6]. Transforming back to real space we find

$$\mathcal{T}_i^{(0)}(\boldsymbol{r}) = -\frac{15D}{20\pi}\frac{r_1 r_2 r_i}{r^5}, \tag{15a}$$

$$\mathcal{T}_i^{(1)}(\boldsymbol{r}) = 0, \tag{15b}$$

$$\mathcal{T}_i^{(2)}(\boldsymbol{r}) = -\frac{15D}{240\pi}\left\{\frac{1}{r^5}\left(r_1^2 r_2^2 r_i - r_1 r_2 r^2 \varepsilon_{ij3} r_j\right) - \frac{1}{r}\left[-r_1\delta_{i1}\left(1-\frac{r_1^2}{3r^2}\right) + \delta_{i2} r_2\left(1+\frac{r_2^2}{3r^2}\right) - \delta_{i3}\frac{r_3^3}{3r^2}\right]\right\}, \tag{15c}$$

$$\mathcal{T}_i^{(3)}(\boldsymbol{r}) = \frac{3D}{10\pi} A'_{ij} r_j . \tag{15d}$$

Details are given in Sec. IV. Equations (15) can be used to verify that the nonlinear convective term $u'_j\partial_j u'_i$ can be neglected in the outer problem (13) to order ϵ^3. The argument goes as follows. Equation (15) shows that $\mathcal{T}_i^{(n)}(\boldsymbol{r})$ scale as $\sim r^{n-2}$ for $n = 0,\ldots,3$ in the matching region. In this region, r is of order of ϵ^{-1}. Using (14) it follows that all terms in Eq. (13) are of order $O(\epsilon^4)$ in the matching region:

$$\epsilon^2\left[A_{jk}^{(\infty)} r_k \partial_j \mathcal{T}_i^{(n)} + A_{ij}^{(\infty)} \mathcal{T}_j^{(n)}\right] \sim \partial_j\partial_j \mathcal{T}_i^{(n)} \sim O(\epsilon^4) \tag{16}$$

for all $n = 0,\ldots,3$. Using the same arguments we can also estimate the magnitude of the neglected nonlinear convective term in the matching region:

$$\epsilon^2 \mathcal{T}_j^{(n)} \partial_j \mathcal{T}_i^{(n)} \sim O(\epsilon^7). \tag{17}$$

It turns out that the nonlinear convective term remains negligible for $n = 0,\ldots,3$ when $r > \ell_\mathrm{S}$. We conclude that the nonlinear convective term can be neglected in the outer problem, because it is subleading within and beyond the matching region for $n = 0,\ldots,3$. In the inner problem, in general, the nonlinear convective term cannot be neglected for $n \leqslant 3$.

C. Matching

The outer solution (15) provides boundary conditions for the inner problem in the matching region, at $r \sim 1/\epsilon$. The leading-order terms of $u'_{\mathrm{in},i}$ at large r must match Eq. (15). We now discuss the matching order by order. To leading order ϵ^0 the inner problem reads

$$-\partial_i p_\mathrm{in}^{(0)} + \partial_j\partial_j u_{\mathrm{in},i}^{(0)} = 0. \tag{18}$$

The boundary and matching conditions are given by

$$u_{\mathrm{in},i}^{(0)} = \varepsilon_{ijk}\omega_j^{(0)} r_k - u_i^{(\infty)} \quad \text{for} \quad \boldsymbol{r} \in \mathscr{S}, \tag{19a}$$

$$u_{\mathrm{in},i}^{(0)} \sim \mathcal{T}_i^{(0)} \quad \text{as } r \to \infty. \tag{19b}$$

From Eq. (19b) we see that $\mathcal{T}_i^{(0)}$ is the leading-order contribution to the Stokes problem of a spheroid freely rotating in a simple shear with its symmetry axis aligned with the $\hat{\mathbf{e}}_3$ axis. The

matching condition (19b) determines the dipole strength D introduced in the previous section. One finds D as a function of the aspect ratio λ:

$$D = \frac{16\pi(\lambda^2-1)^3}{3\lambda^3[5\lambda - 7\lambda^3 + 2\lambda^5 + 3\sqrt{\lambda^2-1}\,\mathrm{arccosh}(\lambda)]} \tag{20a}$$

for a prolate spheroid ($\lambda > 1$) and

$$D = -\frac{16\pi(1-\lambda^2)^3}{3[5\lambda - 7\lambda^3 + 2\lambda^5 - 3\sqrt{1-\lambda^2}\,\arccos(\lambda)]} \tag{20b}$$

for an oblate spheroid ($\lambda < 1$). The corresponding angular velocity is the Jeffery result $\omega^{(0)} = -\frac{1}{2}$ [2].

The order-ϵ^1 problem reads

$$-\partial_i p^{(1)}_{\mathrm{in}} + \partial_j\partial_j u^{(1)}_{\mathrm{in},i} = 0, \tag{21a}$$

$$u^{(1)}_{\mathrm{in},i} = \varepsilon_{ijk}\omega^{(1)}_j r_k \quad \text{for} \quad \boldsymbol{r} \in \mathscr{S}, \tag{21b}$$

together with the matching condition

$$u^{(1)}_{\mathrm{in},i} \sim \mathcal{T}^{(1)}_i \quad \text{as} \quad r \to \infty. \tag{21c}$$

Since $\mathcal{T}^{(1)}_i$ vanishes [see Eq. (15b)] there is no term in Eq. (14) to which the flow $u^{(1)}_{\mathrm{in},i}$ produced by the rotating particle can be matched. We conclude that $u^{(1)}_{\mathrm{in},i} \equiv 0$. It follows that the ϵ^1 contribution to the angular velocity must vanish, $\omega^{(1)} = 0$.

The second-order problem is inhomogeneous:

$$-\partial_i p^{(2)}_{\mathrm{in}} + \partial_j\partial_j u^{(2)}_{\mathrm{in},i} = A^{(\infty)}_{jk} r_k \partial_j u^{(0)}_{\mathrm{in},i} + A^{(\infty)}_{ij} u^{(0)}_{\mathrm{in},i} + u^{(0)}_{\mathrm{in},j}\partial_j u^{(0)}_{\mathrm{in},i}, \tag{22a}$$

with boundary and matching conditions:

$$u^{(2)}_{\mathrm{in},i} = \varepsilon_{ijk}\omega^{(2)}_j r_k \quad \text{for } \boldsymbol{r} \in \mathscr{S}, \tag{22b}$$

$$u^{(2)}_{\mathrm{in},i} \sim \mathcal{T}^{(2)}_i \quad \text{as} \quad r \to \infty. \tag{22c}$$

The solution is the sum of a homogeneous and a particular part: $u^{(2)}_{\mathrm{in},i} = u^{(2)}_{\mathrm{h},i} + u^{(2)}_{\mathrm{p},i}$. The particular solution is found to be $u^{(2)}_{\mathrm{p},i} = \mathcal{T}^{(2)}_i + O(1/r^2)$. The homogeneous part solves the Stokes problem

$$-\partial_i p^{(2)}_{\mathrm{h}} + \partial_j\partial_j u^{(2)}_{\mathrm{h},i} = 0 \tag{23a}$$

with boundary conditions

$$u^{(2)}_{\mathrm{h},i} = \varepsilon_{ijk}\omega^{(2)}_j r_k - u^{(2)}_{\mathrm{p},i} \quad \text{for} \quad \boldsymbol{r} \in \mathscr{S}. \tag{23b}$$

The explicit solution of the homogeneous problem shows that $u^{(2)}_{\mathrm{h},i}$ is asymptotic to $O(1/r^2)$ as $r \to \infty$. This implies that the matching condition (22c) is fulfilled by $u^{(2)}_{\mathrm{p},i}$ alone.

Direct computation confirms that the ϵ^2-contribution to the angular velocity of the particle must vanish for torque-free rotation, $\omega^{(2)} = 0$. We remark that there are, however, examples where there is a linear inertial correction to the angular velocity [9].

So far we have found that $\omega^{(0)} = -\frac{1}{2}$, and $\omega^{(1)} = \omega^{(2)} = 0$. Now consider the third order in ϵ. At this order the problem is homogeneous since $u^{(1)}_{\mathrm{in},i} \equiv 0$. The equations to solve are

$$-\partial_i p^{(3)}_{\mathrm{in}} + \partial_j\partial_j u^{(3)}_{\mathrm{in},i} = 0, \tag{24a}$$

$$u^{(3)}_{\mathrm{in},i} = \varepsilon_{ijk}\omega^{(3)}_j r_k \quad \text{for } \boldsymbol{r} \in \mathscr{S}, \tag{24b}$$

together with the matching condition

$$u^{(3)}_{\mathrm{in},i} \sim \mathcal{T}^{(3)}_i \quad \text{as } r \to \infty. \tag{24c}$$

Equation (15d) shows that $\mathcal{T}^{(3)}_i$ is a linear flow. The third-order problem (24) is thus equivalent to that of a freely rotating spheroid in the linear flow $A'_{ij} r_j$ as $\epsilon \to 0$. The solution of this problem is known, and it is discussed in the next section.

D. Angular velocity

The third-order correction to the angular velocity is computed by requiring that the third-order torque $\boldsymbol{\tau}^{(3)} \equiv \tau^{(3)} \hat{\mathbf{e}}_3$ vanishes. The third-order inner problem is equivalent to the problem of determining the torque on a freely rotating spheroid in a linear flow in the creeping-flow limit. The solution is known (see, e.g., p. 64 in Ref. [10]). In the log-rolling orbit we have

$$\tau^{(3)} = 8\pi \left[\frac{3D}{20\pi} (A'_{21} - A'_{12}) - \omega^{(3)} \right]. \tag{25}$$

Setting Eq. (25) to zero yields $\omega^{(3)}$, and thus

$$\omega \sim -\frac{1}{2} + \frac{3D}{20\pi} (A'_{21} - A'_{12}) \epsilon^3 \tag{26}$$

in dimensionless variables. In Sec. IV we show how to evaluate the constant coefficients A'_{ij}. The result is

$$A'_{12} = 0.0328, \quad A'_{21} = 0.1408. \tag{27}$$

It follows that

$$\omega \sim -\frac{1}{2} + 0.0540 \, \frac{3D}{10\pi} \, \epsilon^3. \tag{28}$$

In dimensional variables this result corresponds to Eq. (1).

IV. SOLUTION OF THE OUTER PROBLEM

In this section we determine the solution of the outer problem (13) in the limit $\epsilon \to 0$. The results are Eqs. (15).

Since Eq. (13) is linear it can be solved by Fourier transform (we employ the symmetric convention). Using incompressibility to eliminate the pressure, we find for the Fourier transform $\hat{u}'_{\mathrm{o},i}(\boldsymbol{k})$

$$\epsilon^2 \left[k_1 \frac{\partial \hat{u}'_{\mathrm{o},i}}{\partial k_2} - \left(\delta_{1i} - \frac{2k_1 k_i}{k^2} \right) \hat{u}'_{\mathrm{o},2} \right] = k^2 \hat{u}'_{\mathrm{o},i} + \frac{\mathrm{i}D}{(2\pi)^{3/2} k^2} [2k_i k_1 k_2 - k^2 (k_1 \delta_{i2} + k_2 \delta_{i1})]. \tag{29}$$

To determine the terms $\mathcal{T}^{(n)}_i$ in Eq. (14) we expand $\hat{u}'_{\mathrm{o},i}$ in ϵ. We see in the next section, however, that a regular expansion does not give all required terms. There are terms involving generalized functions that must be determined separately (Sec. IV B).

A. Even-order terms

It follows from Eq. (29) that the leading order in the ϵ expansion of $\hat{u}'_{\mathrm{o},2}$ takes the form

$$\hat{u}'_{\mathrm{o},2} = -\frac{\mathrm{i}D}{(2\pi)^{3/2}} \frac{k_1}{k^4} \left(2k_2^2 - k^2 \right) + O(\epsilon). \tag{30}$$

This determines $\hat{\mathcal{T}}_2^{(0)}(\boldsymbol{k})$:

$$\hat{\mathcal{T}}_2^{(0)}(\boldsymbol{k}) = \frac{\mathrm{i}D}{(2\pi)^{3/2}}\frac{k_1}{k^4}\left(k^2 - 2k_2^2\right). \tag{31a}$$

This is the Fourier transform of Eq. (15a). The next term in the expansion reads

$$\hat{\mathcal{T}}_2^{(2)}(\boldsymbol{k}) = -\frac{4\,\mathrm{i}D}{(2\pi)^{3/2}}\frac{k_1^2 k_2}{k^8}\left(k^2 - k_2^2\right). \tag{31b}$$

This is the Fourier transform of Eq. (15c). The next order in the expansion is

$$\hat{\mathcal{T}}_2^{(4)}(\boldsymbol{k}) = -\frac{4\,\mathrm{i}D}{(2\pi)^{3/2}}\frac{k_1^3}{k^{12}}\left(k^2 - 6k_2^2\right). \tag{31c}$$

In a similar way we expand $u'_{\mathrm{o},1}$. This yields

$$\hat{\mathcal{T}}_1^{(0)}(\boldsymbol{k}) = \frac{\mathrm{i}D}{(2\pi)^{3/2}}\frac{k_2}{k^4}\left(k^2 - 2k_1^2\right), \tag{32a}$$

$$\hat{\mathcal{T}}_1^{(2)}(\boldsymbol{k}) = \frac{4\,\mathrm{i}D}{(2\pi)^{3/2}}\frac{k_1^3 k_2^2}{k^8}, \tag{32b}$$

$$\hat{\mathcal{T}}_1^{(4)}(\boldsymbol{k}) = \frac{4\,\mathrm{i}D}{(2\pi)^{3/2}}\frac{k_1^2 k_2}{k^{12}}\left[k_1^4 + \left(2k_3^2 - 5k_2^2\right)k_1^2 + k_3^2\left(k_2^2 + k_3^2\right)\right]. \tag{32c}$$

We see that a regular expansion of Eq. (30) yields only even orders $\mathcal{T}_i^{(2n)}$. Yet odd orders $\mathcal{T}_i^{(2n-1)}$ are required to match the inner solution. Terms corresponding to odd powers in ϵ are computed in the following sections.

B. Odd-order terms

Odd terms in the expansion (14) are not captured by the expansion in ϵ described in the previous section because the odd-order terms are zero everywhere except at isolated points in $\boldsymbol{k}$-space. To compute the odd-order terms we subtract the lowest term(s) in the expansion (14) to make the next odd order leading. This new leading order is then found by taking the limit $\epsilon \to 0$. This idea was pioneered by Childress [11] and Saffman [8], and employed by Lin *et al.* [4]. These papers start from an ansatz of the outer solution written in terms of a "stretched" configuration-space variable $\tilde{\boldsymbol{r}} \equiv \epsilon \boldsymbol{r}$; see, for example, Eq. (3.12) in Ref. [8]. Here we pursue an alternative path that does not absorb the ϵ into a new variable $\tilde{\boldsymbol{r}}$ and proceeds with generalized functions in $\boldsymbol{k}$-space [6]. We define

$$\hat{u}_{\mathrm{o},i}^{(q)}(\boldsymbol{k}) \equiv \frac{1}{\epsilon^{q-1}}\left[\hat{u}'_{\mathrm{o},i}(\boldsymbol{k}) - \sum_{k=0}^{q-1}\epsilon^k \hat{\mathcal{T}}_i^{(k)}(\boldsymbol{k})\right] \sim \epsilon\,\hat{\mathcal{T}}_i^{(q)}(\boldsymbol{k}) + \epsilon^2\hat{\mathcal{T}}_i^{(q+1)}(\boldsymbol{k}) + \cdots. \tag{33}$$

To extract an odd term corresponding to $q = 2n - 1$ one can take the limit $\epsilon \to 0$ [6]:

$$\hat{\mathcal{T}}_i^{(2n-1)}(\boldsymbol{k}) = \lim_{\epsilon\to 0}\left[\epsilon^{-1}\hat{u}_{\mathrm{o},i}^{(2n-1)}(\boldsymbol{k})\right]. \tag{34a}$$

It turns out, however, that an alternative procedure has distinct advantages:

$$\hat{\mathcal{T}}_i^{(2n-1)}(\boldsymbol{k}) = \lim_{\epsilon\to 0}\frac{\mathrm{d}}{\mathrm{d}\epsilon}\left[\epsilon^{-1}\hat{u}_{\mathrm{o},i}^{(2n-2)}(\boldsymbol{k})\right]. \tag{34b}$$

Equations (34) are evaluated as follows. We derive a differential equation for $\hat{u}_{\mathrm{o},i}^{(2n-1)}(\boldsymbol{k})$ by substituting Eq. (33) into Eq. (29):

$$\epsilon^2 k_1 \frac{\partial \hat{u}_{\mathrm{o},i}^{(2n-1)}}{\partial k_2} - k^2 \hat{u}_{\mathrm{o},i}^{(2n-1)} - \epsilon^2 \left(\delta_{1i} - \frac{2k_1 k_i}{k^2}\right) \hat{u}_{\mathrm{o},2}^{(2n-1)} = -k^2 \hat{\mathcal{T}}_i^{(2n)}. \tag{35}$$

For $i = 1,2$ the solutions of Eq. (35) are

$$\hat{u}_{\mathrm{o},2}^{(2n-1)}(\boldsymbol{k}) = -\frac{1}{k^2} \int_0^\infty d\xi \, \mathrm{e}^{-\xi(k_1^2\xi^2/3 + k_1 k_2 \xi + k^2)/\epsilon^2} \left[k^4 \hat{\mathcal{T}}_2^{(2n)}(\boldsymbol{k})\right]_{k_2 = k_1\xi + k_2}, \tag{36a}$$

$$\hat{u}_{\mathrm{o},1}^{(2n-1)}(\boldsymbol{k}) = -\int_0^\infty d\zeta \, \mathrm{e}^{-\zeta(k_1^2\zeta^2/3 + k_1 k_2 \zeta + k^2)/\epsilon^2} \left[k^2 \hat{\mathcal{T}}_1^{(2n)}(\boldsymbol{k}) + \frac{k^2 - 2k_1^2}{k_1 k^2} \hat{u}_{\mathrm{o},2}^{(2n-1)}(\boldsymbol{k})\right]_{k_2 = k_1\zeta + k_2}. \tag{36b}$$

Then to determine $\hat{\mathcal{T}}_i^{(2n-1)}$ we must take the limit $\epsilon \to 0$ in Eqs. (34). To this end we use the fact that $\hat{u}_{\mathrm{o},i}^{(2n-1)}(\boldsymbol{k})$ are integrable functions of $\boldsymbol{k}$. For such a function the limit $\epsilon \to 0$ can be expressed in terms of generalized functions. We need the following three relations. First,

$$\lim_{\epsilon \to 0} \frac{1}{\epsilon^3} f(\boldsymbol{k}/\epsilon) = \mathcal{A}\, \delta(\boldsymbol{k}) \quad \text{with} \quad \mathcal{A} = \int_{\mathbb{R}^3} d^3k \, f(\boldsymbol{k}). \tag{37a}$$

Second, consider a function g that integrates to zero:

$$\int_{\mathbb{R}^3} d^3k \, g(\boldsymbol{k}) = 0. \tag{37b}$$

In this case we use

$$\lim_{\epsilon \to 0} \frac{g(\boldsymbol{k}/\epsilon)}{\epsilon^4} = \mathcal{A}_i \frac{\partial \delta(\boldsymbol{k})}{\partial k_i} \quad \text{with} \quad \mathcal{A}_i = -\int_{\mathbb{R}^3} d^3k \, k_i \, g(\boldsymbol{k}). \tag{37c}$$

Third, we make use of the identity

$$\lim_{\epsilon \to 0} \frac{\mathrm{d}}{\mathrm{d}\epsilon} \left[\frac{h(\boldsymbol{k}/\epsilon)}{\epsilon^3}\right] = \mathcal{A}_i \frac{\partial \delta(\boldsymbol{k})}{\partial k_i} \quad \text{with} \quad \mathcal{A}_i = -\int_{\mathbb{R}^3} d^3k \, k_i h(\boldsymbol{k}). \tag{37d}$$

This relation follows from Eq. (37a) for a differentiable function $h(\boldsymbol{k})$ (see the Appendix). To make use of Eqs. (37) we first derive a scaling relation for $\hat{\mathcal{T}}_i^{(2n)}$ applying the results of Sec. IV A:

$$\hat{\mathcal{T}}_i^{(2n)}(\boldsymbol{k}) = \frac{1}{\epsilon^{2n+1}} \hat{\mathcal{T}}_i^{(2n)}(\boldsymbol{k}/\epsilon). \tag{38}$$

This relation together with (36) implies

$$\hat{u}_{\mathrm{o},i}^{(2n-1)}(\boldsymbol{k}) = \frac{1}{\epsilon^{2n-1}} \hat{u}_{\mathrm{o},i}^{(2n-1)}(\boldsymbol{k}/\epsilon). \tag{39}$$

Equation (39) allows us to bring (34) into a form where Eqs. (37) can be directly applied. This yields

$$\hat{\mathcal{T}}_i^{(2n-1)}(\boldsymbol{k}) = \lim_{\epsilon \to 0} \frac{1}{\epsilon^{2n}} \hat{u}_{\mathrm{o},i}^{(2n-1)}(\boldsymbol{k}/\epsilon), \tag{40a}$$

$$\hat{\mathcal{T}}_i^{(2n-1)}(\boldsymbol{k}) = \lim_{\epsilon \to 0} \frac{\mathrm{d}}{\mathrm{d}\epsilon} \left[\frac{1}{\epsilon^{2n-1}} \hat{u}_{\mathrm{o},i}^{(2n-2)}(\boldsymbol{k}/\epsilon)\right], \tag{40b}$$

Substituting $n = 1$ into (40a) gives

$$\hat{\mathcal{T}}_i^{(1)}(\boldsymbol{k}) = \lim_{\epsilon \to 0} \frac{1}{\epsilon^2} \hat{u}_{\mathrm{o},i}^{(1)}(\boldsymbol{k}/\epsilon). \tag{41}$$

This limit evaluates to zero, and we conclude that $\mathcal{T}_i^{(1)}(\boldsymbol{r}) \equiv 0$ [Eq. (15b)]. Now consider $\hat{\mathcal{T}}_i^{(3)}(\boldsymbol{k})$. First, we use the fact that $\hat{\mathcal{T}}_i^{(1)}(\boldsymbol{k}) = 0$ together with Eq. (33) to find the relation

$$\hat{u}_{o,i}^{(2)}(\boldsymbol{k}) = \epsilon^{-1}\, \hat{u}_{o,i}^{(1)}(\boldsymbol{k}). \tag{42}$$

It follows from Eqs. (40) and (42) that

$$\hat{\mathcal{T}}_i^{(3)}(\boldsymbol{k}) = \lim_{\epsilon\to 0} \frac{1}{\epsilon^4} \hat{u}_{o,i}^{(3)}(\boldsymbol{k}/\epsilon), \tag{43a}$$

$$\hat{\mathcal{T}}_i^{(3)}(\boldsymbol{k}) = \lim_{\epsilon\to 0} \frac{\mathrm{d}}{\mathrm{d}\epsilon}\left[\frac{1}{\epsilon^3} \hat{u}_{o,i}^{(1)}(\boldsymbol{k}/\epsilon)\right], \tag{43b}$$

Finally, applying Eqs. (37c) and (37d) we find

$$\hat{\mathcal{T}}_i^{(3)}(\boldsymbol{k}) = \mathcal{A}_{ij} \frac{\partial}{\partial k_j} \delta(\boldsymbol{k}), \tag{44}$$

together with the two equivalent expressions for the normalization $\mathcal{A}_{ij}$:

$$\mathcal{A}_{ij} = -\int_{\mathbb{R}^3} d^3k\, k_j\, \hat{u}_{o,i}^{(3)}(\boldsymbol{k}), \tag{45a}$$

$$\mathcal{A}_{ij} = -\int_{\mathbb{R}^3} d^3k\, k_j\, \hat{u}_{o,i}^{(1)}(\boldsymbol{k}). \tag{45b}$$

The Fourier transform of Eq. (44) is Eq. (15d), with

$$A'_{ij} = \frac{-\mathrm{i}}{(2\pi)^{3/2}} \mathcal{A}_{ij}. \tag{46}$$

The prefactor comes from the Fourier transform (we use the symmetric convention). The integrals $\mathcal{A}_{21}$ and $\mathcal{A}_{12}$ must be evaluated numerically. It is interesting to note that Eq. (45a) agrees with Eq. (3.37) in Ref. [4] (Lin *et al.* use a different convention for the Fourier transform). This confirms that our expansion in $\boldsymbol{k}$-space yields the same result for a sphere as that obtained by Lin *et al.*, using Saffman's asymptotic matching method. We could not perform the numerical integrations of Eq. (45a) with sufficient accuracy (we estimate the relative error of our numerical integrations to be of the order of 10%). We therefore suspect that the error in the coefficient computed by Lin *et al.* occurred in the numerical integration.

On the other hand, substituting Eq. (45b) into Eq. (26), we find an expression that, for a spherical particle, is equivalent to the result obtained by by Stone *et al.* [5]. We emphasize that Eq. (45b) expresses the coefficients $\mathcal{A}_{ij}$ (and thus the angular velocity) in terms of $\hat{u}_{o,i}^{(1)}$ [Eq. (33)]. It is not necessary to compute $\hat{u}_{o,i}^{(3)}$, as suggested by Saffman [8] and Lin *et al.* [4] and carried out in Eq. (45a). This detail makes a distinct difference. The integrals in Eq. (45b) are much simpler to evaluate numerically. We find

$$\mathcal{A}_{12} = \mathrm{i}\,0.517 \quad \text{and} \quad \mathcal{A}_{21} = \mathrm{i}\,2.220, \tag{47}$$

Using Eq. (46) we obtain the coefficients quoted in Sec. III D.

V. DIRECT NUMERICAL SIMULATIONS

The numerical simulations are performed using the commercial finite-element software package Comsol Multiphysics 5.1. The simulation domain is a cube with side length L. Since $\kappa = 2a/L$, the side length is $2\kappa^{-1}$ in dimensionless variables. We impose velocity boundary conditions in the shear direction, $u_1 = \pm\kappa^{-1}$ at $r_2 = \pm\kappa^{-1}$, and periodic boundary conditions in the flow and vorticity directions at $r_{1,3} = \pm\kappa^{-1}$. On the particle surface no-slip boundary conditions are used. For given

TABLE I. Numerical values of the parameter $b(\kappa)$ in Eq. (49), obtained by fitting the results of the direct numerical simulations. For $\kappa = 0.01$ the fit used values of $\mathrm{Re_s}$ smaller than 10^{-3}. For the other values of κ the data was fitted up to $\mathrm{Re_s} = 2.5 \times 10^{-3}$.

κ	0.01	0.025	0.03	0.04	0.05	0.06	0.08	0.1
$b(\kappa)$	1.48	0.60	0.49	0.35	0.27	0.21	0.14	0.10

values of $\mathrm{Re_s}$ and κ we obtain the steady-state solution of Eq. (3), together with the corresponding angular velocity ω.

The numerical mesh consists of tetrahedral elements. The spatial resolution changes, from $\Delta r_{\min}$ close to the particle to $\Delta r_{\max}$ far from the particle. All simulations are performed using $\Delta r_{\min} = 0.06$ and $\Delta r_{\max} = 0.1\kappa^{-1}$. To assess the numerical precision we also perform simulations with $\Delta r_{\min} = 0.12$. The difference $|\omega(\Delta r_{\min} = 0.12) - \omega(\Delta r_{\min} = 0.06)|$ estimates the absolute numerical error of the angular velocity. We estimate this error to be smaller than 10^{-6} in dimensionless units.

We compute the creeping-flow limit $\omega^{(0)}$ of the angular velocity in the finite system by evaluating the angular velocity for a fluid with zero mass density. We estimate that the absolute error of the finite-size corrections is smaller than 10^{-6} in dimensionless units.

VI. DISCUSSION AND CONCLUSIONS

We computed the inertial corrections to the angular velocity of a spheroid log rolling in an unbounded simple shear to order $\epsilon^3 = \mathrm{Re_s}^{3/2}$. Our main result, Eq. (1), is shown as a function of the particle aspect ratio λ by the solid red line in Fig. 3. We observe excellent agreement with the results of our direct numerical simulations (shown as open symbols). Furthermore, we see that the inertial correction is largest for the spherical particle. This reflects the fact that the surface area $|\mathscr{S}|$ of the particle is largest when $\lambda = 1$. The surface area is also shown in Fig. 3, as a black dashed line. As $\lambda \to \infty$ the inertial correction vanishes. This is expected because the latter limit corresponds to slender rods, which do not couple back to the fluid through the boundary conditions. For extended bodies, fluid elements near the rotating particle surface are centrifuged away from the rotation axis due to fluid inertia, thereby slowing the particle down. In the slender-disk limit ($\lambda \to 0$) the inertial correction approaches a finite constant $\sim \mathrm{Re_s}^{3/2}$.

The results of the numerical simulations for a spherical particle are plotted as a function of $\mathrm{Re_s}$ in Fig. 2, for three different system sizes: $\kappa = 2a/L = 0.01$, 0.025, and 0.05. Shown is the difference between ω and the value of the angular velocity in creeping-flow limit, $\omega^{(0)}$. The inset of Fig. 2 shows $\omega^{(0)}$ as a function of κ. A fit to

$$\omega^{(0)}(\kappa) = -\tfrac{1}{2} + C\kappa^3 \tag{48}$$

gives $C \approx 0.22$. For $\mathrm{Re_s}$ between 5×10^{-4} and 5×10^{-2} the numerical data for the largest system agree well with the theoretical prediction (28). This conclusion is supported also by the numerical results reported in Ref. [12].

But at smaller values of the shear Reynolds number the numerical data lies below the theory. The reason is that $L < \ell_S$ at very small values of $\mathrm{Re_s}$. In this case the outer region does not exist, and the problem becomes a regular perturbation problem. We therefore expect that the inertial correction is quadratic in this regime:

$$\omega = \omega^{(0)}(\kappa) + b(\kappa)\mathrm{Re_s^2} \quad \text{when} \quad \mathrm{Re_s} \ll \kappa^2. \tag{49}$$

The thin solid (blue) lines in Fig. 2 show that this is indeed the case. Fitting Eq. (49) to the numerical data we find that the coefficient $b(\kappa)$ increases monotonously as κ decreases. The numerical values of $b(\kappa)$ are given in Table I.

Also shown in Fig. 2 are experimental results of Poe and Acrivos [13] for a sphere in a shear flow at shear Reynolds numbers of order unity. At these Reynolds numbers the theory (1) for $\lambda = 1$ is no

longer valid. The results of our numerical simulations are slightly below the experimental results. We do not know the reason for this discrepancy, but note that Poe and Acrivos [13] comment on the fact that a recirculation flow observed in their experiments at $\mathrm{Re_s} \approx 5$ may have caused a spurious increase of the angular velocity.

In summary, we observe good agreement between the numerical simulations and theory where expected, and we find reasonable agreement between the simulations and the experiment at $\mathrm{Re_s}$ of order unity.

The details of our matching method differ from the standard method [7,8]. We conclude by briefly summarizing the advantages of our approach. We have described two different schemes of calculating the third-order contribution to the angular velocity. The first scheme (Sec. IV B) expresses the angular velocity in terms of $\hat{u}^{(3)}_{\mathrm{o},i}(\boldsymbol{k})$ [Eq. (33)]. This approach is equivalent to the standard asymptotic matching scheme used by Lin *et al.* [4]. It results in integral expressions that we could not evaluate accurately enough.

The second scheme allows us to express the third-order contribution to the angular velocity in terms of $\hat{u}^{(1)}_{\mathrm{o},i}(\boldsymbol{k})$. This leads to integrals that are much easier to evaluate. Saffman [8] remarks that the calculation of such terms in this outer expansion is "a matter of great difficulty." Our new scheme is therefore of practical importance when performing asymptotic matching, as we avoid computing two orders in $\epsilon = \sqrt{\mathrm{Re_s}}$ altogether. Our approach shares this advantage with an alternative method that is based on the reciprocal theorem [5] and leads to identical integral expressions. This provides an interesting link between the standard asymptotic matching method and approaches based on the reciprocal theorem. But it remains to be investigated how general this correspondence is.

We expect that our scheme offers advantages in different problems too. One example is the evaluation of the viscosity and the normal stresses in a dilute suspension of spheroids. For spherical particles these were calculated in Refs. [4,5,14].

In an unbounded shear the log-rolling orbit is stable for oblate particles, but unstable for prolate particles. Direct numerical simulations [15] show that the corresponding stability exponent of the log-rolling orbit has a $\mathrm{Re_s^{3/2}}$ correction which is of the same order as the coefficients of the linear contribution. It would therefore be of interest to compute this correction from first principles. It is also important to mention that the direct numerical simulations are performed for a finite system, a bounded shear. It would be of great interest to generalize the results obtained here, but also those reported in Refs. [1,16,17], to finite systems. The first step is to compute the small-$\mathrm{Re_s^2}$ asymptotes in Fig. 2.

ACKNOWLEDGMENTS

We thank Howard Stone for discussions and for making the preprint [5] available to us. We thank Kirsten Mehlig for help with the analysis of the numerical data. J.M., J.E., and B.M. acknowledge support by Vetenskapsrådet (Grant No. 2013-3992), Formas (Grant No. 2014-585), by the grant "Bottlenecks for particle growth in turbulent aerosols" from the Knut and Alice Wallenberg Foundation, Dnr. KAW 2014.0048, and by the MPNS COST Action MP1305 "Flowing matter". T.R. and F.L. acknowledge financial support from the Wallenberg Wood Science Center, Bengt Ingeström's Foundation, and ÅForsk. The computer simulations were performed using resources provided by the Swedish National Infrastructure for Computing at the National Supercomputer Center in Sweden.

APPENDIX

In this Appendix we derive relation (37d). To this end we consider the action of $\lim_{\epsilon\to 0} \frac{d}{d\epsilon}[\epsilon^{-3} h(\boldsymbol{k}/\epsilon)]$ upon a test function ϕ:

$$\lim_{\epsilon\to 0} \left\langle \frac{d}{d\epsilon}[\epsilon^{-3} h(\boldsymbol{k}/\epsilon)], \phi \right\rangle = \lim_{\epsilon\to 0} \left\langle (-1)\epsilon^{-4} \left[3 + k_j \frac{\partial}{\partial k_j} h(\boldsymbol{k}/\epsilon) \right], \phi \right\rangle. \tag{A1}$$

This expression can written in the form of a divergence:

$$\lim_{\epsilon\to 0}\left\langle \frac{d}{d\epsilon}[\epsilon^{-3}h(\boldsymbol{k}/\epsilon)],\phi\right\rangle = \lim_{\epsilon\to 0}\left\langle (-1)\epsilon^{-4}\tfrac{\partial}{\partial k_j}[k_j h(\boldsymbol{k}/\epsilon)],\phi\right\rangle = \left\langle \lim_{\epsilon\to 0}\left[\epsilon^{-3}\left(\tfrac{k_j}{\epsilon}\right)h(\boldsymbol{k}/\epsilon)\right],\tfrac{\partial\phi}{\partial k_j}\right\rangle. \tag{A2}$$

We use Eq. (37a) to evaluate the last expression further:

$$\lim_{\epsilon\to 0}\left\langle \frac{d}{d\epsilon}[\epsilon^{-3}h(\boldsymbol{k}/\epsilon)],\phi\right\rangle = -\mathcal{A}_{ij}\left\langle \delta(\boldsymbol{k}),\frac{\partial\phi}{\partial k_j}\right\rangle = \mathcal{A}_{ij}\left\langle \frac{\partial}{\partial k_j}\delta(\boldsymbol{k}),\phi\right\rangle. \tag{A3}$$

In summary we find

$$\lim_{\epsilon\to 0}\frac{d}{d\epsilon}[\epsilon^{-3}h(\boldsymbol{k}/\epsilon)] = \mathcal{A}_{ij}\frac{\partial}{\partial k_j}\delta(\boldsymbol{k}) \tag{A4}$$

with

$$\mathcal{A}_{ij} = -\int_{\mathbb{R}^3} d^3k\, k_j\, h(\boldsymbol{k}). \tag{A5}$$

This is Eq. (37d).

[1] J. Einarsson, F. Candelier, F. Lundell, J. R. Angilella, and B. Mehlig, Rotation of a spheroid in a simple shear at small Reynolds number, Phys. Fluids **27**, 063301 (2015).

[2] G. B. Jeffery, The motion of ellipsoidal particles immersed in a viscous fluid, Proc. R. Soc. London A **102**, 161 (1922).

[3] J. J. Bluemink, D. Lohse, A. Prosperetti, and L. van Wijngaarden, A sphere in a uniformly rotating or shearing flow, J. Fluid Mech. **600**, 201 (2008).

[4] C. J. Lin, J. H. Peery, and W. R. Schowalter, Simple shear flow around a rigid sphere: inertial effects and suspension rheology, J. Fluid Mech. **44**, 1 (1970).

[5] H. A. Stone, J. F. Brady, and P. M. Lovalenti, Inertial effects on the rheology of suspensions and on the motion of individual particles (unpublished).

[6] F. Candelier, R. Mehaddi, and O. Vauquelin, Note on the method of matched-asymptotic expansions for determining the force acting on a particle, arXiv:1307.6314 (2013).

[7] I. Proudman and J. R. A. Pearson, Expansions at small Reynolds numbers for the flow past a sphere and circular cylinder, J. Fluid Mech. **2**, 237 (1957).

[8] P. G. Saffman, The lift on a small sphere in a slow shear flow, J. Fluid Mech. **22**, 385 (1965).

[9] F. Candelier, J. Einarsson, and B. Mehlig, Angular dynamics of a small particle in turbulence, Phys. Rev. Lett. **117**, 204501 (2016).

[10] S. Kim and S. J. Karrila, *Microhydrodynamics: Principles and Selected Applications*, Butterworth-Heinemann Series in Chemical Engineering (Butterworth-Heinemann, Boston, 1991).

[11] S. Childress, The slow motion of a sphere in a rotating, viscous fluid, J. Fluid Mech. **20**, 305 (1964).

[12] D. R. Mikulencak and J. F. Morris, Stationary shear flow around fixed and free bodies at finite Reynolds number, J. Fluid Mech. **520**, 215 (2004).

[13] G. G. Poe and A. Acrivos, Closed-streamline flows past rotating single cylinders and spheres: Inertia effects, J. Fluid Mech. **72**, 605 (1975).

[14] G. Subramanian, D. L. Koch, J. Zhang, and C. Yang, The influence of the inertially dominated outer region on the rheology of a dilute dispersion of low-Reynolds-number drops or rigid particles, J. Fluid Mech. **674**, 307 (2011).

[15] T. Rosén, J. Einarsson, A. Nordmark, C. K. Aidun, F. Lundell, and B. Mehlig, Numerical analysis of the angular motion of a neutrally buoyant spheroid in shear flow at small Reynolds numbers, Phys. Rev. E **92**, 063022 (2015).

[16] J. Einarsson, F. Candelier, F. Lundell, J. R. Angilella, and B. Mehlig, Effect of weak fluid inertia upon Jeffery orbits, Phys. Rev. E **91**, 041002(R) (2015).

[17] F. Candelier, J. Einarsson, F. Lundell, B. Mehlig, and J. R. Angilella, The role of inertia for the rotation of a nearly spherical particle in a general linear flow, Phys. Rev. E **91**, 053023 (2015); **92**, 059901(E) (2015).

Paper B

https://doi.org/10.1103/PhysRevE.96.061102

PHYSICAL REVIEW E **96**, 061102(R) (2017)

Relative velocities in bidisperse turbulent suspensions

J. Meibohm, L. Pistone, K. Gustavsson, and B. Mehlig
Department of Physics, Gothenburg University, SE-41296 Gothenburg, Sweden
(Received 5 March 2017; revised manuscript received 18 July 2017; published 14 December 2017)

We investigate the distribution of relative velocities between small heavy particles of different sizes in turbulence by analyzing a statistical model for bidisperse turbulent suspensions, containing particles with two different Stokes numbers. This number, St, is a measure of particle inertia which in turn depends on particle size. When the Stokes numbers are similar, the distribution exhibits power-law tails, just as in the case of equal St. The power-law exponent is a nonanalytic function of the mean Stokes number $\overline{\mathrm{St}}$, so that the exponent cannot be calculated in perturbation theory around the advective limit. When the Stokes-number difference is larger, the power law disappears, but the tails of the distribution still dominate the relative-velocity moments, if $\overline{\mathrm{St}}$ is large enough.

DOI: 10.1103/PhysRevE.96.061102

I. INTRODUCTION

The dynamics of small heavy particles in turbulence plays a crucial role in many scientific problems and technological applications. Any model of the particle dynamics must refer to the turbulence the particles experience. This is a challenge for realistic modeling of such systems, for their direct numerical simulation (DNS), and for experiments. Novel particle-tracking techniques and improved DNS algorithms have made it possible to uncover striking phenomena in turbulent aerosols. For example, heavy particles tend to avoid the vortices of the turbulent fluid, and they form small-scale fractal patterns. Nearby particles can have very high relative velocities, an effect caused by "caustic" singularities in the particle dynamics. The analysis of statistical models has led to substantial progress in explaining these phenomena, reviewed in Ref. [1]. This analysis has offered fundamental insights about how caustics shape the distribution of relative velocities of nearby particles [2–10].

These results apply only to "monodisperse" suspensions of *identical* particles. An important question is therefore how particles of *different* sizes cluster and move relative to each other. Spatial clustering of such "bidisperse" suspensions was analyzed in Refs. [11,12]. The particles cluster onto two distinct attractors, and the fractal distribution of separations between differently sized particles is cut off at a small spatial scale, r_{c}, that can be much larger than the particle size.

Here we analyze the distribution of relative velocities of particles with different sizes. Our results are important for the physics of turbulent aerosols, because the distribution of relative velocities determines the relative speeds of colliding particles, their collision rate, and collision outcomes [13–16].

In a dilute suspension of small, heavy, spherical particles the dynamics of a single particle is approximately given by Stokes law with constant $\gamma \equiv 9\rho_f \nu/(2a^2\rho_p)$:

$$\frac{d}{dt}\boldsymbol{x} = \boldsymbol{v}, \qquad \frac{d}{dt}\boldsymbol{v} = \gamma[\boldsymbol{u}(\boldsymbol{x},t) - \boldsymbol{v}]. \tag{1}$$

Here $\boldsymbol{x}$ and $\boldsymbol{v}$ are particle position and velocity, a is the particle size, ν is the fluid viscosity, and ρ_f and ρ_p are fluid and particle densities. We model the turbulent fluid velocities by a random Gaussian velocity field $\boldsymbol{u}(\boldsymbol{x},t)$ with zero mean, correlation time τ, correlation length η, and typical speed u_0, representing the universal small spatial scales of turbulence [17], neglecting intermittent, non-Gaussian features [1]. It has been shown that many important features of the dynamics of heavy particles in turbulence are explained by this model [1]. Equation (1) assumes that the particle and shear Reynolds numbers are small. Gravitational settling [18–22] is disregarded; this is valid when the turbulence is intense enough. The dimensionless parameters of the model are the Stokes number $\mathrm{St} \equiv 1/(\gamma\tau)$, a measure of particle inertia, and the Kubo number, $\mathrm{Ku} \equiv u_0\tau/\eta$, measuring the persistence of the flow.

II. RELATIVE VELOCITIES

Figure 1(a) summarizes results of statistical-model simulations in two spatial dimensions, for the distribution $\varrho(v_r,r)$ of relative radial velocity v_r and separation r between particles with slightly different Stokes numbers. Color coding and the black isolines in Fig. 1(a) are logarithmic. As a consequence, regions of equidistant isolines correspond to power laws. Figure 1(a) thus shows that the distribution exhibits a power-law tail as a function of r for small v_r and becomes uniform for small r. The crossover between the tail and the plateau defines the cut-off scale r_{c}, observed and discussed in Refs. [11,12].

Furthermore, Fig. 1(a) shows that there is a second cut-off scale, v_{c}, that distinguishes between a power law as a function of v_r for large v_r, and a plateau for small v_r. Our numerical results demonstrate that this new scale v_{c} does not depend on r [Fig. 1(a)]. This is in marked difference to the monodisperse case, where the distribution has no plateau in the limit of $r \to 0$. Panel (b) shows that v_{c} depends linearly on the parameter $\theta \equiv |\mathrm{St}_1 - \mathrm{St}_2|/(\mathrm{St}_1 + \mathrm{St}_2)$ measuring the difference between the Stokes numbers. Panel (c) shows distributions for $r \ll r_{\mathrm{c}}$ as functions of v_r, for different values of θ. The dashed line is the power law $|v_r|^{\mu_{\mathrm{c}}-d-1}$, where $d = 2$ is the

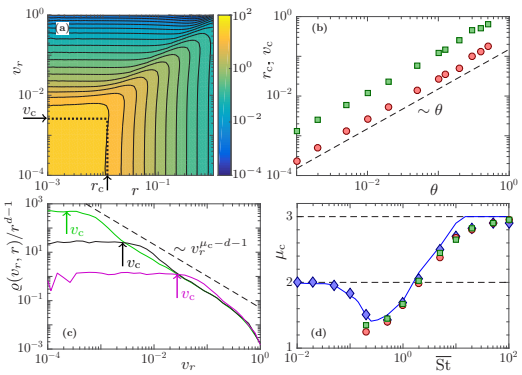

FIG. 1. Distribution $\varrho(v_r,r)$ of relative velocities between particles with different Stokes numbers. Statistical-model simulations in two dimensions ($d=2$) for $\mathrm{Ku}=1$. (a) Contour plot of $\varrho(v_r,r)/r^{d-1}$ for $\overline{\mathrm{St}}=1$ and $\theta=10^{-2}$ (see text). Dotted lines show cut-off scales r_c and v_c. (b) Dependence of r_c on θ (green □), and of v_c on θ (red ○), for $\overline{\mathrm{St}}=1$. (c) $\varrho(v_r,r)/r^{d-1}$ evaluated at $r<r_c$, for $\overline{\mathrm{St}}=1$ and $\theta=10^{-3}$ (green line), $\theta=10^{-2}$ (solid black line), and $\theta=0.1$ (magenta line). Crossover scales v_c (arrows). (d) Power-law exponent μ_c versus $\overline{\mathrm{St}}$ for small θ. Exponent for power-law tails in v_r for fixed r with $\theta=10^{-3}$ (green □) and $\theta=10^{-2}$ (red ○). Exponent for power-law tails in r for fixed v_r with $\theta=10^{-2}$ (blue ◇). Numerical data for $\min(D_2,d+1)$ where D_2 is the phase-space correlation dimension (solid blue line).

spatial dimension. Panel (d) demonstrates that the exponent μ_c is approximately equal to $\min(D_2,d+1)$ where $D_2(\overline{\mathrm{St}})$ is the phase-space correlation dimension of a suspension of identical particles with Stokes number $\overline{\mathrm{St}}\equiv(\overline{\gamma}\tau)^{-1}$ and $\overline{\gamma}=\frac{1}{2}(\gamma_1+\gamma_2)$.

The shape of the distribution shown in Fig. 1(c) has a strong effect on the moments of v_r. For bidisperse suspensions, the plateau of $\varrho(v_r,r)$ ($r<r_c$ and $|v_r|<v_c$) yields an r^{d-1} contribution to the moments $\langle|v_r|^p\rangle$, just as the caustic contribution for identical particles [23]. For $\overline{\mathrm{St}}\ll 1$, when caustics are rare, the dominant contribution to the moments of v_r at small r comes from the plateau of the distribution. But for $\overline{\mathrm{St}}\sim 1$, caustics are abundant and for $p\gtrsim 1$ the moments $\langle|v_r|^p\rangle$ are dominated by the tails of the distribution.

The plateau of the bidisperse distribution below r_c and v_c affects the tails indirectly. Comparing the normalized mono- and bidisperse distributions we see that the tails for $\theta\neq 0$ must lie above those for $\theta=0$. This means that the moments $\langle|v_r|^p\rangle$ must have a minimum for $\theta=0$ (at fixed $\overline{\mathrm{St}}$ and fixed small separation). This is consistent with the findings of Refs. [24–28].

III. ANALYSIS OF THE WHITE-NOISE LIMIT

We now show that all of the above observations can be explained qualitatively by analyzing a one-dimensional white-noise model for the dynamics of a pair of particles. A particle pair in one dimension is described by the four coordinates (x_1,v_1) and (x_2,v_2). It is convenient to transform to the relative coordinates $\Delta x=x_2-x_1$, $\Delta v=v_2-v_1$, $\bar{x}=\frac{1}{2}(x_1+x_2)$, and $\bar{v}=\frac{1}{2}(v_1+v_2)$. At small spatial separations, we can linearize the flow field: $u(x_2,t)-u(x_1,t)\sim A(t)\Delta x$. The spatial dependence in $A(x,t)\equiv\partial_x u(x,t)$ is neglected here. This disregards preferential sampling which is absent in the white-noise limit [1]. The gradient $A(t)$ has zero mean and correlation function $\langle A(t_1)A(t_2)\rangle=3(u_0/\eta)^2\exp(-|t_2-t_1|/\tau)$. For $\theta\neq 0$ there is an additional stochastic driving, $u(x_1,t)+u(x_2,t)\sim 2u(\overline{x},t)$. Neglecting the spatial dependence we write $B(t)\equiv 2u(\overline{x},t)$. The two noise terms $A(t)$ and $B(t)$ are uncorrelated, and $\langle B(t_1)B(t_2)\rangle=4u_0^2\exp(-|t_2-t_1|/\tau)$. We use the de-dimensionalization $\tilde{t}\equiv t\overline{\gamma}$, $\tilde{x}\equiv x/\eta$, $\tilde{v}\equiv v/(\eta\overline{\gamma})$, $\tilde{u}\equiv u/(\eta\overline{\gamma})$. Dropping the tildes we find

$$\frac{d}{dt}\Delta x=\Delta v \quad\text{and}\quad \frac{d}{dt}\begin{bmatrix}\Delta v\\ 2\overline{v}\end{bmatrix}=\begin{bmatrix}1 & \theta\\ \theta & 1\end{bmatrix}\begin{bmatrix}A(t)\Delta x-\Delta v\\ B(t)-2\overline{v}\end{bmatrix}. \quad (2)$$

Note that the equation for $\bar{x}$ decouples and is not considered here. The white-noise limit is taken by letting $\overline{\mathrm{St}}\to\infty$ and $\mathrm{Ku}\to 0$ such that $\overline{\varepsilon}^2\equiv 3\mathrm{Ku}^2\,\overline{\mathrm{St}}$ stays finite. In this limit we obtain $\langle A(t_1)A(t_2)\rangle=\frac{3}{4}\langle B(t_1)B(t_2)\rangle=2\overline{\varepsilon}^2\delta(t_2-t_1)$. The white-noise parameter $\overline{\varepsilon}$ is a measure for the degree of inertia in the problem (2) and plays a similar role as $\overline{\mathrm{St}}$ [1] in the two-dimensional system described above. We are thus left with three coupled dynamical variables, Δx and Δv as in the monodisperse case, and the mean velocity $\overline{v}$. We write $\varrho(\Delta v,\Delta x)\equiv\int d\overline{v}\,P(\Delta v,\Delta x,\overline{v})$, where $P(\Delta v,\Delta x,\overline{v})$ is the steady-state distribution of Δv, Δx, and $\overline{v}$.

A. Crossover scales

In the equation for Δv, Eq. (2), we identify three competing terms: the two noise terms $V_1\equiv A\Delta x$ and $V_2\equiv\theta(B-2\overline{v})$, and the damping term $-\Delta v$:

$$\frac{d}{dt}\Delta v=\underbrace{-\Delta v}_{\text{damping}}+\underbrace{A(t)\Delta x}_{V_1}+\underbrace{\theta(B(t)-2\overline{v})}_{V_2}. \quad (3)$$

The multiplicative-noise term V_1 together with the damping term leads to the power-law tails of the relative-velocity distribution in monodisperse suspensions [7]. The additive-noise term V_2 is proportional to θ and contains the Gaussian white noise $B(t)$, responsible for diffusive behavior at small scales.

Consider first how to estimate r_c. Since the relative strength of V_1 and V_2 depends on Δx, we expect that r_c corresponds to the value of Δx for which V_1 and V_2 are of comparable intensity. We define the noise intensity Φ_X as $\Phi_X\equiv\int_{-1}^{1}dt\,\langle X(t)X(0)\rangle$. Demanding $\Phi_{V_1}\sim\Phi_{V_2}$ yields the estimate

$$r_c\sim\sqrt{\frac{\Phi_{V_2}}{\Phi_A}}\propto\theta. \quad (4)$$

This linear dependence upon θ is consistent with the conclusions of Refs. [11,12], and it is confirmed by the two-dimensional numerical data in Fig. 1(b) (green □). It must be emphasized, however, that the estimate is not precise enough to explain a weak $\overline{\varepsilon}$ dependence that we observe in our numerical simulations of the one-dimensional model (not shown).

Let us now find an estimate for the new crossover scale v_c. To this end we consider small separations and small relative velocities, so that $\Phi_{V_1}\ll\Phi_{V_2}$. This allows us to neglect the term $A(t)\Delta x$ in Eq. (2). The resulting closed set of equations for

$\boldsymbol{v} \equiv [\Delta v, 2\bar{v}]$ gives rise to a Gaussian steady-state distribution

$$\lim_{\Delta v,\Delta x\to 0} P(\Delta v,\Delta x,\bar{v}) \propto \mathrm{e}^{-(1/2)\boldsymbol{v}^T\mathbb{M}\boldsymbol{v}}, \tag{5a}$$

$$\mathbb{M} = \frac{3}{2\bar{\varepsilon}^2(1-\theta^2)}\begin{bmatrix} \frac{2-\theta^2}{\theta^2} & -\frac{1}{\theta} \\ -\frac{1}{\theta} & 1 \end{bmatrix}. \tag{5b}$$

From Eqs. (5) we derive the marginal distribution of Δv and estimate v_c^2 by its variance. This leads to a linear dependence of v_c on both $\bar{\varepsilon}$ and θ:

$$v_c \propto \bar{\varepsilon}\theta. \tag{6}$$

In Fig. 1(b) (red ○), we observe excellent agreement of the two-dimensional numerical data with the linear θ dependence predicted by Eq. (6). The linear dependence on $\bar{\varepsilon}$ was also confirmed in statistical-model simulations but is not shown.

Finally, consider the case where $\Phi_{V_1} \gg \Phi_{V_2}$, that is, either $|\Delta x| \gg r_c$ or $|\Delta v| \gg v_c$. In this limit the dynamics is essentially that of monodisperse suspensions, but with mean Stokes number $\overline{\mathrm{St}}$. For $|\Delta x| \gg r_c$ or $|\Delta v| \gg v_c$ the distribution is therefore expected to show the same power-law tails as the monodisperse case [Fig. 1(c)], with exponent μ_c that depends on $\overline{\mathrm{St}}$.

B. Power-law tails

It follows from the analysis above that the relative dynamics is diffusive for $|\Delta x| \ll r_c$ and $|\Delta v| \ll v_c$. In this case $P(\Delta v,\Delta x,\bar{v})$ is given by the Gaussian distribution (5). In the tails, i.e., for $|\Delta x| \gg r_c$ or $|\Delta v| \gg v_c$, by contrast, the dynamics is that of the monodisperse suspension and we can decompose the joint distribution according to $P(\Delta v,\Delta x,\bar{v}) = \varrho_0(\Delta v,\Delta x)p(\bar{v}) + \delta P(\Delta v,\Delta x,\bar{v})$. Here, $\varrho_0(\Delta v,\Delta x)$ equals the distribution for monodisperse particles ($\theta = 0$) and $\delta P(\Delta x,\Delta v,\bar{v})$ is negligible sufficiently far out in the tails. In order to find $\varrho_0(\Delta x,z)$ we follow Ref. [7] and make the separation ansatz $\varrho_0(\Delta x,z) = \sum_\mu a_\mu g_\mu(\Delta x)Z_\mu(z)$ with $z \equiv \Delta v/\Delta x$ and expansion coefficients a_μ. Inserting this ansatz into the Fokker-Planck equation corresponding to Eq. (2) we obtain

$$g_\mu(\Delta x) = |\Delta x|^{\mu-1} \quad \text{and} \quad \frac{d}{dz}\left(z + z^2 + \bar{\varepsilon}^2\frac{d}{dz}\right)Z_\mu = \mu z Z_\mu. \tag{7}$$

This is the equation for a suspension of identical particles [7] with Stokes number $\overline{\mathrm{St}}$. In a slightly different form, Eq. (7) was used to model the effect of wall collisions in turbulent suspensions [29].

Particle-exchange symmetry [7] requires that $Z_\mu(z)$ is symmetric for large $|z|$, $\lim_{z\to\infty} Z_\mu(z)/Z_\mu(-z) = 1$. Numerical analysis shows that Eq. (7) exhibits a discrete set of such solutions [15]. For small $\bar{\varepsilon}$ only two values are allowed: $\mu = 0$ and $\mu = \mu_c(\bar{\varepsilon})$.

In the monodisperse case, $\mu_c(\bar{\varepsilon})$ equals D_2 for $\bar{\varepsilon} > \bar{\varepsilon}_c$. For $\bar{\varepsilon} < \bar{\varepsilon}_c$, by contrast, particle paths coalesce exponentially [30], there is no power-law steady state, and $\mu_c(\bar{\varepsilon})$ becomes negative and loses its meaning as correlation dimension. As a consequence the distribution $g_{\mu_c}(\Delta x) = |\Delta x|^{\mu_c-1}$ is not normalizable for $\mu_c \leqslant 0$.

In the bidisperse case, this divergence is regularized since diffusion dominates for $|\Delta x| \ll r_c$ and $|\Delta v| \ll v_c$. Thus a power-law steady-state distribution is obtained, even for $\bar{\varepsilon} < \bar{\varepsilon}_c$. This is analogous to the effect of small-scale diffusion that regularizes the power-law steady-state distribution of separations [31].

The full solution of (7) consists of a sum of two terms, $a_0|\Delta x|^{-1}Z_0(z) + a_{\mu_c}|\Delta x|^{\mu_c-1}Z_{\mu_c}(z)$. As was discussed in [7], the separation ansatz for $\varrho(\Delta x,z)$ is strictly valid only for $|\Delta x| \ll 1$. The term that contains a_0 is therefore subdominant for $\mu_c < 0$. For $\mu_c > 0$ we expect $a_0 \sim \theta \ll a_{\mu_c}$ since a_0 must vanish in order for the distribution to be normalizable over $\Delta x = 0$ as $\theta \to 0$, consistent with the numerical small-θ results in Fig. 2(a). Therefore we disregard the $\mu = 0$ term for all values of $\bar{\varepsilon}$.

Figure 2(b) shows that for $\theta \ll 1$ the exponents of both the Δx and Δv distributions (symbols) equal the numerically calculated $\mu_c(\bar{\varepsilon})$ (solid blue line). The asymptote $Z_{\mu_c}(z) \sim |z|^{\mu_c-2}$ for large $|z|$ gives rise to the power-law tails in the relative-velocity distribution of the form $|\Delta v|^{\mu_c-2}$. In d spatial dimensions a similar argument yields tails of the form $v_r^{\mu_c-d-1}$. This explains the power laws observed in Figs. 1(c) and 2(a).

In summary, the white-noise analysis qualitatively explains not only the existence of the plateau in the relative-velocity distribution and the corresponding crossover scales r_c and v_c, it also yields the linear dependence of these scales upon θ, and explains the power-law tails. Thus, the one-dimensional white-noise analysis qualitatively explains all the important features in Fig. 1.

C. Failure of perturbation theory in $\bar{\varepsilon}$

Figure 2(b) demonstrates that the exponent μ_c depends very sensitively on $\bar{\varepsilon}$, for small $\bar{\varepsilon}$. Here we show that this dependence is nonanalytic. This means that it cannot be obtained by perturbation theory in $\bar{\varepsilon}$, and this in turn is a likely reason [32] why Borel resummation of perturbation theory does not yield accurate results for the correlation dimension D_2 (Fig. 1 in Ref. [33]). There is, to date, no theory explaining these observations.

The exponent μ_c appears as a generalized eigenvalue in Eq. (7), but exact solutions to Eq. (7) are known only for $\mu = 0$ [30], $\mu = -1$ [34], and in the large $\bar{\varepsilon}$ limit [35]. The physical solution at small $\bar{\varepsilon}$ corresponds to the eigenvalue $\mu_c(\bar{\varepsilon})$. The solution for $\mu = -1$ is unphysical since it does not obey particle-exchange symmetry.

Numerical analysis reveals that $\mu_c(\bar{\varepsilon}) \to -1$ as $\bar{\varepsilon} \to 0$. We write $\mu_c = -1+\delta\mu$, where $\delta\mu \geqslant 0$ is an "eigenvalue splitting" that vanishes as $\bar{\varepsilon} \to 0$, and attempt to find the physical solution by perturbation theory in $\delta\mu$:

$$Z_{\mu_c}(z) = Z^{(0)}(z) + \delta\mu\, Z^{(1)}(z) + \delta\mu^2 Z^{(2)}(z) + \ldots. \tag{8}$$

Substituting (8) into (7) we obtain a hierarchy of differential equations for $Z^{(n)}$ given by

$$\frac{d}{dz}\left[z + z^2 + \bar{\varepsilon}^2\frac{d}{dz}\right]Z_\mu^{(0)} + zZ_\mu^{(0)} = 0, \tag{9a}$$

$$\frac{d}{dz}\left[z + z^2 + \bar{\varepsilon}^2\frac{d}{dz}\right]Z_\mu^{(n)} + zZ_\mu^{(n)} = zZ_\mu^{(n-1)}, \quad n \geqslant 1. \tag{9b}$$

Equation (9a) is solved by the unphysical solution discussed above, i.e., $Z^{(0)} = Z_{-1}$. The general form of the latter is known [34]:

$$Z_{-1} = C_1(z+1)e^{-U(z)} + C_2(z+1)\int_{-\infty}^{z} \mathrm{d}t\, \frac{e^{U(t)-U(z)}}{(t+1)^2}. \tag{10}$$

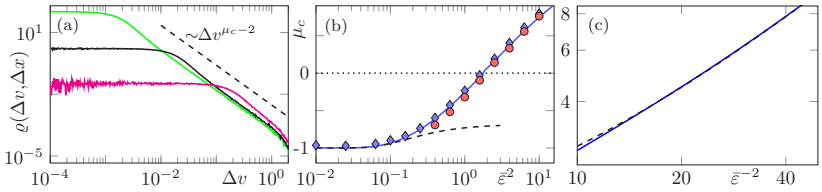

FIG. 2. (a) Distribution of Δv at small Δx from white-noise simulations of Eq. (2), for $\bar{\varepsilon}^2 = 2$ and $\theta = 10^{-3}$, $\theta = 10^{-2}$, and $\theta = 10^{-1}$; green, black, and pink curves, respectively. (b) Exponent μ_c as a function of $\bar{\varepsilon}$ from simulations of Eq. (2) for $\theta = 0.01$, obtained from fit to Δx tails (blue $\Diamond$), and from fit to Δv tails (red $\circ$). Result for equal St obtained by numerical solution of Eq. (7) (solid blue line) and the analytical prediction, Eq. (12) (dashed black line). (c) Same data as for the solid and dashed lines in panel (b), but plotted here as $-\log(1+\mu_c)$ versus $\bar{\varepsilon}^{-2}$.

Here $U(z) \equiv (\frac{1}{3}z^3 + \frac{1}{2}z^2)/\bar{\varepsilon}^2$, and C_1 and C_2 are constants. The first-order solution reads

$$Z^{(1)} = \frac{z+1}{\bar{\varepsilon}^2}\int_{-\infty}^{z} dt\,\frac{e^{U(t)-U(z)}}{(t+1)^2}\int_{-1}^{t} dt' t'(t'+1)Z_{-1}(t'). \quad (11)$$

The integrand involves Z_{-1}, and we must take $C_1 = 0$ in Eq. (10) for Z_{-1} since the first term in (10) is not normalizable. We further choose $C_2 = -\bar{\varepsilon}^2$ because it normalizes the large-z tails of Z_{-1} to $Z_{-1} \sim -z^{-3}$. To evaluate (11) we use the fact that $\delta\mu \to 0$ as $\bar{\varepsilon} \to 0$ and apply a WKB approximation [36] of Z_{-1} that becomes exact in the limit $\bar{\varepsilon} \to 0$. The equation for Z_{-1} has two "turning points" at $z = -1,0$ where the WKB approximation breaks down. We find locally exact solutions and use these to match the WKB solutions across the turning points. Details of this asymptotic-matching method are given in the Supplemental Material [37]. In this way we find $Z^{(1)} \sim |z|^{-3}\log|z|$ for large negative values of z, and $Z^{(1)} \sim |z|^{-3}[2\pi e^{1/(6\bar{\varepsilon}^2)} - \log|z|]$ for large positive z. Imposing particle-exchange symmetry yields

$$\mu_c \sim -1 + \delta\mu \quad \text{with} \quad \delta\mu = \pi^{-1}\exp[-1/(6\bar{\varepsilon}^2)]. \quad (12)$$

The splitting $\delta\mu$ is shown as a dashed black line in Figs. 2(b) and 2(c). It agrees with the numerical data for μ_c (blue) for small $\bar{\varepsilon}^2$ but breaks down for $\bar{\varepsilon}^2 \approx 0.1$.

We emphasize that the nonanalytic dependence (12) cannot be obtained by the $\bar{\varepsilon}$-perturbation theory described in Refs. [1,38,39]. That approach starts by rescaling $z \to \bar{\varepsilon}z$, and solves the resulting equation $\frac{d}{dz}(z + \bar{\varepsilon}z^2 + \frac{d}{dz})Z_\mu = \bar{\varepsilon}\mu z Z_\mu$ perturbatively in $\bar{\varepsilon}$. The solution remains essentially Gaussian. Even for very small $\bar{\varepsilon}$, however, the z dynamics can escape from $z \approx 0$ to $-\infty$ by forming caustics [1]. This gives rise to power-law tails that are not described by perturbation theory. Higher orders in $\bar{\varepsilon}$ improve the accuracy only locally, inside an $\bar{\varepsilon}$-sized "boundary layer" [40] around $z = 0$, but not in the tails. Consequently, perturbation theory fails to give the nonanalytical dependence (12) since all perturbative corrections to $\mu_c \sim -1$ vanish [32].

Our theory, by contrast, provides a uniform approximation valid for small $\bar{\varepsilon}$ and arbitrary z. It allows one to compute the exponentially small eigenvalue splitting $\delta\mu$ because it captures the formation of caustics. For small $\bar{\varepsilon}$, the rate J of caustic formation is $J \sim (2\pi)^{-1}e^{-1/6\bar{\varepsilon}^2}$ [1]. It follows that $\mu_c \sim 2J - 1$ at small $\bar{\varepsilon}$.

We now show that caustics cause similar problems in small-St expansions [1,11,41–44]. In one dimension, the equation for z reads in dimensional units

$$\frac{d}{dt}z = -\gamma z - z^2 + \gamma A(x,t). \quad (13)$$

The Stokes number used in DNS of heavy particles in turbulence [45,46] is $\kappa \equiv u_0/(\eta\gamma)$ [1]. We take A in Eq. (13) to be constant. In this "persistent limit" the local fluid-velocity gradients are roughly constant during the time η/u_0 [1]. As $\kappa \to 0$ we find that $z \sim A$, with distribution $P(A) = (6\pi u_0^2/\eta^2)^{-1/2}\exp[-A^2/(6u_0^2/\eta^2)]$, localized around zero. As in the white-noise case, this local approximation fails when caustics allow z to escape to $-\infty$. Kramers-escape theory for weak colored noise [47,48] reveals that caustics occur in the persistent limit when $A < -\gamma/4$, with probability $p = \int_{-\infty}^{-\gamma/4} dA\,P(A)$. Evaluating this integral for $\kappa \ll 1$, one obtains a nonanalytic dependence, $p \propto \exp[-1/(96\kappa^2)]$, consistent with Ref. [49]. In DNS a similar nonanalytic dependence is found [50], albeit of a slightly different form because the turbulent velocity gradients are non-Gaussian. We conclude that the perturbation theories in the white-noise limit and in time-correlated flows fail for the same reason. Both expansions are valid only locally near $z = 0$ and do not accommodate caustics.

IV. CONCLUSIONS

We analyzed the distribution of relative velocities in turbulence between small, heavy particles with different Stokes numbers St. We demonstrated that the difference in St causes diffusive relative motion at small separations, giving rise to a plateau in the distribution for relative velocities smaller than a cut off v_c. This is in qualitative agreement with DNS [51]. Figure 2 in Ref. [51] shows the v_r distribution for a bidisperse suspension. The cut off v_c depends linearly on both θ, the parameter characterizing the difference in Stokes numbers, and $\bar{\varepsilon}$, which is a measure for the mean Stokes number of the system. At small values of θ and $\bar{\varepsilon}$ the distribution exhibits algebraic tails $|v_r|^{\mu_c-d-1}$ as in the monodisperse case. The exponent μ_c is determined by the phase-space correlation dimension of a monodisperse system with mean Stokes number $\overline{\mathrm{St}}$. When $\overline{\mathrm{St}}$ is $\mathcal{O}(1)$ or larger, the moments of relative velocities at small separations are dominated by the tails of the distribution. As the parameters θ and $\bar{\varepsilon}$ become larger, both our simulations and the analysis of the white-noise model show that the tails gradually disappear, making space

for the diffusive (Gaussian) behavior below $v_c \propto \overline{\varepsilon}\,\theta$. The DNS of Ref. [51] are for quite large θ and $\overline{\varepsilon}$. It would be of interest to perform DNS for smaller parameter values to find the power-law tails we predict here.

Our analysis shows how sensitive the distribution is to polydispersity. This is important for experiments tracking the dynamics of micrometer-size particles in turbulence [9], where strict monodispersity is difficult to achieve.

We explained these observations by analyzing a one-dimensional statistical model in the white-noise limit. The difference in Stokes numbers regularizes the distribution, so that the bidisperse model has a power-law steady state at small $\overline{\varepsilon}$. This makes it possible to compute how the power-law exponent μ_c depends on the inertia parameter $\overline{\varepsilon}$. We demonstrated that the dependence of μ_c upon $\overline{\varepsilon}$ is not analytic.

Our theory explains why small-$\overline{\varepsilon}$ expansions fail to give nonanalytic contributions to physical quantities in the white-noise limit. It is likely that nonanalytic terms in white-noise expansions for the correlation dimension [32] and Lyapunov exponents [38,39] in two and three dimensions have similar origins, and we speculate that Eqs. (12) are only the first two terms in an infinite series of the form $\sum_{k=0}^{\infty} e^{-k/(6\overline{\varepsilon}^2)} \sum_{m=0}^{\infty} b_m^{(k)} \overline{\varepsilon}^{2m}$ [52], possibly also containing logarithmic terms, $\log^n \overline{\varepsilon}^2$.

We remark that the analysis of μ_c in the one-dimensional white-noise model is special insofar as its conventional perturbation expansion vanishes exactly [32], as mentioned above. This renders the nonanalytic correction (12) leading. In higher dimensions this is, however, not the case. We therefore expect perturbation theory to fail in these cases only when the nonanalytical terms become comparable to the perturbative ones. The Borel sum for the correlation dimension in two dimensions, for instance, fails only at $\overline{\varepsilon} \approx 0.1$ [32] where $\overline{\varepsilon}^2 \approx e^{-1/(6\overline{\varepsilon}^2)}$.

More generally we explained that small-St expansions for heavy particles in turbulence [1,11,41–44] suffer from similar problems when caustics occur. This indicates that matched asymptotic expansions (or similar methods) are required to explain the characteristic minimum [46] of the correlation dimension as a function of St.

Our predictions can be directly tested by experiments or by DNS of turbulent bidisperse turbulent suspensions. We note, however, that our analysis pertains to the dynamics in the dissipative range. At higher Stokes numbers, when separations between particle pairs explore the inertial range [53,54], we expect corrections to the power-law exponents derived here. Furthermore, strong intermittency is expected to increase the rate of caustic formation for heavy particles in turbulent flows. This could imply that the breakdown of perturbation theory for heavy particles in turbulent flows is perhaps even more pronounced than predicted by our model calculations.

ACKNOWLEDGMENTS

This work was supported by Vetenskapsrådet (Grant No. 2013-3992), Formas (Grant No. 2014-585), and by the grant "Bottlenecks for particle growth in turbulent aerosols" from the Knut and Alice Wallenberg Foundation, Dnr. KAW 2014.0048. The numerical computations used resources provided by C3SE and SNIC.

[1] K. Gustavsson and B. Mehlig, Statistical models for spatial patterns of heavy particles in turbulence, Adv. Phys. **65**, 1 (2016).

[2] S. Sundaram and L. R. Collins, Collision statistics in an isotropic particle-laden turbulent suspension, J. Fluid. Mech. **335**, 75 (1997).

[3] G. Falkovich, A. Fouxon, and G. Stepanov, Acceleration of rain initiation by cloud turbulence, Nature (London) **419**, 151 (2002).

[4] M. Wilkinson and B. Mehlig, Caustics in turbulent aerosols, Europhys. Lett. **71**, 186 (2005).

[5] M. Wilkinson, B. Mehlig, and V. Bezuglyy, Caustic Activation of Rain Showers, Phys. Rev. Lett. **97**, 048501 (2006).

[6] J. Bec, L. Biferale, M. Cencini, A. Lanotte, and F. Toschi, Intermittency in the velocity distribution of heavy particles in turbulence, J. Fluid Mech. **646**, 527 (2010).

[7] K. Gustavsson and B. Mehlig, Distribution of relative velocities in turbulent aerosols, Phys. Rev. E **84**, 045304 (2011).

[8] J. P. L. C. Salazar and L. R. Collins, J. Fluid Mech. **696**, 45 (2012).

[9] G. P. Bewley, E. W. Saw, and E. Bodenschatz, New J. Phys. **15**, 083051 (2013).

[10] V. Perrin and H. Jonker, Relative velocity distribution of inertial particles in turbulence: A numerical study, Phys. Rev. E **92**, 043022 (2015).

[11] J. Chun, D. L. Koch, S. L. Rani, A. Ahluwalia, and L. R. Collins, Clustering of aerosol particles in isotropic turbulence, J. Fluid Mech. **536**, 219 (2005).

[12] J. Bec, A. Celani, M. Cencini, and S. Musacchio, Clustering and collisions in random flows, Phys. Fluids **17**, 073301 (2005).

[13] M. Wilkinson, B. Mehlig, and V. Uski, Stokes trapping and planet formation, Astrophys. J. Suppl. **176**, 484 (2008).

[14] F. Windmark, T. Birnstiel, C. W. Ormel, and C. P. Dullemond, Breaking through: The effects of a velocity distribution on barriers of dust growth, Astron. Astrophys. **544**, L16 (2012).

[15] K. Gustavsson and B. Mehlig, Relative velocities of inertial particles in turbulent aerosols, J. Turbulence **15**, 34 (2014).

[16] A. Pumir and M. Wilkinson, Collisional aggregation due to turbulence, Ann. Rev. Condens. Matter Phys. **7**, 141 (2016).

[17] J. Schumacher, J. D. Scheel, D. Krasnov, D. A. Donzis, V. Yakhot, and K. R. Sreenivasan, Small-scale universality in fluid turbulence, Proc. Natl. Acad. Sci. USA **111**, 10961 (2014).

[18] K. Gustavsson, S. Vajedi, and B. Mehlig, Clustering of Particles Falling in a Turbulent Flow, Phys. Rev. Lett. **112**, 214501 (2014).

[19] J. Bec, H. Homann, and S. S. Ray, Gravity-Driven Enhancement of Heavy Particle Clustering in Turbulent Flow, Phys. Rev. Lett. **112**, 184501 (2014). .

[20] P. J. Ireland, A. D. Bragg, and L. R. Collins, The effect of Reynolds number on inertial particle dynamics in isotropic turbulence. Part 2. Simulations with gravitational effects, J. Fluid Mech. **796**, 659 (2016).

[21] V. Mathai, E. Calzavarini, J. Brons, C. Sun, and D. Lohse, Microbubbles and Microparticles are Not Faithful Tracers of Turbulent Acceleration, Phys. Rev. Lett. **117**, 024501 (2016).

[22] H. Parishani, O. Ayala, B. Rosa, L.-P. Wang, and W. W. Grabowski, Effects of gravity on the acceleration and pair statistics of inertial particles in homogeneous isotropic turbulence, Phys. Fluids **27**, 033304 (2015).

[23] K. Gustavsson, E. Meneguz, M. Reeks, and B. Mehlig, Inertial-particle dynamics in turbulent flows: Caustics, concentration fluctuations, and random uncorrelated motion, New J. Phys. **14**, 115017 (2012).

[24] H. J. Völk, F. C. Jones, G. E. Morfill, and S. Röser, Collisions between grains in a turbulent gas, Astron. Astrophys. **85**, 316 (1980).

[25] H. Mizuno, W. J. Markiewicz, and H. J. Völk, Grain growth in turbulent protoplanetary accretion disks, Astron. Astrophys. **195**, 183 (1988).

[26] W. J. Markiewicz, H. Mizuno, and H. J. Völk, Turbulence induced relative velocity between two grains, Astron. Astrophys. **242**, 286 (1991).

[27] L. Pan, P. Padoan, and J. Scalo, Turbulence induced relative velocity of dust particles. The bidisperse case, Astrophys. J. **791**, 48 (2014).

[28] M. James and S. S. Ray, Enhanced droplet collision rates and impact velocities in turbulent flows: The effect of polydispersity and transient phases, Sci. Rep. **7**, 12231 (2017); see also arXiv:1603.05880

[29] S. Belan, I. Fouxon, and G. Falkovich, Localization-Delocalization Transitions in Turbophoresis of Inertial Particles, Phys. Rev. Lett. **112**, 234502 (2014).

[30] M. Wilkinson and B. Mehlig, Path coalescence transition and its applications, Phys. Rev. E **68**, 040101 (2003).

[31] M. Wilkinson, R. Guichardaz, M. Pradas, and A. Pumir, Power-law distributions in noisy dynamical systems, Europhys. Lett. **111**, 50005 (2015).

[32] K. Gustavsson, B. Mehlig, and M. Wilkinson, Analysis of the correlation dimension of inertial particles, Phys. Fluids **27**, 073305 (2015).

[33] M. Wilkinson, B. Mehlig, and K. Gustavsson, Correlation dimension of inertial particles in random flows, Europhys. Lett. **89**, 50002 (2010).

[34] S. A. Derevyanko, G. Falkovich, K. Turitsyn, and S. Turitsyn, Lagrangian and Eulerian descriptions of inertial particles in random flows, J. Turbulence **8**, N16 (2007).

[35] H. Schomerus and M. Titov, Phys. Rev. E **66**, 066207 (2002).

[36] C. M. Bender and S. A. Orszag, *Advanced mathematical methods for scientists and engineers* (McGraw-Hill, New York, 1978).

[37] See Supplemental Material at http://link.aps.org/supplemental/10.1103/PhysRevE.96.061102 for additional details on the derivation of Eq. (11) and for a description of how to obtain the WKB solution for $Z_{-1}(z)$ that is used to obtain Eq. (12).

[38] B. Mehlig and M. Wilkinson, Coagulation by Random Velocity Fields as a Kramers Problem, Phys. Rev. Lett. **92**, 250602 (2004).

[39] K. Duncan, B. Mehlig, S. Östlund, and M. Wilkinson, Clustering in Mixing Flows, Phys. Rev. Lett. **95**, 240602 (2005).

[40] E. J. Hinch, *Perturbation methods* (Cambridge University Press, Cambridge, 1991).

[41] M. R. Maxey, The gravitational settling of aerosol particles in homogeneous turbulence and random flow fields, J. Fluid Mech. **174**, 441 (1987).

[42] T. Elperin, N. Kleeorin, and I. Rogachevskii, Self-Excitation of Fluctuation of Inertial Particle Concentration in Turbulent Fluid Flow, Phys. Rev. Lett. **77**, 5373 (1996).

[43] E. Balkovsky, G. Falkovich, and A. Fouxon, Intermittent Distribution of Inertial Particles in Turbulent Flows, Phys. Rev. Lett. **86**, 2790 (2001).

[44] M. Wilkinson, B. Mehlig, S. Östlund, and K. P. Duncan, Unmixing in random flows, Phys. Fluids **19**, 113303 (2007).

[45] J. Bec, L. Biferale, G. Boffetta, M. Cencini, S. Musacchio, and F. Toschi, Lyapunov exponents of heavy particles in turbulence, Phys. Fluids **18**, 091702 (2006).

[46] J. Bec, L. Biferale, M. Cencini, A. Lanotte, S. Musacchio, and F. Toschi, Heavy Particle Concentration in Turbulence at Dissipative and Inertial Scales, Phys. Rev. Lett. **98**, 084502 (2007).

[47] G. P. Tsironis and P. Grigolini, Color-Induced Transition to a Nonconventional Diffusion Regime, Phys. Rev. Lett. **61**, 7 (1988).

[48] A. J. Bray and A. J. McKane, Instanton Calculation of the Escape Rate for Activation over a Potential Barrier Driven by Colored Noise, Phys. Rev. Lett. **62**, 493 (1989).

[49] K. Gustavsson and B. Mehlig, Distribution of velocity gradients and rate of caustic formation in turbulent aerosols at finite Kubo numbers, Phys. Rev. E **87**, 023016 (2013).

[50] G. Falkovich and A. Pumir, Sling effect in collisions of water droplets in turbulent clouds, J. Atmos. Sci. **64**, 4497 (2007).

[51] L. Pan, P. Padoan, and J. Scalo, Turbulence-induced relative velocity of dust particles. III. The probability distribution, Astrophys. J. **792**, 69 (2014).

[52] G. Dorigoni, An introduction to resurgence, trans-series and alien calculus, arXiv:1411.3585.

[53] B. Mehlig, M. Wilkinson, and V. Uski, Colliding particles in highly turbulent flows, Phys. Fluids **19**, 098107 (2007).

[54] K. Gustavsson, B. Mehlig, M. Wilkinson, and V. Uski, Variable-Range Projection Model for Turbulence-Driven Collisions, Phys. Rev. Lett. **101**, 174503 (2008).

Paper C

https://arxiv.org/abs/1806.08207

Fractal dimensions and trajectory crossings in correlated random walks

A. Dubey,[1] J. Meibohm,[1] K. Gustavsson,[1] and B. Mehlig[1]

[1] *Department of Physics, University of Gothenburg, SE-41296 Gothenburg, Sweden*

(Dated: June 22, 2018)

We study spatial clustering in a discrete, one-dimensional, stochastic, toy model of heavy particles in turbulence and calculate the spectrum of multifractal dimensions D_q as functions of a dimensionless parameter, α, that plays the role of an inertia parameter. Using the fact that it suffices to consider the linearized dynamics of the model at small separations, we find that $D_q = D_2/(q-1)$ for $q = 2, 3, \ldots$. The correlation dimension D_2 turns out to be a non-analytic function of the inertia parameter in this model. We calculate D_2 for small α up to the next-to-leading order in the non-analytic term.

I. INTRODUCTION

Heavy particles in turbulent flows occur frequently in nature. Examples are small rain droplets in turbulent rain clouds [1], microscopic sand grains in the turbulent gas surrounding growing stars [2, 3], and microscopic plankton in ocean turbulence [4–7]. These turbulent aerosols show strong inhomogeneities in the spatial distribution of particles, in particular at small spatial scales [8]. Such small-scale spatial clustering was observed in experiments [1, 9], and in direct numerical simulations [10, 11].

Heavy particles may detach from the turbulent flow, so that their trajectories can cross. Tracer particles that are constrained to follow a velocity field, on the other hand, cannot cross paths, since any velocity field must be single-valued. The crossing of trajectories, therefore, is an inertial effect where particle phase-space manifolds fold back upon themselves, causing multi-valued particle velocities that can give rise to large collision velocities [12–17]. The loci in space that delineate the multi-valued regions are referred to as 'caustics' [18–20].

It is a challenge to describe turbulent aerosols from first principles because its analysis must take into account the underlying turbulence, a non-linear, out-of-equilibrium problem, with an infinite number of strongly coupled degrees of freedom [21]. Instead, a statistical approach to model particles in turbulence has been developed [8, 22]. In such statistical models one replaces the deterministic fluid velocity field by a smooth random function with prescribed statistics. In particular, statistical models of particles in turbulence have been useful in the study of small-scale clustering [23–26] caustic formation [14, 27], and have significantly advanced our understanding of heavy-particle dynamics in turbulence.

However, two important issues remain unresolved. First, inertial particles in turbulence have been numerically shown to cluster on multifractal sets [11], characterized by their multifractal dimensions D_q. The multifractal dimensions D_q measure the degree of inhomogeneity in the distribution of the particles as power-laws to the $q-$th mass moments [28, 29]. While the correlation dimension D_2 and the Lyapunov dimension (related to D_1) have been studied in quite some detail [8], little is known about general multifractal dimensions D_q. They have been calculated in the case of tracer particles in compressible flows [30]. This study, however, excludes trajectory crossings, since the velocities of tracer particles are single-valued. Second, the dependence of the correlation dimension D_2 on the inertia parameter (the Stokes number St) is not well understood. The correlation dimension D_2 shows a minimum as a function of St, an effect that is not captured by perturbation theory [31, 32]. Recently, it was argued that the formation of caustics could be the reason for the failure of perturbation theory in D_2 [33].

In this paper, we analytically calculate the spectrum of multifractal dimensions D_q and investigate the effect of the rate of trajectory crossings J on the multifractal dimensions D_q. We consider a statistical toy model to study the clustering of particles suspended in a turbulent flow. The model is a one-dimensional, discrete-time random walk model [34–36], which describes the discrete dynamics of an ensemble of random walks immersed in a flow field. The flow is taken to be a smooth, random velocity field to model turbulence in the dissipative range. Due to the flow field, random walks that are spatially close to each other are correlated and may travel together for some time. The model includes effects that are similar to particle inertia and the turbulent flow, other effects such as particle size and particle-particle interactions are disregarded. The dimensionless number α plays the role of an inertia parameter (the Stokes number St for heavy particles in turbulence). It is defined as the ratio of the mean-squared displacement and the correlation length. The long-time distribution of random walks in this model exhibits a statistical steady state with multifractal clustering. This behavior is similar to that of heavy inertial particles in incompressible turbulence, where the correlated displacement of nearby particles results in small-scale spatial clustering.

The motivation for considering the one-dimensional, discrete-time random walk model as a playground is twofold. Firstly, this model can be seen as a discretization of an over-damped, continuous, one-dimensional model of particles in turbulence. Secondly, we can analytically compute observables like D_q and J, which is not possible in the continuous-time models in two and three spatial

dimensions. This analytical control allows us to find exponentially small non-analytic contributions which could give insights into the physical phenomenon affecting clustering.

We find that the multifractal dimension spectrum D_q is related to the way in which particle trajectories cross and derive a relation between the multifractal dimensions and the correlation dimension, $D_q = D_2/(q-1)$ for $q = 2, 3, \ldots$. The same relation holds for deterministic hyperbolic systems [37, 38]. For small α, we use an implicit equation for the correlation dimension D_2 to derive a non-perturbative, asymptotic expansion of D_2 for small α.

We note that the multifractal dimensions are defined in the mathematical limit of vanishing particle separations. This is an unrealistic assumption for physical systems where the finite particle size sets a lower limit on smallest relevant length scale of the system. Therefore to match with experiment one must be able to describe clustering at finite separations between particles, and non-divergent average densities.

The paper is organized as follows: In Section II we motivate the random-walk model from the continuous one-dimensional stochastic model of particles in turbulence and discuss the details of the random-walk model. Next, in Section III we discuss the multifractal dimensions, and in Section IV we present the non-perturbative expansion of the correlation dimension D_2 in the limit $\alpha \to 0$. In Section V we derive the rate of trajectory crossings in the linearized, as well as in the full non-linear model, and compare with results obtained from simulations. In Section VI we use trajectory crossings to derive a relation between the multifractal dimensions D_q and the correlation dimension D_2. Section VII contains conclusions and discussions of the presented work. Technical details on finite-time Lyapunov exponents and the Mellin-Barnes transform are discussed in the appendices.

II. MODEL

We start with the equation of motion for an inertial particle in a one-dimensional continuous random flow [18],

$$\dot{x} = v \quad \text{and} \quad \dot{v} = \gamma\left[u(x(t),t) - v\right], \tag{1}$$

where x and v are the particle position and velocity respectively, and $u(x,t)$ is the fluid velocity at position x and time t. Taking the overdamped limit $\gamma \to \infty$ reduces the two equations (1) to a single equation,

$$\dot{x}(t) \sim u(x(t),t)\,, \tag{2}$$

the dynamics of tracer particles. Eq. (2) shows that the continuous overdamped model is non-inertial and has no trajectory crossings since the particle follows the single-valued fluid field $u(x(t),t)$. However, discretizing this model at a non-infinitesimal time step Δt reintroduces inertial effects. We obtain

$$x(t+\Delta t) = x(t) + u(x(t),t)\Delta t. \tag{3}$$

Fixing $\Delta t = 1$, we end up with the discrete, iterative dynamics

$$x_{n+1} = x_n + f_n(x_n), \tag{4}$$

where $x_n \equiv x(t_n)$ and $f_n(x_t) \equiv u(x(t_n), t_n)$. In order to model the spatial smoothness and the dynamics of the flow field $u(x(t),t)$ we take $f_n(x)$ to be a Gaussian random function with zero mean and correlation function

$$\langle f_m(x) f_n(0)\rangle = \delta_{mn}\sigma^2 \exp\left(-\frac{x^2}{2\eta^2}\right) \tag{5}$$

which defines the mean-squared displacement σ, and correlation length η. The brackets $\langle \ldots \rangle$ denote an average taken over a large ensemble of walkers with different initial conditions. The system size L introduces an additional length scale in the system. We impose periodic boundary conditions with period L on the equations of motion. The equation of motion can be dedimensionalized with the correlation length η by changing coordinates according to $x \to \eta x$ and $f_n \to \eta f_n$. We find that the model depends on the dimensionless parameters

$$\alpha \equiv \frac{\sigma}{\eta}\,, \quad \text{and} \quad l \equiv \frac{L}{\eta}\,. \tag{6}$$

The multifractal steady-state distribution of particle positions is obtained by iterating an initial density of N walkers. $\{x_0^{(k)},\ k = 1, \ldots, N\}$ a large number of times $n \gg 1$ according to the dynamics (4).

III. MULTIFRACTAL DIMENSIONS

The fractal dimension spectrum D_q, where $q \in \mathbb{R}$, quantifies the nature of singularities of the spatial distribution $P(x_n)$ of the set of walkers S_n and describes the inhomogeneity of the fractal [37, 38]. For instance, a fractal set with a homogeneous distribution of points has for all q, q', $D_q = D_{q'}$. However, in general $D_q \geq D_{q'}$ if $q < q'$ [39, 40]. The fractal dimensions are defined by the scaling relation

$$\langle m_{x,\varepsilon}^{q-1}\rangle \sim \varepsilon^{(q-1)D_q} \tag{7}$$

in the limit of $\varepsilon \to 0$, where $m_{x,\varepsilon}$ is the number of walkers in an ε-interval around a reference walker located at x, and $\langle \cdots \rangle$ is an average obtained by using all walkers as reference walkers. For integer values of q larger than one, $q = 2, 3, \ldots$, D_q may alternatively be defined, and more efficiently calculated from simulations, by following the positions $\{x_n^{(k)},\ k = 1, \ldots, q\}$ of q walkers, given that $n \gg 1$. We have [30, 39]

$$\langle m_{x,\varepsilon}^{q-1}\rangle = P(Y_n^{(q)} \leq \varepsilon)\,, \tag{8}$$

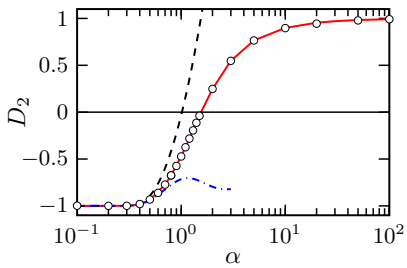

FIG. 1. Correlation dimension as a function of α. Shown is the numerical solution of Eq. (12), solid red line, the leading-order of Eq. (19), dashed line, the resummation (see Appendix B) of the asymptotic approximation to D_2, Eq. (14), dash-dotted blue line, and results of numerical simulations (symbols).

where the $Y_n^{(q)}$ are defined as

$$Y_n^{(q)} = \max_{1\le i,j\le q} \{|x_n^{(i)} - x_n^{(j)}|\} . \tag{9}$$

In the limit of small separations it follows from Eq. (7) that

$$P(Y_n^{(q)} \le \varepsilon) \sim \varepsilon^{(q-1)D_q} , \qquad \varepsilon \ll 1 . \tag{10}$$

In Section VI we use Eq. (10) to find a relation between the correlation dimension D_2 and the multifractal dimensions D_q.

IV. CORRELATION DIMENSION

The (fractal) correlation dimension D_2 is of particular physical importance. As Eq. (10) suggests, D_2 measures the power-law singularity of the probability density of separations, $P(|\delta x_n| = \varepsilon)$, at small separations [37, 41]. More precisely, we obtain by using Eq. (10) the relation

$$P(|\delta x_n| = \varepsilon) = \frac{\mathrm{d}}{\mathrm{d}\varepsilon} P(|\delta x_n| \le \varepsilon) \sim \varepsilon^{D_2 - 1} . \tag{11}$$

The authors of Ref. [36] calculated D_2 for the present model, using a a short-time approximation for the Liouville operator. They derived the implicit formula

$$\Gamma\left[\frac{-D_2+1}{2}\right] {}_1F_1\left[\frac{D_2}{2}; \frac{1}{2}; -\frac{1}{2\alpha^2}\right] = \pi^{\frac{1}{2}} (\sqrt{2}\alpha)^{D_2} . \tag{12}$$

It was shown that this relation admits a solution with $0 < D_2 < 1$ for all $\alpha > \alpha_c \approx 1.56$, which is in line with the requirement that $P(|\delta x_n|)$ be normalizable.

In turn, for $\alpha < \alpha_c$, Eq. (12) still has a non-trivial solution but with negative correlation dimension $D_2 < 0$. Fig. 1 shows $D_2(\alpha)$ as predicted by the relation (12) as the red solid line. A negative correlation dimension seemingly results in a non-normalizable density $P(|\delta x_n| = \varepsilon)$ due to the divergence at small separations according to Eq. (11).

As discussed in Refs. [33, 42, 43] one can make sense of the correlation dimension also for $D_2 < 0$ by regularizing the dynamics at small separations. This is done by adding a weak additional random 'noise' to Eq. (4) according to

$$x_{n+1} = x_n + f_n(x_n^{(1)}) + \xi_n . \tag{13}$$

Here, ξ_n are independent identically distributed Gaussian random variables with zero mean and variance $\langle \xi_n^2 \rangle = \kappa^2$. As the noise ξ_n is purely auxiliary, we choose κ small, in particular, $\kappa \ll \alpha$. Therefore, ξ_n cuts off the power law in (11) at small ε, which results in a uniform distribution at scales up to $\varepsilon \approx \kappa$. For $\kappa \ll \varepsilon \ll 1$, on the other hand, the distribution of separations now follows the power law (11) with negative correlation dimension $D_2 < 0$ [43]. A negative D_2 is not in contradiction with $P(|\delta x| = \varepsilon)$ being normalizable because of the small-scale cut-off at $\varepsilon \approx \kappa$. A noise term similar to the one in Eq. (13) has been shown to arise naturally in turbulent suspensions of heavy particles of different sizes [25, 33, 44]. The white symbols in Fig. 1 are results of numerical simulations for D_2 obtained by measuring the scaling of $P(|\delta x_n| = \varepsilon)$ for $\kappa \ll \varepsilon \ll 1$, using the regularized dynamics (13). We observe excellent agreement with the prediction provided by Eq. (12) for both positive and negative D_2.

The numerics and the simulations shown in Fig. 1 suggest that $D_2 \sim -1$ for $\alpha \ll 1$. Corrections to this relation are found by making the ansatz $D_2 \sim -1 + \beta(\alpha)$ with $\beta(\alpha) \ll \alpha \ll 1$ in Eq. (12) and solving for $\beta(\alpha)$. We find the asymptotic expansion

$$\begin{aligned} D_2 \sim -1 &+ \frac{\mathrm{e}^{-1/(2\alpha^2)}}{\sqrt{2\pi}} (4\alpha - 14\alpha^3 + 63\alpha^5 - \frac{905}{2}\alpha^7 + \dots) \\ &+ \frac{\mathrm{e}^{-1/\alpha^2}}{2\pi} [16\gamma\alpha^2 - 4(3 + 28\gamma)\alpha^4 + (\frac{170}{3} + 700\gamma)\alpha^6 - \dots] \\ &+ \frac{\mathrm{e}^{-1/\alpha^2}}{2\pi} \log(\alpha^2/2)[-8\alpha^2 + 56\alpha^4 - 350\alpha^6 + \dots], \end{aligned} \tag{14}$$

where γ denotes the Euler-Mascheroni constant. The details of the calculation that lead to Eq. (14) can be found in Appendix B. The asymptotic expansion for D_2 in Eq. (14) is shown in Fig. 1 as the blue dash-dotted line, and is seen to be an excellent approximation up to $\alpha \approx 0.4$. The subleading asymptotic terms of the order $\exp(-1/\alpha^2)$ and logarithmic contributions in Eq. (14) have been obtained by using the Mellin-Barnes technique, which is described in more detail in Appendix C.

Previous calculations of the correlation dimension performed using perturbation theory did not capture the non-analytic terms of the form $\exp(-1/(2\alpha^2))$. The leading order non-analytic contributions for D_2 in the continuous one-dimensional model were obtained in [33]. In Eq. (14) we have calculated the corresponding non-analytic contributions to next-to-leading order for the present model. Series of the form in Eq. (14) occur in

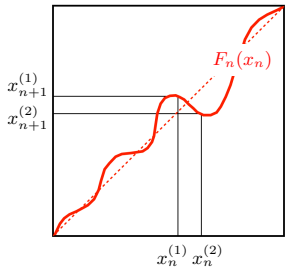

FIG. 2. An illustration of crossing trajectories: $x_n^{(1)} < x_n^{(2)}$ is mapped to $x_{n+1}^{(1)} > x_{n+1}^{(2)}$. For close-by particles this occurs where $F_n' < 0$. The thick solid red line shows a realization of the random function $F_n(x_n)$. The dashed line shows $x_{n+1} = x_n$.

quantum mechanics and quantum-field theory, and are referred to as 'trans series' [45–48].

V. CROSSING TRAJECTORIES

The iterative dynamics defined by Eq. (4) allows for trajectory crossings of nearby random walkers. Crossings occur when the random map that generates the iterations,

$$F_n(x) \equiv x + f_n(x), \tag{15}$$

has realizations that are not one-to-one. Since the realizations F_n are smooth, a necessary condition for F_n to be one-to-one is that its derivative is positive everywhere, $F_n' > 0$. In turn, trajectories of nearby walkers may cross if there are finite regions in x for which this derivative is not positive, $F_n'(x) \le 0$. Fig. 2 schematically depicts a realization $F_n(x)$ that is multivalued and two walkers whose trajectories cross.

The crossing rate J for two infinitesimally close walkers can be obtained by linearizing the dynamics of separations of two particles. The separation $\delta x_n = x_n^{(1)} - x_n^{(2)}$ of two close-by walkers obeys the asymptotic dynamics

$$\delta x_{n+1} \sim (1 + A_n)\, \delta x_n, \qquad |\delta x_n| \ll 1\,, \tag{16}$$

where A_n are identically distributed Gaussian random variables with zero mean and variance $\langle A_n^2 \rangle = \alpha^2$, see Appendix A for a related discussion of the calculation of Lyapunov exponents from the linearized dynamics. Crossings occur when the separation δx_n changes sign between two subsequent time steps of (16). Thus a sufficient condition for a crossing in the linearized dynamics is that $A_n < -1$. At each time step, the probability $P(A_n < -1)$ and, hence, the rate of crossing J at small

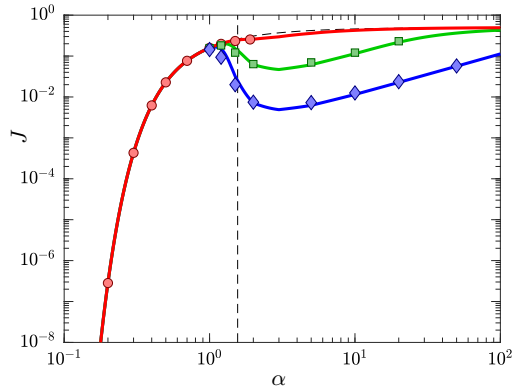

FIG. 3. Probability of trajectory crossing J against α. The black dashed line shows the theoretical prediction from the linearized model, Eq. (17). The colored lines show the rate of crossings obtained from the non-linear model theoretically, Eq. (24), and from simulations with $l = 10$ (red circles), $l = 10^2$ (green boxes), $l = 10^3$ (blue diamonds). The vertical black line shows $\alpha_c = 1.56$

separation is given by

$$J \sim P(A_n < -1) = \int_{-\infty}^{-1} \frac{\mathrm{d}A_n}{\sqrt{2\pi\alpha^2}}\, \mathrm{e}^{-A_n^2/(2\alpha^2)},$$
$$= \frac{1}{2}\mathrm{erfc}(1/\sqrt{2\alpha^2}), \qquad |\delta x_n| \ll 1, \tag{17}$$

where erfc is the complementary error function. For small α, J is exhibits an exponential activation according to

$$J \sim \frac{\alpha\, \mathrm{e}^{-1/(2\alpha^2)}}{\sqrt{2\pi}}, \qquad \alpha \ll 1\,. \tag{18}$$

The rate of trajectory crossing J is the analogue to the rate of caustic formation $\mathcal{J}$ in the corresponding one-dimensional continuous model for inertial particles in turbulence [8, 27]. Interestingly, $\mathcal{J}$ shows a similar activation in the weak-inertia limit. Furthermore, using the leading-order term in Eq. (14) and Eq. (18) we find

$$D_2 \sim -1 + 4J\,, \qquad \alpha \ll 1\,. \tag{19}$$

In the regime $\alpha \ll 1$ the Lyapunov exponent is negative, $\lambda < 0$ so a pair of trajectories converge towards each other. If the rate of trajectory crossings was identically 0, the trajectories would eventually fuse together giving $D_2 = -1$. A non-zero value of J leads of the trajectories oscillating around each other and causing a spread in the distribution of particles, thereby reducing clustering i.e. forcing $D_2 > -1$. A similar relation between D_2 and $\mathcal{J}$ has recently been found in the corresponding continuous white-noise model, namely $D_2 \sim -1 + 2\mathcal{J}$ [33].

The expression for J given in (17) is a good approximation for the rate of trajectory crossings in the full

(non-linear) model as long as most crossings occur between nearby trajectories. That is the case if $\alpha < \alpha_c$, when the Lyapunov exponent of the system is negative and trajectories spend most of their time close together (see Appendix A) regardless of the size of l. For $\alpha > \alpha_c$, in turn, trajectories spend most of their time far apart so that crossings are more likely to occur at larger separations. Moreover the likelihood of two trajectories traveling away from each other increases as l increases. This leads to an increase in deviations from the linearized rate of crossings as l increases. Crossings at larger separation are not described by the linearized model, Eq. (16). Fig. 3 shows the probability of trajectory crossing in the linearized dynamics J (black dashed line) and numerical simulations of the full model (markers) as functions of α for different values of l. The data suggests that Eq. (17) is an excellent approximation to the exact probability of trajectory crossing up to values $\alpha \approx \alpha_c$.

The rate of trajectory crossings in the full non-linear model can be obtained as follows. The equation of motion for the separation between two particles δx_n is

$$\delta x_{n+1} = \delta x_n + \delta f_n, \tag{20}$$

where $\delta f_n := f_n(x_n^{(1)}) - f_n(x_n^{(2)})$. The probability of a trajectory crossing is given by the probability of the separation changing sign between two subsequent time steps. That means

$$J = P(\delta x_{n+1} < 0; \delta x_n > 0) + P(\delta x_{n+1} > 0; \delta x_n < 0), \tag{21}$$

where $P(A; B)$ is the joint probability of events A and B. Using particle-interchange symmetry, Eq. (20), and factorization of the joint probability due to the independence of δf_n and δx_n, we can write Eq. (21) as

$$J = 2\int_0^\infty \mathrm{d}\varepsilon\ P(\delta f_n < -\varepsilon) P(\delta x_n = \varepsilon). \tag{22}$$

Because δf_n is a sum of two Gaussian random functions, it is itself a Gaussian random function, with zero mean and variance

$$\langle (\delta f_n)^2 \rangle = 2\alpha^2 (1 - e^{-\delta x_n^2/2}) \equiv v(\alpha, \delta x_n), \tag{23}$$

so that $P(\delta f_n < -\varepsilon) = \mathrm{erfc}(\varepsilon/\sqrt{2v(\alpha,\varepsilon)})/2$. Using integration by parts, this gives

$$J = -\frac{1}{2}\int_0^\infty \mathrm{d}\varepsilon P(|\delta x_n| \le \varepsilon) \frac{\mathrm{d}}{\mathrm{d}\varepsilon} \mathrm{erfc}\left(\frac{\varepsilon}{\sqrt{2v(\alpha,\varepsilon)}}\right). \tag{24}$$

Note first that for $\varepsilon \ll 1$ the term $\mathrm{erfc}(\varepsilon/\sqrt{2v(\alpha,\varepsilon)})$ has the asymptotic form

$$\mathrm{erfc}(\varepsilon/\sqrt{2v(\alpha,\varepsilon)}) \sim \mathrm{erfc}(1/\sqrt{2\alpha^2}). \tag{25}$$

Using this, we infer from Eq. (24) that $J = \mathrm{erfc}(1/\sqrt{2\alpha^2})/2$ as in the linear model (see Eq. (17)) if $P(|\delta x_n| = \varepsilon)$ is concentrated at $\varepsilon = 0$. That is the case when $\alpha < \alpha_c$, so that the rate of crossings in the full model reduces to the one obtained from the linearized model for $\alpha < \alpha_c$, as expected.

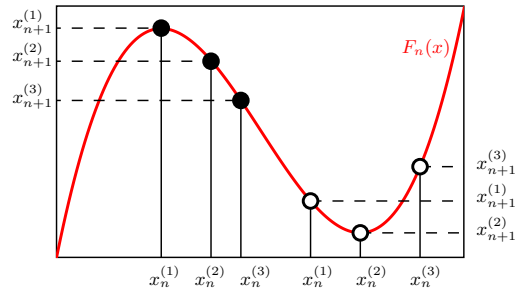

FIG. 4. Illustrates different types of crossings. When the particles are in an approximately linear regime of the flow or close enough together (filled bullets on the left), then the identity of the pair with maximal position distance does not change. When the particles are further apart so that the non-linearity of F_n becomes important, the identity of the pair with maximum position distance may change (white bullets on the right).

For $\alpha > \alpha_c$, $P(|\delta x_n| \le \varepsilon)$ is a non-trivial function of ε so that J differs from the rate of trajectory crossings in the linearized model Eq. (17). More precisely, we see that $J \le \mathrm{erfc}(1/\sqrt{2\alpha^2})/2$ for all α since $P(|\delta x_n| \le \varepsilon) \le 1$.

In order to evaluate J for $\alpha > \alpha_c$ we need an expression $P(|\delta x_n| \le \varepsilon)$ that is valid for any value of ε. Eq. (11), however, is valid only at small ε. Including the small-scales noise and because we expect particles to be uncorrelated at larger ε, we make the following ansatz for the cumulative probability distribution:

$$P(|\delta x_n| \le \varepsilon) = \frac{1}{l} \times \begin{cases} \varepsilon (x^*/x_0)^{1-D_2} & \text{if } 0 < \varepsilon \le x_0, \\ \varepsilon^{D_2} x^{*1-D_2} & \text{if } x_0 < \varepsilon \le x^*, \\ \varepsilon & \text{if } x^* < \varepsilon \le l. \end{cases} \tag{26}$$

Here x_0 is a small length scale related to the regularizing noise in Eq. (13), and x^* is an arbitrary matching scale of order unity for the transition between the power law behavior of $P(|\delta x_n| \le \varepsilon)$ and the large-scale uniform behavior. For $|\delta x_n| < x_0$ the dynamics is dominated by the noise term, and so the distribution is uniform. The solid lines in Fig. 3 show results of numerical integration of Eq. (24) using Eq. (26) with $x^* = 3$. We observe excellent agreement with simulations.

In what follows, we denote the crossings that are governed by the linearized model Eq. (16) 'linear crossings'. Since we expect non-linear terms to play a role at larger α, we call crossings that are not described by Eq. (16) but only by the full (non-linear) model Eq. (4) 'non-linear crossings', Fig. 4.

VI. A RELATION BETWEEN MULTIFRACTAL DIMENSIONS USING TRAJECTORY CROSSINGS

Having discussed the multifractal dimensions and trajectory crossings in our model we now turn to the effects of trajectory crossings on clustering. We find that arguments about trajectory crossings lead to a relation between the multifractal dimensions D_q.

First, consider how multifractal dimensions D_q as defined in Sec. III are related for $q = 2, 3, \ldots$. As Eq. (18) suggests the probability of trajectory crossings is exponentially small for $\alpha \ll 1$. As a first approximation let us assume that there are no crossings for small α. This approximation has interesting consequences for the $Y_n^{(q)}$ defined in Eq. (9). Namely, if particle trajectories do not cross, the particle pair that has the largest separation at time step n will have the largest separation also at any later time step, thus $Y_n^{(q)} = Y_n^{(2)}$, where $Y_n^{(2)}$ is obtained by considering only the two particles which initially had the largest separation. This means that we may follow the trajectories of the walker pair with the largest separation, without considering the other walkers. As a consequence we get for $Y_n^{(q)}$, $n \gg 1$:

$$P(Y_n^{(q)} \leq \varepsilon) \propto P(Y_n^{(2)} \leq \varepsilon). \tag{27}$$

Now consider the possibility of linear crossings as defined in the end of Sec. V. To that end, we name the walkers according to their order at step n, i.e. here and in the following,

$$x_n^{(1)} \leq x_n^{(2)} \cdots \leq x_n^{(q)}\,. \tag{28}$$

It follows that at step n, $Y_n^{(q)} = |x_n^{(1)} - x_n^{(q)}|$. If the mutual separations of all walkers are small, in which case $Y_n^{(q)} \ll 1$, crossings between the trajectories of $x^{(1)}$ and $x^{(q)}$ are almost always of the linear kind. A linear crossing of q walkers at time step n leaves the outermost walkers invariant, i.e., the crossing changes $x_n^{(1)}$ to $x_{n+1}^{(q)}$ and $x_n^{(q)}$ to $x_{n+1}^{(1)}$. Hence, $Y_{n+m}^{(q)} = Y_{n+m}^{(2)}$ for all m if all crossings are linear, just as in the case of no crossings. It follows that Eq. (27) holds also if $Y_n^{(q)} \ll 1$ for all $n \gg 1$. Using Eqs. (27) and (10) gives the following relation between D_2 and D_q:

$$D_q = \frac{D_2}{q-1}. \tag{29}$$

Note that one can show that $D_q \geq 1/(1-q)$, see Appendix A. Using Eq. (29) it is trivial to generalize the relations (14) and (19) to all D_q with $q = 2, 3, \ldots$. Note that the argument above holds true for any finite value of α because we may always take ε in Eq. (27) small enough so that $Y_n^{(q)} \ll 1$ for all $n \gg 1$. In practice this means, however, that as α becomes larger and the Lyapunov exponent λ increases, it becomes increasingly hard to verify Eq. (29) numerically. Fig. 5**a** shows a comparison of D_q in Eqs. (29) and (12) to D_q evaluated from the scaling exponent in Eq. (10) using numerical simulations. We observe good agreement within the limits of numerical accuracy if α is not too large or if $q = 2$. For $q > 2$ and $\alpha > \alpha_c$ the convergence of the simulations to theory is slow and very small scales must be resolved, see Fig 5**b** and discussion below.

We remark that we have not considered non-linear crossings in our discussion. This kind of crossing in general does not leave the outermost walker pair invariant. In our simulations it was possible to observe non-linear crossings already at small but finite values of ε. In Fig 5**b** the scaling exponent $(q-1)D_q$ is measured numerically as a function of ε for $\alpha > \alpha_c$. For $q = 2$ the expected value $(q-1)D_q = D_2$ from Eq. (29) is obtained for moderately large separations ε. For $q > 2$, the simulation data converge slowly towards this value as ε decreases and we observe a significant deviation from Eq. (29) already at small but finite ε, which we attribute to the occurrence of non-linear crossings in the model.

Physical systems are typically equipped with a natural cutoff scale ε_0 that may be, for example, a finite walker size or a regime where small-scale diffusion dominates. We expect the physically relevant observables in realistic systems to be not the $\varepsilon \to 0$ scaling exponents D_q but suitably defined, finite size counterparts $D_q(\varepsilon_0)$. A more detailed study of $D_q(\varepsilon_0)$ is left for future work.

VII. CONCLUSIONS

We studied clustering of heavy particles in turbulence by means of a simple one-dimensional discrete-time model. As the main result, we derived an intriguing relation between the multifractal dimensions D_q and the correlation dimension D_2, $D_q = D_2/(q-1)$ and verified it for different values of q by numerical simulations. A related expression for D_q has been previously derived for hyperbolic systems without trajectory crossings in [30]. We show here that it is valid also for the present model, which is non-hyperbolic and allows for trajectory crossings. Furthermore, the derivation of Eq. (29) via Eq. (10) leads to the important insight that $(q-1)D_q = D_2$ holds true only if the rate of non-linear crossings is negligible compared to the rate of linear crossings. Mathematically, this is ensured because the multifractal dimensions D_q are *defined* in the limit of infinitesimal separations, $\delta x \to 0$, where all crossings are linear.

However, to observe the relation $D_q = D_2/(q-1)$ in real systems one would need to have an large number of particles in a given volume. In contrast, systems of interest such as turbulent aerosols typically contain only a small number density of particles, of the order of a few of particles per Kolmogorov length cubed [49]. This leads to the conclusion that it would be interesting to study clustering for small average particle densities. Due to the natural small scale cut-off imposed by the particle size, a relevant quantity to calculate would be multifrac-

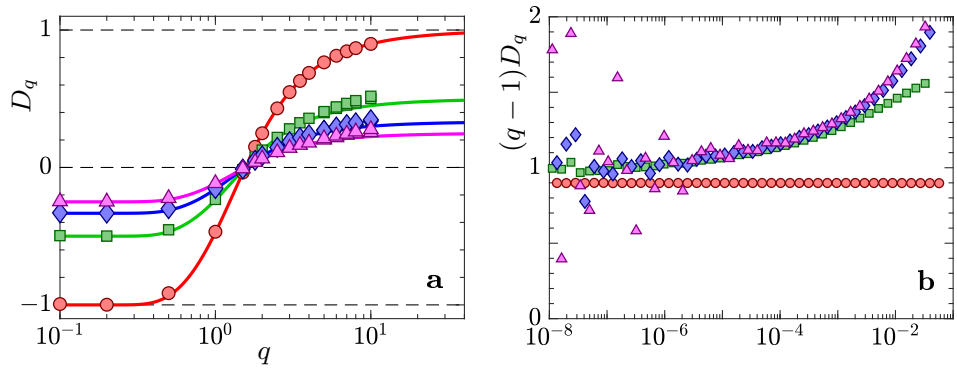

FIG. 5. Generalized fractal dimensions determined from numerical simulations using Eqs. (7) and (8). Panel **a** shows D_q as functions of α. The solid lines represent the theoretical predictions obtained using Eqs. (12) and (29) and the symbols represent numerical simulations. Circles (red) correspond to $q = 2$, squares (green) to $q = 3$, diamonds (blue) to $q = 4$, and triangles (pink) to $q = 5$. Panel **b** shows numerical simulation data for the local scaling exponent $(q-1)D_q$ in the relation $P(Y \leq \varepsilon) \sim \varepsilon^{(q-1)D_q}$ as a function of ε for $\alpha = 10$. Marker shapes corresponds to $q = 2, 3, 4, 5$ as in panel **a**. Horizontal dashed line shows $D_2 = 0.90$.

tal dimensions at non-zero separation, $D_q(\varepsilon)$, instead of the usual D_q defined at infinitesimal separations.

Further, we analyzed the correlation dimension D_2 in the limit $\alpha \to 0$. We found that naive perturbation theory fails because D_2 is non-analytic at $\alpha = 0$. Our results indicate that the small-α expansion of D_2 is a trans-series of the general form

$$D_2 = \sum_{k,l,m} c_{klm} \mathrm{e}^{-k/(2\alpha^2)} \alpha^l \log^m(\alpha^2/2)\,. \qquad (30)$$

An intensively studied example of a trans-series is the quantum-mechanical energy spectrum of a particle in a double well [50, 51]. There, the exponential contributions have a clear physical interpretation in terms of instantons, that is, collective excitations due to the presence of the degenerate potential minima. The corresponding power-series, in turn, are related to fluctuations around these instantons whereas logarithmic corrections are due to so called quasi-zero-modes [48]. In the present model, Eq. (19) suggests that the multi-valuedness caused by crossing trajectories gives rise to similar instanton contributions. We expect that perturbation expansions for heavy-particle dynamics in turbulence have a similar structure, for expansions in the Stokes number, and also for related perturbation expansions in the white-noise limit [8, 33]. This would explain why the perturbation calculations of the correlation dimension in Refs. [31, 52] appear to miss important contributions. More generally, our results give novel insight into the mathematical structure that links fractal clustering with caustic formation in the dynamics of heavy particles in turbulence, since the singularities that make crossing of trajectories possible in the random-walk model correspond to caustic singularities in turbulent aerosols.

Appendix A: Finite-Time Lyapunov exponents

The probability density function $P(\lambda_n)$ of finite-time Lyapunov exponents λ_n characterizes the leading asymptotic behavior of particle pairs after a large number of time steps $n \gg 1$ of the dynamics (4). This distribution is assumed to have the large deviation form [53]

$$P(\lambda_n) \approx \mathrm{e}^{-nI(\lambda_n)}\,, \qquad (A1)$$

where $I(\lambda_n)$ is called 'rate function'. The infimum of $I(\lambda_n)$ determines the most likely value, λ, that λ_n takes after $n \gg 1$ iterations. We call this value λ such that $I(\lambda) = \inf_{\lambda_n} I(\lambda_n)$ the (ordinary) Lyapunov exponent. It is defined in the strict limit $n \to \infty$ according to

$$\lambda \equiv \lim_{|\delta x_0| \to 0} \lim_{n \to \infty} \left\langle \log \left| \frac{\delta x_n}{\delta x_0} \right| \right\rangle, \qquad (A2)$$

where δx_n is the n^{th} iteration of the initial separation δx_0. As shown in [36], λ can be evaluated explicitly in the present model by considering the equation of motion for separations $\delta x_n = x_n^{(1)} - x_n^{(2)}$ of the momentary position of the two particles after n iterations, $x_n^{(1)}$ and $x_n^{(2)}$, respectively. In this section, we extend the calculation in [36] by providing an analysis of the distribution of finite-time Lyapunov exponents. We start out by using Eq. (4) to derive an equation for δx_n given by

$$\delta x_{n+1} = \delta x_n + f_n(x_n^{(1)}) - f_n(x_n^{(2)})\,. \qquad (A3)$$

Linearizing the smooth function f_n for small separations $\delta x_n \ll 1$ we readily obtain

$$\frac{\delta x_{n+1}}{\delta x_n} \sim 1 + f_n'(x_n^{(1)})\,. \qquad (A4)$$

Because f_n and f_m are uncorrelated for $n \neq m$, we can neglect the dependence of the right-hand side on $x_n^{(1)}$. This way, $f_n'(x_n^{(1)}) \equiv A$ simplifies to a single Gaussian random variable with $\langle A \rangle = 0$ and variance $\langle A^2 \rangle = \alpha^2$. Using this, we solve the iteration in Eq. (A4) and get

$$\log \left| \frac{\delta x_n}{\delta x_0} \right| \sim \sum_{k=1}^{n} \log |1 + A| \,. \tag{A5}$$

By assuming ergodicity, we can replace the ensemble average over initial separations in Eq. (A2) by the sample mean of $\log |1 + A|$. We find a simple equation for the finite-time Lyapunov exponent given by

$$\lambda_n = \frac{1}{n} \sum_{k=1}^{n} \log |1 + A| \,, \qquad n \gg 1 \,. \tag{A6}$$

We use the Varadhan method [53] to obtain the rate function for the sample mean in Eq. (A6). To this end, we first calculate the moment generating function of $\log |1 + A|$ according to

$$\begin{aligned} \langle \mathrm{e}^{k \log |1+A|} \rangle &= \int_{-\infty}^{\infty} \frac{\mathrm{d}A}{\sqrt{2\pi\alpha^2}} \, \mathrm{e}^{-A^2/(2\alpha^2)} \, |1 + A|^k \\ &= \pi^{-\frac{1}{2}} 2^{\frac{k}{2}} \alpha^k \Gamma \left[\frac{k+1}{2} \right] {}_1F_1 \left[-\frac{k}{2}; \frac{1}{2}; -\frac{1}{2\alpha^2} \right] , \end{aligned} \tag{A7}$$

where Γ is the gamma function and ${}_1F_1$ is the Kummer hypergeometric function. According to Varadhan's theorem, the cumulant generating function $\Lambda(k) = \log \langle \mathrm{e}^{k \log |1+A|} \rangle$ and the rate function $I(\lambda_n)$ are related by Legendre transform. We have

$$I(\lambda_n) = \sup_k \{ \lambda_n k - \Lambda(k) \}. \tag{A8}$$

Because $\Lambda(k)$ is a smooth function, we can replace the supremum in Eq. (A8) by the maximum and the relation $\lambda_n = \Lambda'(k)$ holds.

The Lyapunov exponent λ given in Ref. [36] is recovered from the moment generating function:

$$\begin{aligned} \lambda &= \left. \frac{\mathrm{d}}{\mathrm{d}k} \right|_{k=0} \langle \mathrm{e}^{k \log |1+A|} \rangle \,, \\ &= \int_{-\infty}^{\infty} \frac{\mathrm{d}A}{\sqrt{2\pi\alpha^2}} \, \mathrm{e}^{-A^2/(2\alpha^2)} \, \log |1 + A| \,. \end{aligned} \tag{A9}$$

Evaluation of the integral shows that $\lambda < 0$ for small α and that it changes sign at $\alpha_c \approx 1.56$ to become positive at larger α. This transition was called 'path-coalescence transition' [18, 36], because all paths coalesce in the limit of $n \to \infty$ for $\alpha < \alpha_c$. Below we derive a relation between the distribution of finite-time Lyapunov exponents λ_n and the fractal dimension spectrum D_q for our model. From arguments based on large-deviation theory, Pikovsky [42] derived an expression for the correlation dimension D_2 that applies directly to our model. In terms of the cumulant generating function $\Lambda(k)$ the author showed that

$$\Lambda(-D_2) = 0 \,. \tag{A10}$$

Using Eq. (29) we can generalize this relation to $q = 2, 3, \ldots$ according to

$$\Lambda\big(-(q-1)D_q \big) = 0 \,. \tag{A11}$$

Condition (A11) is equivalent to

$$\min_{\lambda_n} \{ \lambda_n (q-1) D_q + I(\lambda_n) \} = 0 \,. \tag{A12}$$

Related expressions were first derived for deterministic hyperbolic systems [37, 38], and for particles advected in compressible random velocity fields [30]. The discussion given here shows that the relations (A10) and (A12) also apply to the present system which includes trajectory crossings and is not deterministic and non-hyperbolic.

Eq. (A11) can alternatively be written as an integral fluctuation relation for the random quantity $(q-1)D_q \log |1 + A|$ according to

$$\langle \mathrm{e}^{-(q-1)D_q \log |1+A|} \rangle = 1 \,. \tag{A13}$$

Using Jensen's inequality and $\lambda = \langle \log |1 + A| \rangle$ (see Eq. (A9)), it follows directly that

$$D_q \lambda \geq 0 \,, \tag{A14}$$

for $q = 2, 3, \ldots$. This clearly shows that if $\lambda < 0$, we must have $D_q < 0$ and vice versa, in accordance with observation.

Furthermore, using Eq. (A12), we now show that D_q is bounded from below by $(1 - q)^{-1}$, which can be observed in Fig. 5. Consider the 'time-reversed' linearized dynamics (compare Eq. (16))

$$\delta x_{n-1} \sim (1 + A)^{-1} \delta x_n \,, \tag{A15}$$

where A is the Gaussian random variable defined above. For this time reversed process, the distribution of finite time Lyapunov exponents, Eq. (A6), is identical to the 'time-forward' case but with an overall minus sign. Eq. (A12) thus implies that the fractal dimension for the reversed process flips sign compared to the time-forward process. As all fractal dimensions, including that of the time-reversed process, are bounded above by one, this observation together with Eq. (29), leads to $-D_q(q-1) \leq 1$. We thus find the lower bound

$$\frac{1}{1-q} \leq D_q \,, \tag{A16}$$

for the time forward process.

Appendix B: Non-analyticity of D_2

We start from Eq. (A10). A direct perturbation expansion of the correlation dimension yields that $D_2 =$

-1 for $\alpha = 0$, and that all other perturbation coefficients vanish. The same happens in the one-dimensional white-noise models for turbulent aerosols analyzed in Refs. [33, 43, 52]. The main issue with local perturbation theory in this case is that if $D_2(\alpha)$ near $\alpha = 0$ is a non-analytic function, then a perturbative expansion would naturally fail. One must use non-perturbative methods to analyze Eq. (A10). To extract this non-analytic dependence we write $D_2 = -1 + \beta(\alpha)$. We assume that the β-term is small, insert this ansatz into Eq. (A10), and expand the condition (A10) in β:

$$1 = I_0 - \beta I_1 + \beta^2 I_2 + \dots . \tag{B1}$$

The integrals I_k are given by

$$I_k = \frac{1}{k!}\int_{-\infty}^{\infty} \frac{\mathrm{d}A}{\sqrt{2\pi\alpha^2}}\, \mathrm{e}^{-A^2/(2\alpha^2)}\, |1+A| \log^k |1+A| \,. \tag{B2}$$

Let us first consider the linear order in β. Solving Eq. (B1) for β we find to this order

$$\beta_1 = \frac{I_0 - 1}{I_1} \,. \tag{B3}$$

To compute the expansion in α we require the asymptotics of I_0 and I_1. I_0 is given by the exact expression

$$I_0 = \mathrm{erf}\left(\frac{1}{\sqrt{2}\alpha}\right) + \frac{\mathrm{e}^{-1/(2\alpha^2)}}{\sqrt{2\pi}} 2\alpha, \tag{B4}$$

and its series expansion reads:

$$I_0 = 1 - \frac{\mathrm{e}^{-1/(2\alpha^2)}}{\sqrt{2\pi}} 2\alpha \sum_{k=1}^{\infty} (-1)^k (2k-1)!!\, \alpha^{2k} \,. \tag{B5}$$

The expansion of I_1 is more difficult. We obtain the asymptotic expansion of I_1 up to the special function ${}_1F_1{}^{(1,0,0)}(a,b,z)$ (the superscript $(1,0,0)$ denotes a derivative in the first argument a, see main text)

$$\begin{aligned} I_1(\alpha) \sim & -\frac{1}{2}\mathrm{erf}\left[\frac{1}{\sqrt{2\alpha^2}}\right]\left\{\gamma + \log\left(\frac{1}{2\alpha^2}\right)\right\} \\ & + \frac{\alpha}{\sqrt{2\pi}} \exp\left[-\frac{1}{2\alpha^2}\right]\left\{ -\gamma - \log\left(\frac{1}{2\alpha^2}\right) \right. \\ & \left. + {}_1F_1{}^{(1,0,0)}\left(1, \frac{1}{2}, \frac{1}{2\alpha^2}\right)\right\}, \end{aligned} \tag{B6}$$

where γ is the Euler–Mascheroni constant. We use the Mellin-Barnes integral representation of the Confluent Hypergeometric function ${}_1F_1$ to obtain the asymptotics of ${}_1F_1{}^{(1,0,0)}$ to exponential accuracy, see Appendix C. We obtain

$$\begin{aligned} I_1(\alpha) = & \sum_{k=0}^{\infty} \frac{(2k-1)!!}{2(k+1)} \alpha^{2k+2} + \frac{\mathrm{e}^{-1/(2\alpha^2)}}{\sqrt{2\pi}} \times \\ & [2(\gamma-1) - \log(\frac{\alpha^2}{2})] \left(\sum_{k=1}^{\infty} (-1)^k (2k-1)!! \alpha^{2k+1}\right), \end{aligned} \tag{B7}$$

for small positive values of α. Expanding the integral Eq. (B2) for $k = 2$, we obtain the expansion for I_2 given by

$$\begin{aligned} I_2(\alpha) = & \frac{\alpha^2}{4} \sum_{k=0}^{\infty} \frac{(2k+1)!!\,(1 - H_{2k})}{(k+1)\left(k+\frac{1}{2}\right)} \alpha^{2k} \\ & + \mathrm{e}^{-1/(2\alpha^2)}(\dots), \end{aligned} \tag{B8}$$

where $H_{2k} = \sum_{n=1}^{2k} 1/n$ and $H_0 = 0$. The exponentially small corrections in Eq. (B8) are disregarded because they contribute to D_2 only at higher order in $\mathrm{e}^{-1/(2\alpha^2)}$.

The expansions of I_0, I_1, and I_2 along with Eqs. (B1) and (B3) gives D_2 to the next-to-leading-order non-analytic term, Eq. (14). In this expansion of D_2, each non-analytic term is multiplied by an alternating, divergent series in α. We use Padé-Borel resummation with Padé approximants of order $(32, 32)$ to extract meaningful information from these series [8].

Appendix C: Mellin-Barnes transforms

The asymptotic expansion of the function ${}_1F_1^{(1,0,0)}(1, 1/2, 1/2a^2)$ for $a \to 0$ can be calculated using its Mellin-Barnes representation. The Mellin-Barnes representation is well known in the fields of Finite Temperature Quantum Field Theory where it is used to find asymptotics of infinite sums, and Conformally invariant Quantum Field Theories where it is the natural substitute for the Fourier representation due to its scale invariance properties. The discussion in this introductory section closely follows [54].

The Mellin transform $F(s)$ of a function $f(x)$ is defined as

$$F(s) \equiv \mathcal{M}[f; s] = \int_0^{\infty} \mathrm{d}x\; x^{s-1} f(x), \tag{C1}$$

and the transform can be inverted to give

$$f(x) = \int_{\mathcal{C}} \mathrm{d}s\; x^{-s} F(s), \tag{C2}$$

where $\mathcal{C}$ is a contour in the complex s plane. $\mathcal{C}$ is typically a line parallel to the $y-$axis, a curve asymptoting as $|s| \to \infty$ in the second and third quadrant and intersecting the $x-$axis at a finite value of $\mathrm{Re}(s)$, or a combination of the two. Assuming for $f(x)$, with $\delta > 0$,

$$f(x) = \begin{cases} O(x^{-a-\delta}), & x \to 0+ \\ O(x^{-b+\delta}), & x \to +\infty \end{cases}, \tag{C3}$$

the integral (C1) is absolutely convergent and $F(s)$ is an analytic function in the strip $a < \mathrm{Re}(s) < b$, referred to as the *strip of analyticity* of $F(s)$. Typically, the function $F(s)$ can be analytically continued outside this strip. It

can been proved that if $f(x)$ has the asymptotic behavior (compare with eq. (30))

$$f(x) = \begin{cases} \mathrm{e}^{-b_1 x^{-\mu_1}} \sum_m \sum_{l=0}^{N_1(m)} c_{lm} (\log x)^l x^{a_m}, x \to 0+ \\ \mathrm{e}^{-b_2 x^{\mu_2}} \sum_m \sum_{l=0}^{N_2(m)} c'_{lm} (\log x)^l x^{-b_m}, x \to \infty. \end{cases} \tag{C4}$$

$F(s)$ may be continued to, at worst, a meromorphic function outside it's *strip of analyticity*, and the singular terms in the Laurent expansion of $F(s)$ near the poles, if any, can be determined solely in terms of the constants appearing in (C4), the asymptotic expansion of $f(x)$[55].

1. Calculation of Asymptotics of ${}_1F_1^{(1,0,0)}(1, 1/2, 1/2a^2)$

For $\mathrm{Arg}(-z) < \frac{\pi}{2}$ the Confluent Hypergeometric function has the Mellin representation

$${}_1F_1(a,b,z) = \frac{\Gamma(b)}{\Gamma(a)} \frac{1}{2\pi i} \int_{c-i\infty}^{c+i\infty} \frac{\Gamma(-s)\Gamma(s+a)}{\Gamma(s+b)} (-z)^s \, \mathrm{d}s, \tag{C5}$$

where the contour of integration is a line parallel to the $y-$axis, possibly with kinks to separate the poles of $\Gamma(-s)$ from those of $\Gamma(s+a)$. One can obtain an asymptotic expansion of the ${}_1F_1$ by shifting his contour to the left over the poles of $\Gamma(s+a)$ [54]. Here we'll use the same procedure to obtain the asymptotic expansion of ${}_1F_1^{(1,0,0)}$. We use the Kummer transformation,

$${}_1F_1(a,b,z) = e^z \, {}_1F_1(b-a,b,-z), \tag{C6}$$

followed by differentiation in the first argument of ${}_1F_1$ to obtain

$$\begin{aligned} & e^{-z} {}_1F_1{}^{(1,0,0)}(1, 1/2, z) = \frac{d}{da} {}_1F_1(b-a,b,-z)\Big|_{a=1,b=1/2} \\ & = \psi(-1/2) {}_1F_1(-1/2, 1/2, -z) \\ & + \frac{1}{2} \frac{1}{2\pi i} \int_{c-i\infty}^{c+i\infty} \frac{\Gamma(-s)\Gamma(s-1/2)}{\Gamma(s+1/2)} \psi(s-1/2) \, z^s \, \mathrm{d}s \end{aligned} \tag{C7}$$

$$\begin{aligned} & = \psi(-1/2) {}_1F_1(-1/2, 1/2, -z) \\ & + \frac{1}{2} \frac{1}{2\pi i} \int_{c-i\infty}^{c+i\infty} \frac{\Gamma(-s)}{s-1/2} \psi(s-1/2) \, z^s \, \mathrm{d}s. \end{aligned} \tag{C8}$$

Since $\Gamma(s-1/2)$ has poles at at $s = 1/2, -i-1/2; i \in \mathbb{N}^0$ we obtain an asymptotic expansion by shifting the contour to the left over these poles, which gives

$$\begin{aligned} & \frac{1}{2\pi i} \int_{c-i\infty}^{c+i\infty} \frac{\Gamma(-s)}{s-1/2} \psi(s-1/2) \, z^s \, \mathrm{d}s \\ & = 2\sqrt{\pi}(\gamma - \psi(-1/2))\sqrt{z} + 2\sqrt{\pi}\sqrt{z}\log z \\ & + \frac{1}{2\pi i} \int_{c-1-i\infty}^{c-1+i\infty} \frac{\Gamma(-s)}{s-1/2} \psi(s-1/2) \, z^s \, \mathrm{d}s \\ & = 2\sqrt{\pi}(\gamma - \psi(-1/2))\sqrt{z} + 2\sqrt{\pi}\sqrt{z}\log z \\ & + \sum_{n=0}^{\infty} \frac{\Gamma(n+1/2)}{n+1} \frac{1}{\sqrt{z} z^n}. \end{aligned} \tag{C9}$$

This gives the full asymptotic expression for I_1,

$$\begin{aligned} & I_1(\alpha) \sim \frac{\alpha^2}{2} \sum_0^{\infty} \frac{(2k-1)!!}{k+1} \alpha^{2k} \\ & + \alpha \frac{e^{-1/2\alpha^2}}{\sqrt{2\pi}} (2(\gamma-1) - \log\frac{\alpha^2}{2}) \sum_1^{\infty} (-1)^k (2k-1)!! \alpha^{2k} \end{aligned} \tag{C10}$$

[1] B. J. Devenish, P. Bartello, J. Brenguier, L. R. Collins, W. W. Grabowski, R. H. A. IJzermans, S. P. Malinowski, M. W. Reeks, J. C. Vassilicos, L. Wang, and Z. Warhaft, Quarterly Journal of the Royal Meteorological Society **138**, 1401 (2012).

[2] A. Johansen, J. Blum, H. Tanaka, C. Ormel, M. Bizzarro, H. Rickman, and R. Dotson, "The multifaceted planetesimal formation process," in *Protostars and Planets VI* (University of Arizona Press, 2014) pp. 547–570.

[3] M. Wilkinson, B. Mehlig, and V. Uski, Astrophys. J. Suppl. **176**, 484 (2008).

[4] R. Reigada, R. M. Hillary, M. A. Bees, J. M. Sancho, and F. Sagus, Proc. R. Soc. Lond. B **270**, 875 (2003).

[5] J. S. Guasto, R. Rusconi, and R. Stocker, Ann. Rev. Fluid Mech. **44**, 373 (2012).

[6] K. Gustavsson, F. Berglund, P. R. Jonsson, and B. Mehlig, Phys. Rev. Lett. **116**, 108104 (2016).

[7] M. Cencini, G. Boffetta, F. De Lillo, R. Stocker, M. Barry, W. M. Durham, and E. Climent, Nature Communications **4**, 2148 (2013).
[8] K. Gustavsson and B. Mehlig, Adv. Phys. **65**, 1 (2016).
[9] Z. Warhaft, Fluid Dyn. Res. **41** (2009), 011201.
[10] E.-W. Saw, R. A. Shaw, J. P. L. C. Salazar, and L. R. Collins, New J. Phys. **14** (2012), 105031.
[11] J. Bec, L. Biferale, M. Cencini, A. S. Lanotte, and F. Toschi, Journal of Physics: Conference Series **333**, 012003 (2011).
[12] G. Falkovich, A. Fouxon, and G. Stepanov, Nature **419**, 151 (2002).
[13] S. Sundaram and L. R. Collins, J. Fluid. Mech. **335**, 75 (1997).
[14] M. Wilkinson, B. Mehlig, and V. Bezuglyy, Phys. Rev. Lett. **97** (2006), 048501.
[15] K. Gustavsson and B. Mehlig, Phys. Rev. E **84** (2011), 045304.
[16] K. Gustavsson and B. Mehlig, J. Turbulence **15**, 34 (2014).
[17] M. V. kuhle, A. Pumir, E. Lévêque, and M. Wilkinson, Arxiv (2013).
[18] M. Wilkinson and B. Mehlig, Phys. Rev. E **68**, 040101 (2003).
[19] M. Wilkinson and B. Mehlig, Europhys. Lett. **71**, 186 (2005).
[20] A. Crisanti, M. Falcioni, A. Provenzale, P. Tanga, and A. Vulpiani, Phys. Fluids **4**, 1805 (1992).
[21] M. Oberlack and F. H. Busse, *Theories of Turbulence* (Springer-Verlag Wien, 2002) pp. VII+373.
[22] G. Falkovich, K. Gawedzki, and M. Vergassola, Rev. Mod. Phys. **73**, 913 (2001).
[23] K. Gustavsson and B. Mehlig, Europhys. Lett. **96** (2011), 60012.
[24] E. Balkovsky, G. Falkovich, and A. Fouxon, Phys. Rev. Lett. **86**, 2790 (2001), cond-mat/9912027.
[25] J. Chun, D. L. Koch, S. L. Rani, A. Ahluwalia, and L. R. Collins, J. Fluid Mech. **536**, 219 (2005).
[26] K. Duncan, B. Mehlig, S. Östlund, and M. Wilkinson, Phys. Rev. Lett. **95** (2005), 240602.
[27] K. Gustavsson and B. Mehlig, Phys. Rev. E **87** (2013), 023016.
[28] B. B. Mandelbrot, Journal of Fluid Mechanics **62**, 331 (1974).
[29] T. C. Halsey, M. H. Jensen, L. P. Kadanoff, I. Procaccia, and B. I. Shraiman, Phys. Rev. A **33**, 1141 (1986).
[30] J. Bec, K. Gawedzki, and P. Horvai, Phys. Rev. Lett. **92** (2004), 224501.
[31] M. Wilkinson, B. Mehlig, and K. Gustavsson, Europhys. Lett. **89** (2010), 50002.
[32] K. Gustavsson, B. Mehlig, and M. Wilkinson, Physics of Fluids **27**, 073305 (2015).
[33] J. Meibohm, L. Pistone, K. Gustavsson, and B. Mehlig, Phys. Rev. E **96**, 061102 (2017).
[34] J. Deutsch, Phys. Rev. Lett. **52**, 1230 (1984).
[35] J. Deutsch, J. Phys. A **18**, 1449 (1985).
[36] M. Wilkinson, B. Mehlig, K. Gustavsson, and E. Werner, Eur. Phys. J. B **85**, 18 (2012).
[37] P. Grassberger and I. Procaccia, Phys. Lett. **97A**, 227 (1983).
[38] P. Grassberger and I. Procaccia, Physica D **9**, 189 (1983).
[39] D. Harte, *Multifractals* (Chapman & Hall/CRC, Boca Raton, FL, 2001) pp. xiv+248, theory and applications.
[40] E. Ott, *Chaos in dynamical systems, 2nd edition* (Cambridge Univeristy Press, Cambridge, UK, 2002) 478p.
[41] P. Grassberger and I. Procaccia, Physica D **9**, 189 (1983).
[42] A. S. Pikovsky, Phys. Lett. A **165**, 33 (1992).
[43] M. Wilkinson, R. Guichardaz, M. Pradas, and A. Pumir, Europhys. Lett. **111**, 50005 (2015).
[44] J. Bec, A. Celani, M. Cencini, and S. Musacchio, Phys. Fluids **17** (2005), 073301.
[45] J. Zinn-Justin and U. D. Jentschura, Annals of Physics **313**, 197 (2004).
[46] J. Zinn-Justin and U. D. Jentschura, Annals of Physics **313**, 269 (2004).
[47] G. Dorigoni, Department of Applied Mathematics and Theoretical Physics, arXiv:1411.3585 (2014).
[48] G. V. Dunne and M. Unsal, Phys. Rev. D **89**, 105009 (2014).
[49] H. Siebert, R. A. Shaw, J. Ditas, T. Schmeissner, S. P. Malinowski, E. Bodenschatz, and H. Xu, Atmospheric Measurement Techniques **8**, 3219 (2015).
[50] C. M. Bender and T. T. Wu, Physical Review **184**, 1231 (1969).
[51] C. M. Bender and T. T. Wu, Physical Review D **7**, 1620 (1973).
[52] K. Gustavsson, B. Mehlig, and M. Wilkinson, Phys. Fluids **27** (2015), 073305.
[53] H. Touchette, Phys. Rep. **478**, 1 (2009).
[54] R. B. Paris and D. Kaminski, *Asymptotics and Mellin-Barnes integrals*, Encyclopedia of Mathematics and its Applications, Vol. 85 (Cambridge University Press, Cambridge, 2001).
[55] N. Bleistein and R. A. Handelsman, *Asymptotic expansions of integrals*, 2nd ed. (Dover Publications, Inc., New York, 1986) pp. xvi+425.